

Wetting of geometrical structures in the order of the capillary length

Vom Fachbereich Maschinenbau
an der Technischen Universität Darmstadt
zur
Erlangung des Grades eines Doktor-Ingenieurs (Dr.-Ing.)
genehmigte

D i s s e r t a t i o n

vorgelegt von

Felix Gerlach, M.Sc.

aus Bad Nauheim, Deutschland

Berichterstatter: Prof. Dr.-Ing. Cameron Tropea

Mitberichterstatter: Prof. Dr. rer. nat. Steffen Hardt

Tag der Einreichung: 12.10.2020

Tag der mündlichen Prüfung: 09.12.2020

Darmstadt 2020
D17 (Diss. Darmstadt)

Felix Gerlach:

Wetting of geometrical structures in the order of the capillary length

Darmstadt, Technische Universität Darmstadt

Jahr der Veröffentlichung der Dissertation auf TUprints: 2021

URN: urn:nbn:de:tuda-tuprints-174175

URL: <https://tuprints.ulb.tu-darmstadt.de/id/eprint/17417>

Tag der mündlichen Prüfung: 09.12.2020



Veröffentlicht unter CC BY-NC-ND 4.0 International:

Namensnennung - Keine kommerzielle Nutzung - Keine Bearbeitung

<https://creativecommons.org/licenses/by-nc-nd/4.0>

Abstract

Wetting phenomena are often analyzed on the basis of single droplets or microscopic liquid flow phenomena. At industry scale such processes are rare and more often larger objects like wide rolls of material or whole car bodies are coated/wetted. At these scales macroscopic flow phenomena have a major impact on the wetting process. However, to simulate such processes it is necessary to reduce the complexity of the object surface in order to reduce the necessary computational resources. Therefore, the effects of geometrical features in the order of the capillary length on wetting have to be known in order to apply models instead of resolving them numerically.

In this thesis the capillary rise in macroscopic right-angled corners is analyzed experimentally in order to capture the main physically relevant effects for large scale wetting. At the beginning of the thesis the experimental equipment and post-processing techniques utilized for the experiments are introduced. This experimental setup allows dipping experiments with objects of a size up to two orders of magnitude above the capillary length to be performed at speeds of 0.01 mm/s to 500 mm/s. These experiments are measured with an optical resolution of approximately 20 μm . After the introduction of the test rig, the new insights into capillary corner rise (also called rivulet rise) are presented.

The interaction between concave and convex corners is analyzed by varying the inter-corner distance. This reveals the different length scales at which the concave corner alters the wetting at the convex corner and vice versa. Two models for the static shape of a rivulet are derived. One model combines different existing models from literature and the second model can be applied more generally and with fewer simplifications.

The dynamics of rivulet rise are analyzed for three different situations. The change in rivulet rise emerging from concave and convex corners in close proximity to each other is analyzed and described empirically. Since industrial surfaces are produced with macroscopic fabrication methods, the corners are not mathematically sharp, but are microscopically round and the effect of this roundness on the rivulet rise is investigated and theoretically modeled. Since many industrial processes involve moving parts and forced wetting, the influence of forced immersion of a corner on the rivulet rise is also analyzed and described with two complementary models.

The thesis concludes with first observations about the influence of roughness on wetting of flat walls. For this topic no models have been developed but different fabrication and measurement techniques have been tested and their characteristics are reported.

Kurzfassung

Benetzungsphänomene werden häufig auf Basis einzelner Tropfen oder mikroskopischer Strömungsphänomene untersucht. Im industriellen Maßstab sind Prozesse dieser Größenordnung selten und häufiger werden große Objekte wie beispielsweise breite Materialrollen oder ganze Karosserien benetzt/beschichtet. Auf dieser Längenskala haben makroskopische Strömungsphänomene einen entscheidenden Einfluss auf die Benetzung. Um solche Prozesse simulieren zu können ist es, zur Einsparung numerischer Ressourcen, notwendig die Komplexität der Objektoberfläche zu reduzieren. Daher müssen die Benetzungseffekte geometrischer Strukturen in Größenordnung der Kapillarlänge verstanden werden, um sie durch Modelle darzustellen und nicht numerisch auflösen zu müssen.

In dieser Studie wird der kapillare Anstieg in makroskopischen, rechtwinkligen Kanten untersucht, um die wichtigsten physikalisch relevanten Effekte für die Benetzung auf großen Längenskalen zu erfassen. Zu Beginn der Thesis werden das experimentelle Equipment und die Datenauswertungsmethoden vorgestellt. Der experimentelle Aufbau ermöglicht Eintauchexperimente mit Proben welche zwei Größenordnungen größer als die Kapillarlänge sind, Geschwindigkeiten von 0,01 mm/s bis 500 mm/s und einer optischen Auflösung von etwa 20 μm . Nach der Erläuterung des Prüfstands werden neu gewonnene Erkenntnisse zum kapillaren Anstieg in Kanten (auch Rivulet genannt) vorgestellt.

Durch Variation des Abstands zwischen konkaven und konvexen Kanten wird deren Interaktion untersucht. Dies zeigt die unterschiedlichen Längenskalen auf welchen eine konkave Kante die Benetzung an einer

konvexen Kante und umgekehrt beeinflusst. Es werden zwei Modelle für die statische Form von Rivulets hergeleitet, wobei das erste Modell unterschiedliche Literaturmodelle verknüpft, während das zweite Modell allgemeingültiger ist und weniger Vereinfachungen verwendet.

Die Dynamik von Rivuletanstiegen wird anhand dreier Situationen untersucht. Die Veränderung des Rivuletanstiegs durch die Nähe von konkaven und konvexen Kanten wird empirisch modelliert. Da industrielle Oberflächen mit makroskopischen Fertigungsmethoden hergestellt werden, sind sie nicht mathematisch scharfkantig sondern weisen mikroskopische Rundungen an den Kanten auf. Der Effekt dieser Rundungen auf den Rivuletanstieg wird analysiert und modelliert. Industrielle Prozesse beinhalten bewegende Teile und erzwungene Benetzungen, daher wird auch der Einfluss von eintauchenden Kanten auf den Rivuletanstieg untersucht und mit zwei sich ergänzenden Modellen abgebildet.

Die Thesis schließt mit ersten Beobachtungen über den Einfluss von Rauheit auf die Benetzung flacher Wände. Für dieses Thema wurden keine Modelle erstellt, sondern verschiedene Fertigungs- und Messmethoden getestet. Deren unterschiedlichen Eigenschaften werden vorgestellt.

Acknowledgements

In the first place I want to thank Professor Dr.-Ing. **Cameron Tropea** for giving me the opportunity to work at the Institute of Fluid Mechanics and Aerodynamics at the Technical University of Darmstadt as part of the Collaborative Research Center SFB 1194. He gave me plenty of freedom during my research, allowing me to test different approaches and investigate new methods. I could discuss complex problems with him and he made it possible for me to present my research results at international conferences.

I also want to thank Professor Dr.-Ing. **Jeanette Hussong** who gave me the opportunity to continue my work after the retirement of Prof. Tropea. She supported my project and my thesis and always had a sympathetic ear for questions and discussions.

Professor Dr. **Ilia V. Roisman** provided invaluable scientific support in deriving models for new phenomena and in our discussions about complex modeling issues he provided important input and new perspectives. I want to thank him for this scientific support.

A special thanks to Professor **Stephen Garoff** from Carnegie Mellon University who supported me during my entire doctoral period with fruitful discussions, visiting our university and giving me the opportunity to visit his department. I hope that our on-going collaboration culminates in a great published article.

I also would like to thank Professor Dr. rer. nat. **Steffen Hardt** from the Institute for Nano- and Microfluidics for refereeing my thesis.

I want to thank **Frank Plückebaum** for constructing and building many parts of experimental equipment and carrying out an endless number of different measurements. He was always available to discuss the current issues of the experimental rig and possible improvements.

Birgit Neuthe, **Corinna Neumann**, **Monika Medina-Espana**, **Stephanie Lath** and **Petra Fuhrmann** helped me with many

administrative tasks. I want to thank them all for this help.

My experimental rig would not have been possible without the help and work from **Ilona Kaufhold**, **Tim Geelhaar** and **Joachim Heyl** in the mechanical workshop and the help for electrical devices from **Martin Weiß**. For this technical support I want to thank them all.

Especially I want to thank my former and current office mates **Sebastian Wegt**, Dr.-Ing **Benjamin Krumbein**, **Maximilian Bopp** and **Ivan Joksimovic** who enriched my work and spent many hours discussing various issues with me.

Further colleagues I want to mention and thank, because I had many helpful and interesting discussions with them, are **Sebastian Brulin**, Dr.-Ing **Markus Schremb**, **Louis Reitter**, **Mark Gloerfeld**, **Sebastian Blahout** and **Bastian Stumpf**. Furthermore, Sebastian Wegt as well as Sebastian Brulin proofread major parts of this thesis, for which I am grateful.

I want to thank **Maximilian Hartmann** from the Institute for Nano- and Microfluidics for his Surface Evolver simulations, which enriched our two joint papers. I could always discuss various problems with him.

I had many fruitful discussions with **Benedikt Straub** working at the Max Planck Institute for Polymer Research on the same collaborative research project as me. He also helped me by proofreading parts of this thesis and I want to thank him very much for both.

Julian Schäfer from the Institute of Printing Science and Technology spent many hours of fruitful discussions about gravure printing and co-supervising our Advanced Design Project, for which I want to heartily thank him.

I also want to thank **Jiangsheng Wang** from Beihang University who visited our institute for one very interesting year full of fruitful discussions.

Furthermore, I want to thank **Till Feldner** and **Fabian Weidler** for their support during their Bachelor theses, in which they spent many hours performing measurements.

Also I want to thank **Christian Braun**, **Janita Braun**, **Marcus Freiherr Ebner von Eschenbach**, **Leo Gögelein** and **Fabius Jäger**, who designed the gravure printing module for the experimental test rig and programmed all necessary functions for it

during their Advanced Design Project.

Bertin Junior Waffo Kegni and **Daniel Elmeua Lehmann** worked as student assistants for me, post-processing data, setting up new sensors and performing test measurements. I want to thank both for their help.

Finally, I want to thank my parents and friends who supported me during the last years and accepted not seeing me as often as in the past. A special thanks to my girlfriend **Ankatrin Weber**, with whom I paced through both our theses together, withstanding all occurring difficulties.

Contents

Abstract	I
Kurzfassung	III
Acknowledgements	V
1 Introduction	1
1.1 Wetting – Relevance in industry and everyday life	1
1.2 The enigma of wetting physics	3
1.3 Thesis outline	5
2 Fundamentals of wetting	7
2.1 Basic equations	7
2.2 Dimensionless parameters	9
2.3 Model challenges	11
2.3.1 Contact line singularity	12
2.3.2 Contact angle hysteresis	15
3 Experimental details	21
3.1 Experimental setup	21
3.1.1 Liquids and samples	30
3.1.2 Data acquisition	40
3.2 Data post-processing	44
3.2.1 Ray calibration	44
3.2.2 Image enhancement	56
3.2.3 Rough surface post-processing	57

4 Rivulets and cusps	59
4.1 Basics of rivulets and cusps	59
4.2 Static shape of rivulets and cusps	64
4.2.1 Interaction of rivulets and cusps	64
4.2.2 Shape of rivulets	69
4.3 Rivulet dynamics	83
4.3.1 Influence of cusps	83
4.3.2 Roundness effects	86
4.3.3 Forced rivulet dynamics	101
5 Wetting of rough surfaces	109
5.1 Basics of roughness wetting	109
5.2 Roughness fabrication	110
5.3 Effects of roughness on wetting	113
6 Summary and outlook	117
A Appendix	121
A.1 Force measurement details	121
A.2 Light field calibration details	121
A.3 Shadow technique details	122
A.4 Bubble counting details	125
A.5 Laser refraction details	128
A.6 Liquid data	132
A.7 Surface roughness values	133
Bibliography	135
Nomenclature	153
List of Figures	163
List of Tables	169

1 Introduction

1.1 Wetting – Relevance in industry and everyday life

Wetting is important in many practical applications. Nevertheless it is a topic seldom considered in everyday life or engineering context. In this section different wetting examples from everyday life and industry are shown. Probably the first wetting problem encountered in the morning during everyday life is the water on the walls of a shower. After showering, the walls are speckled with pinned water drops, which do not flow down without forcing by a shower screen wiper. Leaving the house during fog leads to water drops condensing on eyeglasses. When coming into a building while it is cold outside, humidity also condenses onto cold eyeglasses. During rain, water drops impact onto the windshield of vehicles and flow away in rivulets, driven by gravity, wetting and aerodynamic forces. The prediction of the paths of these rivulets is a difficult but important task, since this rivulets can obscure the view of the driver and are thus a safety factor.

Another wetting aspect is the removal of oils and grease from surfaces. Since they wet most surfaces very well, even mechanical cleaning methods like scrubbing often leave a residual oil film on surfaces. A similar problem is known in the oil industry in the context of oil recovery. Oil recovery tries to gain oil from oil soaked porous ground and thus has to remove the oil from the porous surface.

Printing techniques transfer liquid into defined patterns on various surfaces. Therefore wetting and spreading phenomena are a crucial part

1 Introduction

of this techniques. Especially when it comes to functional printing, which means the printing of electric circuits, it is crucial to control where conductive paint is applied and where not.

A huge field of wetting applications are coating techniques. There exist various coating techniques (slot, slide, curtain, knife and roll, meniscus roll, dip and spin coating)[1] which serve the coating of all kind of objects (from artificial hands for the production of one-way gloves to entire car bodies for priming) with different coatings like paint, rubber, plastic, etc. Kistler and Schweizer [1] name numerous further examples, such as different grades of paper with different surface finishes, packaging materials, printed paper products, magnetic hard drives, optical storage media (CD, DVD, Blu-ray), wires and fibers, labels, photoresistant coatings for the production of printed circuits and solar cells, ceramic components made from sol/gels, sensors, transdermic applicators for medical drugs, textiles, sand paper and adhesive tapes. The optimal process for all coating methods and products mentioned above is given by a defect-free coating layer of well defined thickness applied with the highest possible coating speed.

Dip coating is one of the oldest and most versatile coating techniques. As described by its name, it simply consists of dipping an object into a pool of coating liquid, letting wetting physics determine the amount of liquid coated to the surface of the object. The basic process parameters are the orientation of the object and the acceleration and velocity of submerging and withdrawal. Additionally rotating movements, liquid and gas convective currents, doctor blades in the liquid pool, surfactants and different ambient pressures and temperatures and liquid temperatures can be applied to modify the coating behavior.

Since wetting physics can act very freely in dip coating processes and nearly arbitrary objects and liquids can be used and observed with different measurement techniques, this thesis uses dip coating to analyze basic wetting and dewetting phenomena, which were not well understood beforehand, e.g. capillary driven rivulet rises. These phenomena are not

limited to dip coating, instead they are of generic nature and occur in various wetting and dewetting scenarios, which allows extrapolation of the gained insights to other wetting scenarios.

1.2 The enigma of wetting physics

Although many fundamentals of wetting have been investigated in the last century, there still remain many aspects of wetting and dewetting not fully understood and many related industrial processes are, therefore, often based on empiricism or operator experience [1]. This is due to liquids sometimes exhibiting different wetting behavior, although only minute or no deliberate parameter changes at all have been incurred.

One example of such unpredictability is the influence of surface roughness on dynamic wetting. Roughness can be parameterized in many ways, such as the standards defined in 1D (DIN EN ISO 4287) or 2D (EN ISO 25178). To correlate roughness with wetting behavior, various alternative measures have been used in the past, for instance R_z [2, 3], R_a [2, 4–6] (both from DIN EN ISO 4287), or a selection of more sophisticated parameters [7] such as the Wenzel factor r [5, 6, 8] (see Eq. (5.1)). However, none of these parameters have proven to universally describe the effects of roughness for different wetting scenarios. This leaves roughness being a huge source of uncertainty when designing wetting processes.

A similar uncertainty can be observed for the characterisation of contact angles (see Fig. 2.1), reflecting the fundamental ability of a system to wet or dewet. For example, Chibowski [9] collected five literature values for the advancing contact angle of water on polypropylene, ranging from 91.5 to 108.7°. Small variations in the surface properties, cleaning or environmental conditions lead to different contact angles; moreover, high fluctuations are often noted when repeating measurements. Under controlled conditions the value of a contact angle can be taken from literature values, but without checking the real contact angle in any given

1 Introduction

situation, unconsidered side effects can lead to different values than given by the literature.

This unpredictability of wetting effects complicates the construction of machinery and devices based on wetting. The resulting uncertainties in experiments originating from these enigmas can obscure other physical effects occurring in combination with wetting phenomena, e.g. during capillary force driven wetting [10–13]. A previous PhD thesis of Manukyan [14] dealt with capillary effects and showed a very rich wetting behavior on surfaces structured with pyramidal arrays. However, the wetting patterns on these surfaces were too complex to be described comprehensively. Reasons complicating the wetting behavior were the complex structure and the uncertainties mentioned above. Hence, for further experimental research as many of this uncertainties as possible have to be avoided to receive reproducible results which do not possibly emerge from a specific wetting defect instead of being a general wetting effect. What is more, experiments gain clarity by reducing the complexity of the surface structures to the minimal possible amount of complexity. This allows reducing side effects and analyzing the effect of single structures onto the wetting. When these effects are understood and physically described, interactions among different structures can be observed for further understanding of more complex surface topologies.

In this thesis a simplified, generic surface structure (see Fig. 3.5) is used to reduce the geometrical complexity of typical applications. This simpler geometry is used in combination with silicone oils (see subsection 3.1.1) to further reduce contact angle variations as well as the influence of roughness on the wetting. With this simplified setup, basic phenomena are investigated which are otherwise obscured due to complex surface patterns, contact angle and roughness uncertainties. These basic phenomena then form the basis for further investigation of the coupling among different phenomena and to allow the future prediction of wetting patterns on complex surface geometries.

1.3 Thesis outline

This first chapter of the thesis introduces the topic of wetting on structured surfaces and outlines the scope of the study. After giving examples of wetting phenomena in everyday life and industry in section 1.1, section 1.2 highlights the unpredictability of wetting for design processes.

Chapter 2 introduces the terminology of wetting. The basic equations used to describe wetting phenomena are given in section 2.1. In section 2.2 the most important dimensionless numbers for the characterisation of wetting phenomena are given. Section 2.3 discusses two of the main challenges in modelling wetting phenomena, for which no general solution is known today. Subsection 2.3.1 outlines different strategies to deal with the microscopic region close to the contact line, while subsection 2.3.2 describes the differences in contact angle definition and different equations for calculating dynamic contact angles.

In Chapter 3 the experimental and post-processing techniques are introduced. The experimental rig built and used in this thesis is described in section 3.1. In subsection 3.1.1 the utilized liquids and samples are presented and in subsection 3.1.2 the measurement methods used in this thesis are introduced. Section 3.2 describes the process of data post-processing necessary to obtain quantitative values from the chosen measurement system.

The major part of experimental research was performed on the subject of rivulets and cusps formed on geometrically complex surfaces. These phenomena appear at edges and all geometries can be interpreted as a combination of different edges (like when building a 3D mesh of an arbitrary shape). This, in theory, allows to predict the wetting behavior of arbitrary geometries when the wetting of simple edges and the interaction between them is fully understood. In literature and also in the publications written by the author, edges on samples are usually referred to as corners. To clearly distinguish between edges (along a line)

1 Introduction

and corners (one point) at which several edges meet, edges will not be called corners in this thesis. The insights gained for the wetting of edges are presented in Chapter 4. In the beginning, the basic equations for this topic are introduced in section 4.1 before the static rivulet shape is discussed in section 4.2. The rivulet shape in the vicinity or far away from a cusp is described in subsection 4.2.1 before subsection 4.2.2 introduces two models for the static shape of a rivulet. At first a model for right-angled edges using some approximations was formulated. Based on this model, a second model being more advanced and universally valid was derived. Section 4.3 deals with the dynamics of rivulet wetting, subdivided into subsection 4.3.1, analyzing the effect of nearby cusps onto the rivulet rise, subsection 4.3.2, explaining the effect of curvature in edges on rivulet rise, and subsection 4.3.3, describing the quasi-steady state forced rivulet rise, as it is seen in real-world coating applications.

Chapter 5 presents results obtained by analyzing the wetting and dewetting of rough surfaces. Structured similar as Chapter 4, section 5.1 introduces the basic equations used to describe the wetting and dewetting of rough surfaces. Section 5.2 describes how the samples for roughness measurements were manufactured and prepared. This chapter concludes with section 5.3 giving insights obtained for the wetting and dewetting of rough surfaces.

In the final Chapter 6, the findings of this thesis are summarized and open questions which require further study are highlighted.

2 Fundamentals of wetting

Figure 2.1 introduces the two important concepts in the field of wetting. It shows the definitions of the *contact line* and the *contact angle* θ using the example of a drop on a flat surface. The line at which the outer surface of the liquid meets the solid surface is marked in red and called the three-phase contact line or simply contact line. The angle at which the liquid surface meets the solid surface is marked in green and called the contact angle. By definition, the contact angle is the angle measured inside the liquid.

This chapter contents itself with introducing basic equations (2.1) and phenomena (2.3), from which advanced models can be derived. A more comprehensive overview of known wetting physics and models is given in the review article of Bonn et al. [15].

2.1 Basic equations

The first mathematical description of the situation shown in Fig. 2.1 was provided by Thomas Young in 1805, who postulated that an equilibrium of forces emerging from the surface tensions between liquid and gas (σ_{lg}), liquid and solid (σ_{ls}) and solid and gas (σ_{sg}) exists at the static contact line. This results in the Young equation [16]:

$$\sigma_{sg} = \sigma_{ls} + \cos(\theta) \sigma_{lg} \quad (2.1)$$

Based on this equation, materials with high contact angles (like plastics) are often referred to as "low surface energy" materials because a high

2 Fundamentals of wetting

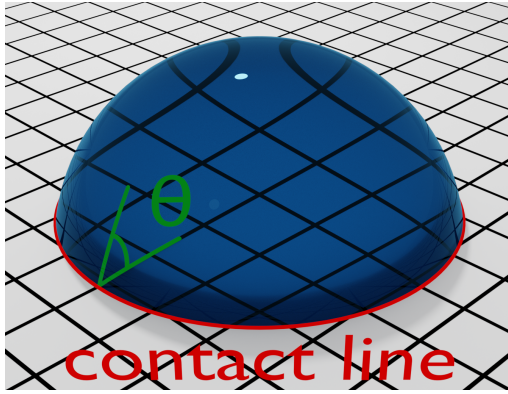


Figure 2.1: Contact line and contact angle θ shown for a drop on a flat surface.

value of θ corresponds to a low value of σ_{sg} . The surface tensions σ_{sg} and σ_{ls} cannot be measured directly and are therefore more of theoretical nature. In the following discourse, the surface tension between liquid and air σ_{lg} will be used, in favor of readability it will be described as σ without a subscript.

A second important relation, found independently by Thomas Young and Pierre-Simon Laplace in 1805, is the so-called Young-Laplace equation [17]. It describes the pressure difference between the inside and the outside of a liquid due to its surface curvature, given by the two main radii of curvature r_1 and r_2 .

$$\Delta p = \sigma \left(\frac{1}{r_1} + \frac{1}{r_2} \right) \quad (2.2)$$

The pressure difference expressed by Eq. (2.2) (also called the Laplace pressure) is the primary driving force of many wetting phenomena. While it is negligible on larger scales, where r_1 and r_2 become large, the Laplace pressure can reach very high values for wetting phenomena occurring on

the order of millimeters or smaller. For steady-state situations under the influence of gravity in which a liquid is not moving, the Laplace pressure usually has to equal the hydrostatic pressure inside the liquid, given by

$$p = \rho gh. \quad (2.3)$$

In Eq. (2.3) ρ expresses the density of the liquid, g the gravitational constant and h the height. The static surface shape of a liquid element can be calculated by combining Eqns. (2.2) and (2.3). When the liquid is moving, viscous friction arises, which is defined as

$$f = \mu \nabla^2 u \quad (2.4)$$

for a Newtonian liquid. A second counteracting force is the inertia of the liquid, delaying changes of velocity. For the systems studied in this thesis inertial effects are usually negligible.

2.2 Dimensionless parameters

Dimensionless parameters are values composed of different physical variables in a manner that all physical units cancel out. The most widespread example in fluid mechanics is the Reynolds number

$$Re = \frac{\rho ul}{\mu} \quad (2.5)$$

in which μ describes the dynamic viscosity of a fluid and u and l a characteristic speed and length respectively. The Reynolds number has no physical units, regardless of the system of measurement (e.g. SI or imperial units). Moreover, the value of a dimensionless number is independent of the measurement units. These properties give dimensionless parameters the ability to universally describe physical systems. When the relation between all relevant dimensionless parameters and physical measurements is sufficiently understood, the

2 Fundamentals of wetting

physical behavior of different systems sharing the same dimensionless parameters can be predicted.

The Reynolds number in Eq. (2.5) describes the ratio of inertial to viscosity forces. For small Reynolds numbers (< 1) inertial effects can be neglected, while for high Reynolds numbers ($\rightarrow \infty$) viscosity effects can be neglected.

A further important dimensionless parameter for wetting phenomena is the Capillary number

$$Ca = \frac{\mu u}{\sigma}. \quad (2.6)$$

The Capillary number describes the ratio of viscosity to surface tension forces. For Capillary numbers much smaller than unity, viscosity forces can be neglected, while for high Capillary numbers surface tension forces can be neglected.

An alternative to the usage of Ca for the description of wetting systems is the use of the Weber number

$$We = \frac{\rho u^2 l}{\sigma} = Re Ca \quad (2.7)$$

which can be calculated by multiplying the Reynolds and the Capillary number. The Weber number describes the ratio of inertia to surface tension forces. Since only two of Re , Ca and We have to be known to calculate the third parameter, using all three parameters gives no additional insight into a physical problem.

All three dimensionless parameters contain a characteristic speed u , Re and We additionally contain a characteristic length l . For common engineering problems like the flow in pipes or over airfoils, it is common to use the diameter or the chord length as a macroscopic characteristic length. However, for wetting phenomena often no characteristic length is

known. One simple example is an infinite wall, half submerged into an infinite liquid pool. When the wall is moving, a characteristic speed u can be defined, but the only non-infinite length in the system is the rise or suppression of the liquid meniscus, which itself is a function of various parameters like the contact angle θ ; thus, it is not suitable to use as characteristic length l . The same is valid for rivulets and cusps existing in semi-infinite geometries without a length scale, as discussed in more detail in section 4. Anticipating that rivulets can become quite high, the characteristic length in Re (Eq. (2.5)) scales the magnitude of the inertial forces, but since a rivulet also becomes very thin when it becomes high, it is clear that the rivulet height does not contribute much to its inertia and so it is not the appropriate length to use in the Reynolds number. When the diameter of a rivulet is taken as characteristic length instead, the question arises, which diameter to use since the width of a rivulet varies from zero to infinity from top to bottom. For this kind of problem the appropriate characteristic length is usually the capillary length

$$l_\sigma = \sqrt{\frac{\sigma}{\rho g}} \quad (2.8)$$

The capillary length is given by the ratio of surface tension to gravitational forces and is an unique fluid system property. The geometrical size of wetting systems can be compared to the capillary length to obtain some physical insight as to the importance of capillary forces (Laplace pressure). Systems smaller than the capillary length are dominated by surface tension forces, while gravitational forces are small or can even be neglected. Systems larger than the capillary length are dominated by gravitational forces and surface tension forces become less significant.

2.3 Model challenges

While the set of equations introduced in section 2.1 was already known in 1805, even today wetting phenomena are still challenging to predict, as discussed above in section 1.2. Experience has shown that a unique contact angle, as expressed in Eq. (2.1), does not exist. Instead different

2 Fundamentals of wetting

contact angles for liquid spreading over a surface (advancing) or liquid being drawn from a surface (receding) on different length scales can be measured, leading to a variety of contact angle models, as outlined in subsection 2.3.2.

Another challenge, especially for numerical applications, is the frictional force defined in Eq. (2.4). A singularity occurs at the contact line where the moving liquid surface contacts the wall, at which it is not allowed to move due to the no-slip condition, leading to an infinite velocity gradient directly at the contact line. The resulting infinite frictional force would, if it would be a real phenomenon, prevent any object to be ever wetted. Different model approaches exist to overcome this shortcoming in basic theoretical modeling. These models are outlined in subsection 2.3.1.

2.3.1 Contact line singularity

Fig. 2.2 shows the contact line region of a moving liquid in 2D. Due to the no-slip boundary condition the liquid directly at the wall cannot move, resulting in a boundary layer inside the liquid. The surface of the liquid has to move forward, otherwise the liquid bulk would not move. When approaching the contact line, the distance between the moving liquid surface and the fixed boundary layer decreases. This results in a strong velocity gradient which is proportional to a high frictional force (Eq. (2.4)). Directly at the contact line the distance between the moving outer surface and the fixed liquid at the wall becomes zero, leading to an infinite frictional force.

This problem was first encountered by Huh and Scriven in 1971 when they solved the flow shown in Fig. 2.2 using a stream function [18]. They pointed out that one possible solution of this problem is the replacement of the no-slip boundary condition with Navier slip. This in turn makes the friction dependent on the amount of slip given as a parameter and different authors found different amounts of slip matching to their analyzed systems. Because of this inconsistency Thomson and Troian

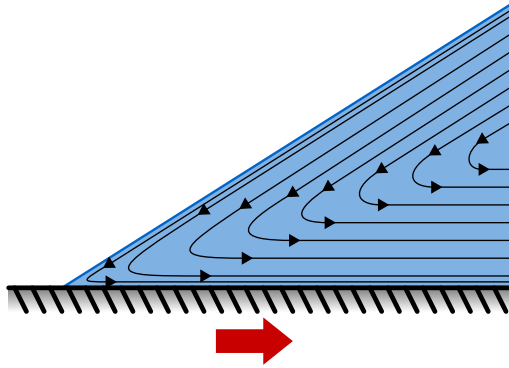


Figure 2.2: The linearized contact line region of liquid on a wall moving to the right.

defined a non-linear slip function, giving appropriate slip lengths for different systems [19].

Another solution to the contact line singularity is the assumption of a precursor film in front of the contact line which solves the problem by simply eliminating the contact line. This solution was proposed by Hervet and de Gennes in 1984 [20] and is partly supported by studies observing precursor films for certain setups [21]. In contrast to the mathematical infinite film without a contact line, real precursor films are limited and hence have the same contact line singularity which Hervet and de Gennes try to circumvent. Eres et al. [22] developed a model assuming this film to be only of a molecular size instead of being a macroscopic liquid film. For volatile liquids like ethanol or water it can be assumed that every time a small amount of vapor is in the air in front of the bulk liquid, it deposits on the solid surface and hence forms this kind of molecular precursor film. But for non-volatile liquids like silicone oil or wetting phenomena on fresh surfaces taking place much faster than vapor deposition, a liquid precursor in front of the contact line seems to be unlikely.

2 *Fundamentals of wetting*

A related model to both concepts was proposed by Hocking [23] who assumed every surface to have some roughness in the form of grooves, which either contain air when a liquid front is approaching or retain some liquid in the case of dewetting. In both cases the liquid only contacts the air or liquid in the grooves and thus there is either no contact line at all for the dewetting case, like with a precursor film, or the contact line connects liquid and air and hence does not have to obey a no-slip boundary condition at a wall. Both cases can be calculated by modelling the roughness on the flat surface with a slip length. While this model tries to physically explain the presence of slip, the explanation becomes invalid for very smooth surfaces like silicon wafers.

A different modelling approach was given by Weidner and Schwartz [24], who no longer assumed Newtonian liquids with a constant dynamic viscosity and instead assumed the liquid to be slightly shear thinning. Their approach limits the amount of shear thinning to a degree in which the bulk still behaves very close to a Newtonian liquid while the shear thinning becomes important close to the contact line where it results in integrable frictional forces allowing the calculation of the liquid movement without any slip, even though the shear stress directly at the contact line is still infinite. Boudaoud [25] also found a working model for non-Newtonian liquids. His model is based on polymeric suspensions which exhibit normal stresses. With these normal stresses he was able to calculate the spreading of a droplet forming a precursor film without a contact line singularity.

Wayner developed a model using evaporation and condensation to allow contact line movement without slip or rheological changes [26]. Seppacher went in a similar direction by modeling the liquid air interface as a diffuse interface with finite thickness, allowing mass transfer from one side to the other [27]. The next step from this diffusive interface model is the breakdown of the liquid into single molecules in order to leave continuum mechanics and model the area close to the contact line using molecular dynamics (MD). Since molecules can jump along the wall, a moving contact line can be simulated using MD without the need

of any additional assumptions for solving the contact line singularity [28]. The obvious drawback of MD simulations is the enormous amount of computational resources needed for a simulation resolving real-world problems down to the scale of single molecules.

At least on superhydrophobic surfaces the motion of the contact line was found experimentally to not cause a singularity. For advancing liquids a rolling motion like that of a wheel with an approximate contact angle of 180° can be observed, while receding occurs in a similar manner but with the liquid pinned to the pillars of the superhydrophobic surface before breaking free [29].

2.3.2 Contact angle hysteresis

Experience has shown that there is no single value which can be applied for a real-world contact angle, unlike proposed by Young in 1805 [9, 30–35]. Usually drops of liquid can be applied to a surface and, depending on how they were placed, they can exhibit different static contact angles. It was found by experiment that there exists a range of equally probable static contact angles which are limited by an upper value called the advancing contact angle (θ_a) and a lower value called the receding contact angle (θ_r). For contact angles greater than θ_a , the contact line begins to advance away from the liquid bulk in order to reach a static force balance, while for contact angles lower than θ_r , the contact line starts to recede back into the direction of the bulk. When the velocity of the contact line movement increases, the contact angle (in this case called dynamic contact angle θ_d) changes further, as sketched in Fig. 2.3. The angles θ_a and θ_r are usually measured by forcing a very slow motion of the contact line in order to receive a value as close to the desired value as possible. However, close to stagnancy the motion of the contact line is unsteady, exhibiting a "stick-slip behavior". In this regime the contact line stops/pins at the surface while the contact angle decreases or increases until the force imbalance becomes large enough to move the contact line, which results in the contact angle relaxing back again, leading to a pinning of the contact line at the next sufficiently large

2 Fundamentals of wetting

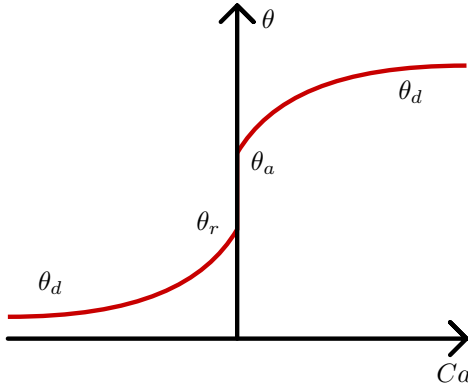


Figure 2.3: A qualitative sketch schematically showing the relationship between dimensionless contact line speed and contact angle.

surface defect. Due to this behavior, even for non-volatile liquids it is difficult to measure contact angles at very low velocities. One major factor influencing the width of the static contact angle interval and the amount of stick-slip behavior at slow movements is the roughness of the surface promoting local pinning defects. Fig. 2.4 shows a common explanation for pinning at sharp surface defects with constant advancing contact angles θ_a . A liquid approaching the sharp edge of angle γ with θ_a has to increase its contact angle by $\Delta\theta_a = \gamma$ to reach θ_a on the surface on the other side of the kink and continue advancing. Thus it stops at the edge until its (now static) contact angle is increased to θ_a on the right surface of the edge to enable continuation of the movement at the surface. For receding contact angles a similar effect happens with the contact line stopping at the kink until its contact angle decreased by $\Delta\theta_r = \gamma$ in order to continue receding on the other side of the kink.

Dussan assumed the contact angle to have an unique value on a microscopic level, called θ_m [36]. With this assumption, macroscopic measured contact angles are only results of the further deformed liquid surface and hence without physical meaning. While it is widely accepted

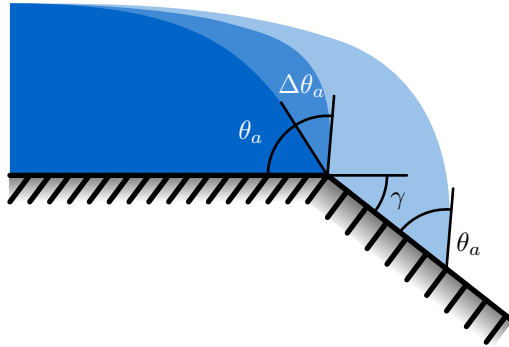


Figure 2.4: Pinning at a sharp kink until the advancing contact angle increased by $\Delta\theta_a = \gamma$. For receding contact lines the same pinning happens until the contact angle is decreased by $\Delta\theta_r = \gamma$.

as an unsolved problem that the measured contact angle depends on the distance to the contact line, due to the logarithmic [20, 21, 37–39] liquid surface curvature, a constant microscopic contact angle could not be found and its definition and reproducible measurement would be as difficult as for macroscopic contact angles, due to the diffuse nature of the liquid surface at a molecular level.

In order to reduce the measurement error on rough surfaces, vibrations can be used to overcome the energetic barrier of pinning, which enables the contact line to reach its state of lowest energy, partially removing the hysteresis of the measured contact angle [33, 40–44]. However, this process is not straight-forward since the vibrational energy has to be high enough to ensure the contact line reaching its state of lowest energy, while too strong vibrations lead to a breakup up of the liquid, resulting in an uneven contact line or even several small satellite droplets. These droplets have smaller volume-to-surface ratios; hence, they need even stronger vibrations to overcome the surface tension induced pinning by the use of inertial effects.

2 Fundamentals of wetting

In literature different physical and empirical models for the dynamic contact angle sketched in Fig. 2.3 are common and until now, authors are still using different models, since no model is universally applicable. The most commonly used model is the Hoffman-Voinov-Tanner model [45]

$$\theta_d = f(f(\theta) + Ca) \quad \text{general equation} \quad (2.9)$$

$$\theta_d = (\theta^3 + Ca)^{1/3} \quad \text{commonly used version} \quad (2.10)$$

in which θ refers to Young's static contact angle and f is a function. Hoffman did not explicitly define the two functions in this model and so different functions are used in literature, all referring to Hoffman. Voinov published a modified version of this model, called the Voinov model [46]

$$\theta_d = \left(\theta_m^3 + 9Ca \ln \left(\frac{h}{h_m} \right) \right)^{1/3} \quad \text{for } \theta_d < 135^\circ, \quad (2.11)$$

in which h depicts the macroscopic length on which θ_d is measured/calculated while h_m depicts the microscopic length belonging to θ_m . When θ_m and $\ln(h/h_m)$ are used as free parameters the Voinov model can be fitted to many dynamic contact angle measurements despite its simple nature.

Kistler formulated a more advanced function for use in the Hoffman-Voinov-Tanner model over a wider range of Ca , which is

$$\theta_d = \arccos \left\{ 1 - 2 \tanh \left[5.16 \left(\frac{Ca}{1 + 1.31 Ca^{0.99}} \right)^{0.706} \right] \right\} \quad (2.12)$$

proposed in [47]. The parameters in this function are fitted to experimental data for completely wetting ($\theta = 0$) high viscosity liquids. For $Ca < 0.1$ Eq. (2.12) can be simplified to

$$\theta_d = 4.54 Ca^{0.353} \quad (2.13)$$

which is very similar to the commonly used version of the Hoffman-Voinov-Tanner model from Eq. (2.10). Jiang [48] defined a different empirical correlation for the dynamic contact angle which is remarkable akin to Eq. (2.12):

$$\theta_d = \arccos \left\{ \cos(\theta) - (1 + \cos(\theta)) \tanh [4.96 Ca^{0.702}] \right\} \quad (2.14)$$

Bracke [49] published a model in a similar form, but missing the tanh function and exhibiting a different exponent:

$$\theta_d = \arccos \left\{ \cos(\theta) - (1 + \cos(\theta)) 2 Ca^{0.5} \right\} \quad (2.15)$$

With these most common dynamic contact angle models the dynamic contact angle for different wetting and dewetting speeds perpendicular to the contact line can be calculated. Often dynamic contact angle models only fit to experimental data with low Capillary numbers. But even when a model predicts the correct contact angle for every Capillary number, another limitation appears at $\theta_d \sim 0$ for dewetting and $\theta_d \sim 180^\circ$ for wetting cases. When the dynamic contact angle reaches these limits the speed is called the critical de-/wetting speed and if the speed is further increased, the contact line starts to take on a saw tooth shape [50] and finally breaks up, either by leaving liquid droplets on a surface while dewetting or entrapping air in the liquid while wetting. The precise physical interactions leading to this failure in de-/wetting are not well understood and proper models for the critical speeds are missing.

2 *Fundamentals of wetting*

3 Experimental details

The experimental rig built for the current thesis is described in section 3.1 while the liquids and sample materials are introduced in subsection 3.1.1. Subsection 3.1.2 gives an overview over possible wetting measurement techniques and the techniques used in this thesis. This chapter concludes with section 3.2, describing the data post-processing applied to the measurement data.

3.1 Experimental setup

The design goal of the experimental rig used in this thesis was a general purpose dipping experiment which can be used for various liquids, sample and movement kinematics. These broad possibilities were not only intended for this thesis, but also for future use of the test rig for investigating more complex wetting phenomena. It was desired to foresee different kinematic dipping movements, for example movements with constant acceleration and with superimposed vertical rotation. All movements are to be performed long enough to allow analyzing steady state situations, i.e. after the initial acceleration. This capability demanded a strong linear motor moving over a large distance, while being modular extendable. These specifications were therefore instrumental in defining the test rig.

Fig. 3.1 and Fig. 3.2 show simplified 3D renderings of the experimental rig used in this thesis. The rig is designed to be modularly expandable and serves for a variety of dipping experiments. Additional modules for future measurements are designed in the scope of this thesis and are presented in this section.

3 Experimental details



Figure 3.1: A simplified 3D rendering of the experimental rig, basic CAD model courtesy of Frank Plückebaum.

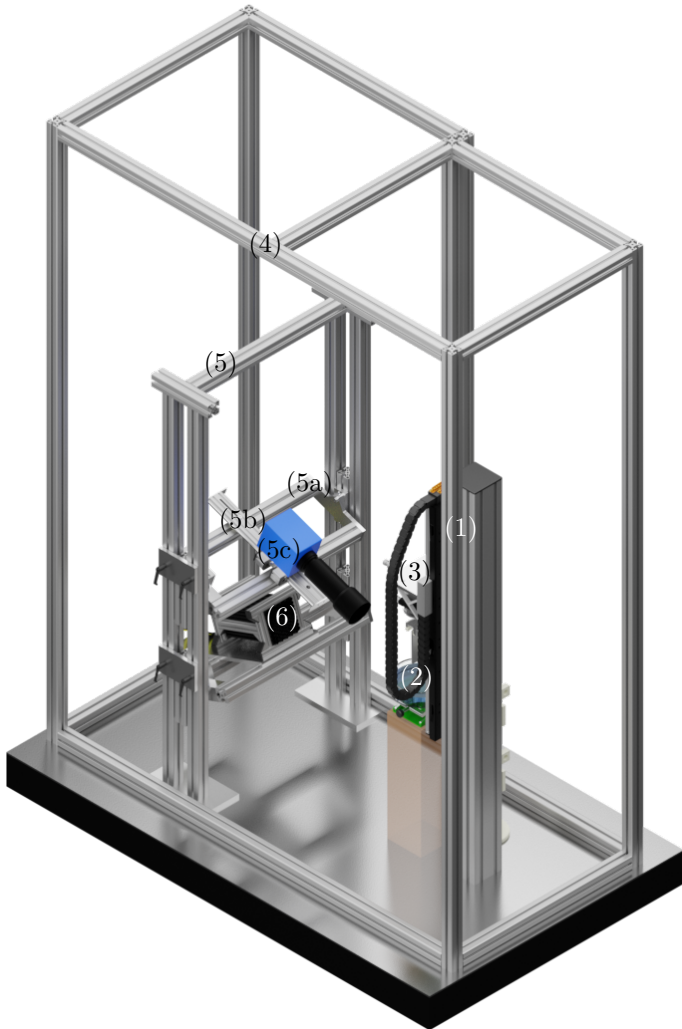


Figure 3.2: A simplified 3D rendering of the experimental rig observed from a second perspective, basic CAD model courtesy of Frank Plückebaum.

3 Experimental details

Linear motor

The central part of the experimental rig is the vertical pillar with the electro-pneumatic linear motor, (1) in Fig. 3.1 and Fig. 3.2. This motor construction was chosen in order to allow high sample weights up to 15 kg and long samples up to 400 mm length. Usually the preparation of samples becomes increasingly more difficult with their length, therefore, shorter samples are preferable. However, long samples become necessary for high speed forced wetting/dewetting measurements in which steady-state conditions should be reached before the whole sample was either dipped into or pulled from the liquid pool (2).

The electro-pneumatic linear motor is capable of performing smooth movements in a speed range of 0.01 to 500 mm/s and accelerations of up to 20 m/s^2 , while at the same time repeatedly reaching the same positions on its 408 mm long track with a precision of $\pm 0.15 \mu\text{m}$. [51] These abilities originate from the hybrid nature of the linear motor system. The core of this motor system is a PI LMS-180 (from Physik Instrumente (PI) GmbH & Co. KG, Germany) linear stage with a moving platform connected to a 408 mm long track via recirculating ball bearings. This motor is the mechanical base of the motor system. It employs an incremental encoder for position regulation and is driven by an iron-less magnetic direct drive. It had to be equipped with a modified controller unit to be initialized and used vertically. This motor gives the speed range and precision of the experimental rig, but due to its magnetic direct drive it tends to overheat fast in vertical use. When the current turns off due to failure, overheating or an emergency shutdown, the motor falls down unrestrained, leading to a possible destruction of parts of the experimental rig and the motor itself. To reduce this danger, prevent overheating and increase the maximum possible sample weight, a pneumatic cylinder was connected to the electric linear stage, providing a constant upward force.

To avoid introducing any jerking motion into the motor movement, a low friction pneumatic cylinder with a graphite piston running inside a glass

tube was ordered in a special size to fit to the electric motor. This AIRPEL Plus MP 16 S 420.0 NX cylinder (from Airpot Corporation, United States) [52] with a working volume of approx. 0.0811 is connected to an air tank with a volume of 11.81. This tank itself is connected to a pressurized air supply which is filtered several times to avoid oil reaching the pneumatic cylinder. The pressure in the tank is controlled by a mechanical valve, which is adjusted to the value needed in order to cancel out the dead weight of the sample and all moving parts of the motor combination. While in theory the mechanical pressure valve should bring more air to the cylinder when it is extending and blow out air during a retraction, the mechanical hysteresis of such a valve is too high to adequately react to cylinder movements. For this reason the air tank in between the valve and the cylinder works as pressure buffer, supplying the cylinder with a constant air pressure regardless of its position. The tank amounts to the total volume behind the pressure valve, therefore, the position of the cylinder (with its more than 145 times smaller volume) does almost not affect the total volume and hence the air pressure. A more common way, recommended by PI, is an active computer controlled air regulation at the cylinder, creating a constant pressure independent of its position. While this method could be applied in the experimental rig, the chosen self-regulating tank solution has an higher fail-safe level because it does not need computer control and two active valves to work.

Clamping module

Fig. 3.3 shows photographs of three different modules which can be connected to the moving platform of the linear stage ((3) in Fig. 3.1 and Fig. 3.2). The left image shows the latest version of a general purpose sample clamp, which was used for most experiments in its different versions. Its general clamping mechanism allows a versatile use with nearly every kind of sample fitting into the clamping slot of 30 mm width. The mechanics above the actual clamp allow to correct the sample tilting around all three axis, precisely rotate the sample around the vertical axis and change its distance towards the camera. The clamp is covered with PP (Polypropylene, in white) to avoid scratches on metal samples and, with a change of the 3D printed PP part, to allow the shape of

3 Experimental details

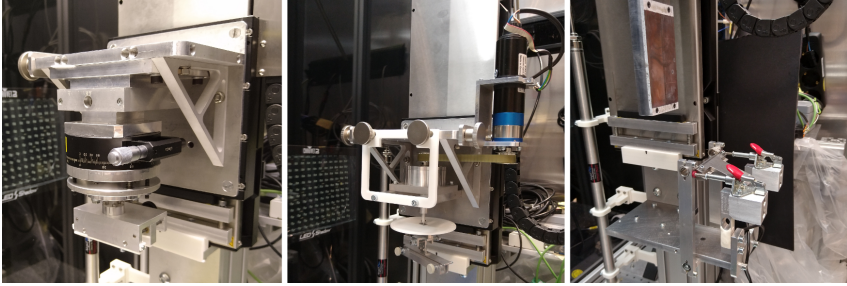


Figure 3.3: Left: The latest version of the sample clamp in use.
Center: The first version of a vertical rotation unit.
Right: A gravure printing test module.

the clamp to match to any sample. For very sensitive or dirty (e.g. liquid infused surfaces) samples the clamp can be covered with a thin PE (Polyethylene) foil or other material to protect the sample and the clamp from scratches and contamination. Fig. 4.21 shows the use of PE foil to prevent the contamination of the clamp with silicone oil rising up the sample.

In the center image of Fig. 3.3 an additional module for superposed rotational movement around the vertical axis is shown. This module is intended to be used with cylindrical samples to study the effects of forced wetting with movement non orthogonal to the contact line direction. The module is driven by a 3890 H024CR-2016 rotational motor [53] through a 38/2S 14:1 planetary gearing [54] with an IE3-512 encoder and a SC 5008 S 3531 speed controller [55] programmed by a SC 2804 (6501.00096) programming adapter [56] (everything by Dr. Fritz Faulhaber GmbH & Co. KG, Germany). The module was tested in this thesis and the clamp proved not to be stable enough to withstand unbalances during rotation. While non-orthogonal forced wetting is an interesting topic with few existing literature references, there was plenty of new knowledge to gain during this study without invoking the rotation movement. As a result, after initial tests, the rotation unit was not used anymore and the clamp

still has to be revised for future use.

The image on the right side of Fig. 3.3 shows a different module, replacing all parts mounted to the linear stage. This module mimics the wetting inside a gravure printing machine by vertically dipping a gravure printing plate into a pool of liquid, pressing a doctor blade with a given angle and force against the gravure printing plate and pulling the plate up again. These process steps usually happen on a cylindrical gravure printing role when it submerges its surface on one side while on its other side a doctor blade scrapes away superfluous liquid before the printing role comes into contact with the printed surface (e.g. paper). The pressure at the doctor blade is measured with two 166H load cells (from BCM SENSOR TECHNOLOGIES bvba, Belgium) [57]. The surface of gravure printing roles consists of a thin metal sheet which makes it possible to flatten it out onto this linear setup, to observe the wetting and dewetting processes taking place on these structured surfaces. This module was constructed in a student group work [58] and built making only minor changes to their construction plans in order to ensure fitting of all parts and enabling one complicated part to be at least producible using direct metal laser melting (DMLM). Some preliminary measurements were performed with this gravure printing module, but no further experiments have been performed.

Liquid pool

The liquid pool ((2) in Fig. 3.1 and Fig. 3.2) is a completely modular part of the experimental rig and a variety of different pools with different sizes and shapes exist for different types of measurements. Two lifting tables support smaller pools, so that neither the motor nor the camera and lighting setup have to be adjusted to different pool heights. Most of the pools are made of borosilicate glass in order to withstand more aggressive cleaning procedures, while some simple pools are also fabricated from acrylic glass (Poly(methyl methacrylate)) plates connected by glue. Two special pool shapes are presented in Fig. 3.4.

3 Experimental details



Figure 3.4: Left: The wide surface/small volume pool.
Right: The overflowing cylinder pool.

The left pool shows a sharp radius transition. This sharp transition is used to reduce the overall liquid volume needed to fill the pool while at the same time providing a sufficiently deep pool with a large surface. A large pool surface has two benefits for wetting measurements. The change in pool height due to displacement of the sample is reduced and what is more, the interaction between pool walls and sample surface in form of capillary forces and reflecting liquid waves is also reduced. A picture of this pool being used for a measurement can be seen in Fig. 4.21.

The pool shown on the right side of Fig. 3.4 is an overflowing cylinder as known by literature [59, 60]. It can be used to maintain a fixed surface height when dipping or redrawing very long samples. Alternatively, it can be used to constantly renew the liquid surface if working with surface active substances. In both cases a pump regulating the inflow has to be installed, which is present in the experimental equipment.

Isolation and damping

To compare experiments in different vapor atmospheres it would be necessary to control temperature, pressure and the type of gas inside

the experimental rig. Most electrical systems (e.g. the linear motor) are not able to operate in wet or hot conditions. Hence sample and liquid pool would need to be located inside a separate test chamber to protect the electronics outside of it. To maintain temperature, pressure and gas/vapor composition inside this chamber all connections to the outside would need to be sealed, but vacuum tight sealings can impede the smooth motor movement. In general, this kind of small, pressure tight test chamber limits the flexibility of the test rig. Hence no sealed test chamber is used and the atmospheric conditions are given and controlled by the air conditioning in the laboratory. To provide a calm atmosphere without disturbances due to air recirculation or moving doors, the entire test rig is encased in a large acrylic glass box ((4) in Fig. 3.1 and Fig. 3.2).

Vibrations can have a strong impact on wetting phenomena, especially when pinning is involved. Due to this, the experimental rig is built on an optical table to be able to damp external vibrations. The drawback of this damping is the possibility of small movements of the table when the air cushions of the table are blown up. This can lead to additional oscillations when the linear motor stops and its impulse is transferred to the table. To avoid this inertia induced oscillations, the optical table was not inflated during the experiments but still was damping vibrations due to its high inertia and passive damping abilities. A second source of vibration are the motor pillar ((1) in Fig. 3.1 and Fig. 3.2) and the camera tower (5) which are made of aluminum, combining high stiffness and low damping. This leads to vibrations due to motor movement, camera cooling fans and similar sources. In 1990 Panossian suggested a new damping method which he calls "Non-Obstructive Particle Damping" [61]. This method makes use of the friction between spherical particles, which are inserted into hollow volumes of the vibrating part to be stimulated to move against each other. This technique was later adapted to reduce the noise of roller coasters by filling their cylindrical rail tubes with sand [62]. The motor pillar (1) has a hollow core which is filled with sand, resulting in a sufficient damping effect. The same technique was applied on the camera tower before it was updated to a version using smaller but solid aluminium profiles. This latest version of the camera tower is less prone to vibration since the horizontal camera floor (5a) is connected

3 *Experimental details*

to four different vertical profiles which mutually hinder them from free oscillation. The camera track (5b) is connected to the horizontal floor via two solid PP pieces, which add a minor amount of damping. The camera itself sits on an 8 mm rubber mat on the camera slide (5c), which isolates it from the camera tower and absorbs vibrations.

3.1.1 Liquids and samples

Liquids

The majority of literature uses water for wetting experiments. This can be traced back to several facts. Water most probably is the best documented liquid, it is (when purity does not matter) easy to obtain, it has a simple Newtonian viscosity and it is important for many real-world processes. On the other side important drawbacks of water are frequently ignored. Simple tap water and highly purified water show different surface tensions and highly purified water tends to lower its surface tension over time. Tiny amounts of grease and oil (e.g. from human skin) can be sufficient to lower the surface tension of highly purified water by a significant amount. Surface active substances can also have similar effects to less pure water. Water has a strong tendency to pinning, which correlates to its high surface tension. Hence, the surface tension of water has to be constantly monitored to detect contamination effecting the experimental results. In this thesis the pinning of water was found to be predominant on the samples, obscuring the wetting behavior in a way that it could not be used for most measurements. However for [63] a supersaturated tenside solution in water was used on a smooth sample, where it showed no visible pinning effects but its rise height indicated a general pinning of the contact line.

Another very common liquid is ethanol. It is well documented, Newtonian, has no tendency to pin and good wetting properties on most surfaces. Its major drawback is its high vapor pressure at room temperature. This leads to omnipresent evaporation which often, especially close to a contact line, cannot be neglected. Because of this

unpredictable evaporation effects ethanol was not used in this study except for test measurements and cleaning processes.

A popular binary liquid with adjustable viscosity are mixtures of water and glycerol. These mixtures are hygroscopic and because of their usually high viscosity they tend to build layers or streaks of different mixture ratios when samples are dipped into and pulled out of them. The pinning tendency raises with higher amounts of water. Because of all these effects the mixtures have to be monitored permanently and used with great care to ensure good measurement results. As for pure water, the pinning proved to be too strong on the samples used in this thesis and hence these binary mixtures were avoided.

More exceptional for wetting phenomena is the use of mono ethylene glycol. It was tested as an alternative for ethanol and glycerol. It has a higher viscosity than ethanol but does not evaporate noticeably at room conditions. Its pinning tendency turned out to be lower than that of pure water or water/glycerol mixtures but still resulting in a scattering of measurement data which can obscure important effects. Hence, mono ethylene glycol was not used for published measurement data.

Silicone oils (Polydimethylsiloxane, PDMS) allow for adjustable viscosity, have a very low tendency to pin, do not evaporate at room conditions (when they are above a viscosity of approx. $5 \times 10^{-6} \text{ m}^2/\text{s}$ or 5 cSt) and wet most materials very well. For slower speeds and lower viscosities silicone oils can be assumed to be Newtonian. While all these properties make them perfect liquids for most wetting experiments, their major disadvantage is their chemical stability. After applying silicone oil to a surface it is difficult to remove it again. Normal cleaning substances like soap water, ethanol, acetone or isopropanol are not able to remove silicone oil from a surface. One cleaning method is a bath of xylene which will remove silicone oil when given enough time to work. Due to the dangerous nature of xylene this method was not used in this thesis. Another cleaning method was found by the use of Tickopur R 33, which is a commercial cleaning solution (from DR. H. STAMM GmbH Chemische

3 Experimental details

Fabrik, Germany) for ultrasonic baths. After five minutes ultrasonic cleaning in a Tickopur R 33 solution, rinsing with water, ethanol, acetone and water the samples usually showed no sign of remaining silicone oil (for $20 \times 10^{-6} \text{ m}^2/\text{s}$ or 20 cSt silicone oil). However, when silicone oil with a viscosity of $100 \times 10^{-6} \text{ m}^2/\text{s}$ (or 100 cSt) was used, the samples remained clearly hydrophobic after cleaning. Repeated cleaning did improve this situation but was not sufficient to gain a clean surface. Additional wetting with lower viscosity silicone oil and a subsequent cleaning showed a positive effect on removing the underlying layer of higher viscosity silicone oil from the surface.

Some tests with fluorescent liquids were performed during this thesis. Fluorescence paired with an UV filter (cutoff wavelength of 500 nm) filtering out the exciting near UV light (405 nm) allows a clear optical separation between wetted and dry parts of the sample. Two fluorescent substances were found to be most efficient in combination with the tested liquids. Fluorescein showed a good emission in water compared to other fluorescent substances, while meanwhile being only of minor danger to health and environment. For silicone oil the best fluorescent substance which was found is nile red, emitting a yellow light when used in silicone oil. The emission of nile red in silicone oil is much weaker than the emission of fluorescein in water. Since this thesis is mainly dealing with silicone oil and avoiding the use of water, the low signal-to-noise ratio (SNR) and the necessity of repeatedly preparing equal fluorescent mixtures are considered disadvantageous wherefore fluorescence finally was not used in the experiments.

Literature values for the most important physical properties of the liquids mentioned above are listed in Table A.2 to give an overview of the different liquid characteristics.

Samples

Previous experimental work of Manukyan [14] observed the wetting phenomena at arrays of millimeter scale pyramids. The wetting patterns

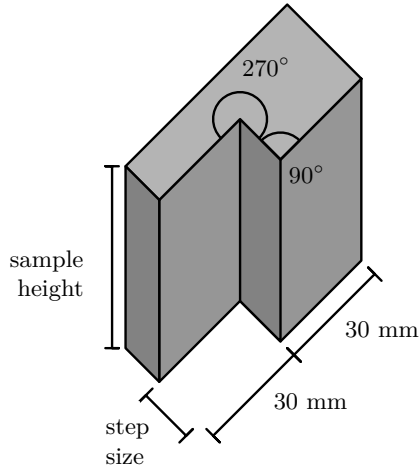


Figure 3.5: The sample geometry used for the majority of experiments in this thesis. Image adapted from [64].

on these arrays proved to be highly complex and different wetting phenomena were interacting with each other. In order to enhance the basic understanding of single phenomena and simple interactions among them, a simplified geometry was sought. Two basic geometries are very popular in literature. One geometry are capillary tubes with edges (often rectangular tubes) [65–74]. The second geometry are grooves (often triangular or rectangular) [13, 73, 75–89]. Fig. 3.5 depicts the geometry finally chosen to be used for the majority of experiments in this thesis. The geometry consists of three vertical walls connected to each other at right angles with one edge being convex and one edge being concave. Usually the vertical edges at which the wetting behavior is investigated are referred to as corners in the literature and in the articles published by the author. While calling them corners is a widely accepted practice, in this thesis they are called edges to clearly distinguish them from the corners at the top and at the bottom, at which three different edges meet. When the length of the center wall, called step size, is changed, the

3 Experimental details

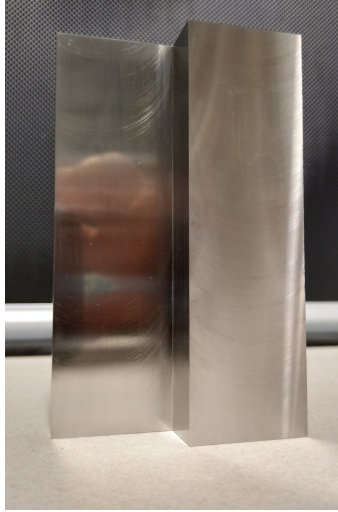


Figure 3.6: A stainless steel sample with the geometry shown in Fig. 3.5, a step size of 15 mm and a height of 100 mm.

phenomena at the inner and outer edge can be observed either separated or coupled.

The first set of samples used for the measurements published in [64] have a sample height of 60 mm and different step sizes in a range from 50 μm to 15 mm. They are milled from aluminum alloy 2024 (AlCuMg2) which, at solitary points, shows degeneration effects when continuously cleaned with Tickopur R33. These effects are a whitening of the aluminum and seem to be triggered by small surface defects. This degeneration did not appear directly on the analyzed areas of the samples and no quantifiable difference in silicone oil wetting is observable at degenerated areas of the samples.

The average roughness of these samples is in the range of 2 μm , but despite this low roughness height, non-isotropic pinning effects are visible

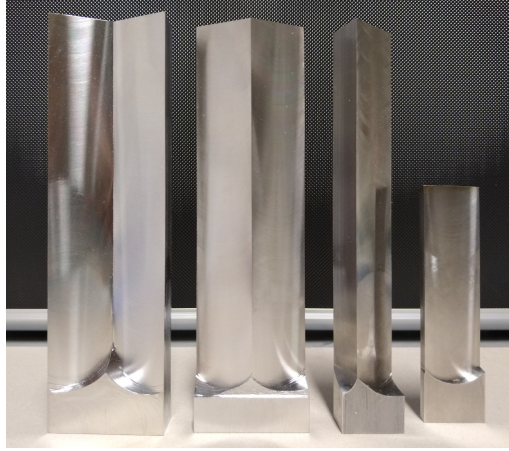


Figure 3.7: Stainless steel samples with only one analyzed edge, but different edge opening angles.

along the milling grooves except for ethanol and silicone oil. A second set of samples (used for [90] and [63]) exhibits the same geometry using a sample height of 100 mm. This set is milled from 1.4404 stainless steel which proved to be resistant against cleaning with Tickopur R33. One sample from this set is shown in Fig. 3.6. As for the first set, the second set can be only used in combination with silicone oil to prevent pinning at the milling grooves.

To analyze the wetting behavior of different edge angles than 90° or 270° another set of 1.4404 stainless steel samples was milled. These samples have different edge angles, like 135° , and a total height of 200 mm (including a flat clamping area of about 20 mm) to prolong the experimental run time for forced wetting measurements. The samples are shown (upside down) in Fig. 3.7. These samples are designed to analyze the effect of a single edge and no interaction phenomena, so they do not follow the shape sketched in Fig. 3.5. An image of the 135° sample used in an experiment is shown in Fig. 4.21.

3 Experimental details

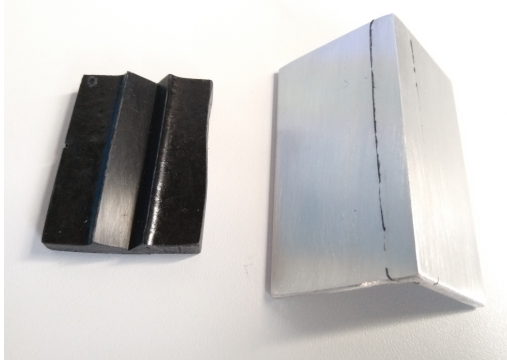


Figure 3.8: Left: The PLA sample used for validation in [63]. Right: The aluminum profile used to cast the sample with visible PLA remains where its meniscus broke off.

Test were performed in order to build edge geometries from smooth glass plates. Connecting different glass plates either resulted in very fine cavities in between the contact faces (affecting the rivulet rise in the edge) or, when connected by glue, resulted in samples which could not be cleaned without dissolving this glued connection. Glue filled out most of the cavities between the glass plates but either left some cavities open or squeezed out into the edge since it was not possible to control the application of glue down to a level of tenths of micrometers. Moreover, the observation of a transparent liquid on a three-dimensional transparent sample with superposing refractions complicates optical measurements.

For the analytical solution proposed in [63], an experimental validation of a liquid not forming full rivulets at the edge of a sample was needed. For this experiment, the combination of PLA (Polylactic acid) and a supersaturated tenside solution was found to show an advancing contact angle of about 52° which is above the Concus-Finn value (Eq. (4.1)) for

a right-angled edge, which is 45° . This PLA sample (shown on the left of Fig. 3.8) was cast from a right-angled sharp aluminum profile (shown on the right of Fig. 3.8) which was partly immersed into PLA pellets before slowly heating everything up to 200°C and letting the parts cool down over night. This resulted in a solid PLA negative with a relatively sharp edge (edge radius approx. $442\ \mu\text{m}$) replicating the aluminum profile down to small scratches on its surface, see Fig. 3.8.

For the experiments discussed in Chapter 5, different materials and surface treatments were tested to create reproducible artificial surface roughness. A popular method for creating artificial roughness is sandblasting [91, 92] with the parameters: Sand shape, size and material, air pressure, blasting distance, blasting direction and blasting duration. Sandblasting was used in combination with aluminum alloy 2024 (AlCuMg2) surfaces. Several tests showed that it was not possible to repeatably treat surfaces in a way that their roughness structure was equal in terms of roughness parameters (EN ISO 25178) and in terms of experimental wetting results. The sandblasted surfaces showed a great variance in roughness and the stochastic differences observed at wetting experiments prevented the gathering of general information about the interaction between wetting and roughness. While the average roughness for these sandblasted samples was in the order of micrometers, the maximum surface peaks were one order of magnitude larger, leading to a more hierarchical than monotone surface roughness. [93, 94]

In order to achieve small surface roughness, aluminum samples were either polished or milled flat. As for the geometrical shaped samples mentioned above, the milled surfaces showed milling lines which triggered pinning for liquids prone to pinning effects and led to non isotropic wetting. Fig. 3.9 shows one sandblasted, one milled and one polished sample.

Another method for the creation of artificial rough surfaces is the use of inherent surface roughness resulting from 3D printing processes. At first the roughness of selective laser sintered (SLS) PP parts was utilized as

3 Experimental details



Figure 3.9: Three aluminum samples used for roughness measurements. From left to right: Sandblasted, milled, polished.

artificial roughness. In this 3D printing method plastic powder is flattened out in a plane and a laser selectively fuses parts of the powder together. Afterwards a new thin layer of powder is laid above the last one and selectively fused to it again. It was found that the roughness of SLS printed parts is even higher than the roughness obtained by sandblasting. Furthermore, the roughness mainly depends on the PP particle size for the laser sintering process and hence cannot be easily varied. Examples of SLS printed parts are all white parts of the clamps shown in Fig. 3.3. Another popular 3D printing method is fused filament fabrication (FFF) in which liquefied plastic filaments are used to print stacked layers of an object. The height of these layers can be freely adjusted, which allows the repeatable production of different surface finishes. The surfaces of FFF prints consist of horizontal round ridges forming the different layers, with grooves in between them. Fig. 3.10 shows such a sample, for which the horizontal ridges as well as some superposed waviness due to mechanical restrictions



Figure 3.10: A PLA sample printed with fused filament fabrication. The horizontal layers as well as a diagonal wavy pattern due to mechanical restrictions (timing belt) of the 3D printer are visible.

(timing belt) of the 3D printer are visible. The exact geometry is difficult to describe, since the filament is compressed during printing, melting layers together and deforming the ridges to an elliptic shape, which varies with layer height. The surface structure is therefore highly non-isotropic and the effects of the structure at different tilting angles can be analyzed. In general, such highly ordered geometrical structures are not referred to as roughness anymore but as geometrical surface structure. The FFF prints are made with PLA, which can be cleaned using ethanol. Acetone or the Tickopur R33 ultrasonic bath cannot be applied for cleaning, since PLA is not chemically resistant against these substances.

3 Experimental details

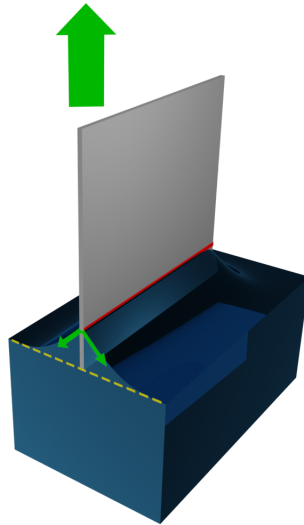


Figure 3.11: The measurement principle of a Wilhelmy tensiometer shown in cross section. The sample plate stays at the pool level height (dashed yellow line) while the liquid forms a meniscus with a nearly straight contact line (red). The liquid surface tension exerts a force along the contact line (small green arrows) in a direction given by the contact angle. The large green arrow above the sample symbolizes the force needed to balance the contact line forces.

3.1.2 Data acquisition

Force measurement

Fig. 3.11 shows the principle of Wilhelmy tensiometers [95]. A platinum-iridium plate of known dimensions is immersed in and pulled out of a liquid pool until its bottom is at the same height as the undisturbed liquid surface (dashed yellow line). The contact angle of most liquids on platinum-iridium is close to zero, so that a liquid

meniscus (contact line in red) is formed, vertically pulling down the plate (small green arrows) due to surface tension. The dimensions of the plate and hence the length of the contact line is known, which, assuming a contact angle of zero, allows a direct calculation of the surface tension from the measured force at the platinum-iridium plate (large green arrow above the plate). Such a device (DCAT 25 from DataPhysics Instruments GmbH, Germany) was used to measure surface tensions in this thesis. Wilhelmy tensiometers can also be used in the opposite direction by using liquids with known surface tension and samples with an unknown contact angle. The vertical part of the force exerted by the meniscus is equal to the cosine of the contact angle, which thus can be measured in this manner.

For this thesis it was planned to implement a force sensor into the experimental rig for estimating average contact angles of structured surfaces by using the inverted Wilhelmy measurement method. Because of a large discrepancy between necessary measurement precision and sample weight, experiments with force measurements were not continued after initial tests. More details are described in the Appendix A.1.

Another form of force measurement was implemented in the gravure printing test module, shown on the right side of Fig. 3.3. In this module two bending beams are used to measure the contact force of the doctor blade on the gravure printing plate.

Optical measurement

The primary measurement instrument of the test rig is a pco.edge 5.5 camera (from PCO AG, Germany) [96] (in blue on top of (5c) in Fig. 3.1 and Fig. 3.2), which is monochrome with a high dynamic range (HDR) of 16 bit (65536 brightness levels) and 5.5 megapixels (2560 x 2160 pixels). This camera was also used for the fluorescence tests described in subsection 3.1.1 for which a LED panel with near UV LEDs (405 nm) with a total power of 48 W was used (from Chauvet DJ, United States) [97].

3 *Experimental details*

For the majority of measurements the camera was used in combination with two white light sources of the type Constellation 120E (from Integrated Design Tools, Inc., United States) [98] with a color temperature of 6200 K, 22×10^3 lm and a beam angle of approx. 15° . One of these two light sources was further directed with a custom built light commutator ((6) in Fig. 3.1 and Fig. 3.2) consisting of black anodized aluminium pipes (\varnothing 10 mm (outside), wall thickness 0.5 mm, 200 mm length) which are closed-packed and placed in front of the light source in order to absorb light rays non-normal to the light source, leaving only a tightly directed light bundle. This modified light source was placed below the camera and tilted to be directly reflected into the camera from the sample surface. With this configuration, transparent liquid menisci on the sample become visible due to their refraction disturbing the direct bright reflection. The second white light source was mounted on a flexible arm and used variably in order to enhance the contrast at relevant areas for each measurement.

Some measurements, mainly for other projects, were performed using background lighting [99, 100] (for further explanation see subsection 3.2.3). For these experiments a modified LED panel placed between sample and linear motor was used for illumination. This panel has a power of 20 W and a color temperature of 4000 K. The original LED panel fluctuated with the mains frequency (50 Hz) while the usual frame rate of the pco.edge 5.5 is 49.997 Hz leading to a dominant illumination beat in the recorded video material. An additional capacitor added to the LED panel eliminated these fluctuations, making it usable in combination with the pco.edge 5.5 camera.

Two lenses were used in combination with the pco.edge 5.5. The general purpose objective was a Milvus 2/100M (from Carl Zeiss AG, Germany) with a focal length of 100 mm, an aperture from f/2.0 to f/22 and 9 lenses leading to a resolution of approx. $20 \mu\text{m}/\text{px}$. For punctual high resolution images (e.g. on gravure printing plates) a Navitar objective with a zoom factor of 12 was applied.

For the Bachelor thesis of Weidler [94], lighting with laser light sheets was tested to measure dynamic contact angles on rough surfaces by means of refraction from the meniscus (for further explanation see subsection 3.2.3). While the refraction is clearly visible and in theory allows the calculation of the contact angle, the generated light sheets have proven to be too fuzzy (approx. 1 mm in width) and the reflections of the rough surfaces too scattered to define refraction angles precisely enough to make practical use of this method. Hence this laser lighting method was not further used after initial tests.

Environmental sensors

The environmental conditions around the test rig are controlled by the laboratory air conditioning system, nevertheless they are monitored by two sensors in the test rig. Room temperature, moisture and dew point temperature are measured with a SHT75 sensor (from Sensirion AG, Switzerland) [101] selected from [58] with a temperature error of about $\pm 0.3^\circ\text{C}$ and a moisture error of about $\pm 1.8\%$ (the dew point temperature is calculated from measured temperature and moisture). The total pressure around the test rig is measured with a precision of $\pm 1.5\%$ [102]. Additional stainless steel covered PT 100 sensors (class B) (from B+B Thermo-Technik GmbH, Germany) [103] are available for temperature measurements inside the liquid pool, while plastic covered PT 1000 sensors (class B) (from Heraeus Nexensos GmbH, Germany) [104] can be used to measure the sample temperature.

The total pressure sensor and the 31E-002N5-1m force sensor are connected to a NI USB-6002 AD converter (from National Instruments Corp., United States) [105], which is also used to control the rotary motor shown in the center image of Fig. 3.3. A NI 9219 (from National Instruments Corp., United States) [106] is connected to the computer via a NI USB-9162 adapter and reads out the temperature values from the additional PT 100 and PT 1000 sensors.

3.2 Data post-processing

In order to enhance the visibility of the analyzed wetting phenomena, lighting and camera have to be adjusted differently for different measurements. Usually sample and camera are tilted and displaced towards each other in all three dimensions and a precise measurement of the angles and distances between them is technically not possible. Hence the camera images have to be calibrated during post-processing to receive quantitative data. The methods used for this calibration are discussed in subsection 3.2.1. Subsection 3.2.2 describes the filters proven to be useful for image enhancement in the measurements performed in this thesis. For the test measurements performed during the Bachelor thesis [94] some image processing methods have been used, which are explained in subsection 3.2.3.

3.2.1 Ray calibration

Target calibration

Fig. 3.12 demonstrates the principle of target calibration used for the measurements published in [64]. A target (a) with a known dot pattern containing a central bigger dot (hidden by the coordinate system in the figure) is filmed at two positions. The first position defines the origin and orientation of the local coordinate system while the second position (only differing in its translation into the local y axis (inverse normal of the target)) is used to measure the ray directions. From the known y distance between these two positions and the dot positions in the camera images, the camera frustum (blue) can be calculated. For this calculation the dots on the target images are automatically detected by binarization followed by connected-component labeling and their sizes and relative positions are used to detect their most probable position in the dot pattern; hence, their local x and z coordinates in the target planes. This defines the mapping of the camera image (b) pixels onto the first target plane. Afterwards the pixel positions of every visible dot from the first target image are interpolated onto x and z coordinates on

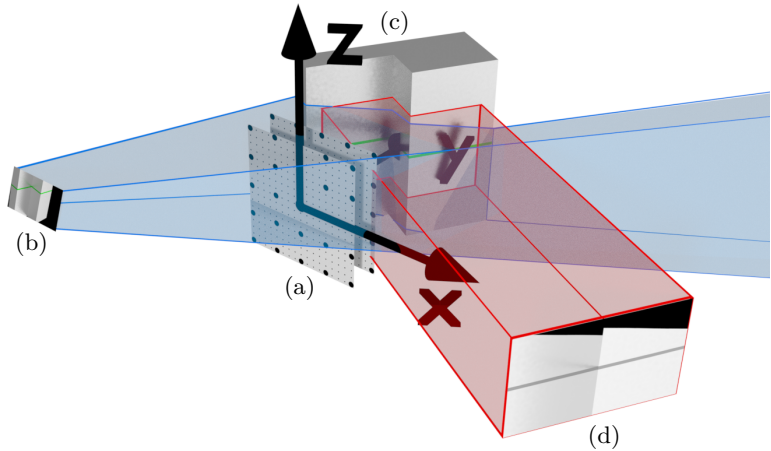


Figure 3.12: The principle of the target calibration. A target (a) is filmed at two different positions in a known distance and rotation to the sample (c). With the target images the frustum (blue) of the camera (b) can be calculated and used to transform the camera images into perspective free mappings as visible in (d). Image adapted from [107].

the second target plane, resulting in two 3D positions projected onto the same camera pixel. From this, the camera ray directions from the first target plane into the 3D scene are known. To make use of these ray directions the position and orientation of the sample (c) towards the target origin has to be known. This can be achieved by mounting both, the target and the sample, to the same clamp system with adjustable rotation and translation into different axes, so that the position and rotation can be mechanically adjusted. With this information the pixels of the camera image (b) can be projected, starting from the mapping onto the target plane (a), into the calculated ray directions. Due to the known geometry of the sample (c) the intersection of its surface with the camera rays originating from every pixel can be calculated to receive the real-world 3D position of every point of the sample observed by the camera. A second virtual orthographic camera (d) can be used to obtain

3 *Experimental details*

undistorted images of the sample with fixed pixel to meter ratios, which can be analyzed quantitatively.

In Fig. 3.12 a green horizontal line is drawn on the sample (c). In the camera image (b) this line can be seen jagged because of the tilted perspective. After the image transformation onto the orthogonal camera (d), observing the sample from the front, the line (here in dark gray due to monochrome post-processing) can be seen horizontal again.

This target calibration method exhibits several drawbacks during active use and due to these, it was later replaced by other methods. The imaging of both target positions and the measurement itself proved to be difficult. The focal point of the camera and its positioning has to be adjusted to the sample and wetting situation before the calibration, since the camera parameters are not allowed to change between the calibration and the final measurement. After this initial uncalibrated imaging tests the sample has to be removed and cleaned again while the target has to be mounted. The two target positions have to be found in a way that they are separated from each other as far as possible, since the precision of the ray vector detection rises with the distance, but must still be close enough to the focus of the camera to be imaged sharp enough for post-processing. Simultaneously, the target has to fill out nearly the entire camera image and its central big dot, giving the origin of the coordinate system, has to be visible in the camera at both positions. Additionally, the brightness level of the target images turned out to be difficult to adjust to a constant level which is necessary for a good binarization result. Dot detection errors in the order of single pixels proved to have a major impact onto the resulting camera ray directions which can be partially counteracted by filtering the ray directions. The filtering algorithm applied assumes the dots in the different rows and columns of the target to form straight lines, with approximately constant distances among them, in the camera images. This assumption is close to reality since the utilized camera objective has a small opening angle, leading to only minor non-linear distortion. Least squares fitting is used to find the starting point, direction and distance among the dots of every row and column. These starting points and

direction vectors are used to recalculate the dot positions in the image by setting

$$\vec{r}_{s,z} + x \vec{r}_{d,z} = \vec{c}_{s,x} + z \vec{c}_{d,x}. \quad (3.1)$$

In Eq. (3.1) $\vec{r}_{s,z}$ is the starting position (in pixels) of the row at height z and $\vec{r}_{d,z}$ is its direction between two adjacent dots (in pixels). Respectively $\vec{c}_{s,x}$ and $\vec{c}_{d,x}$ are the starting position and direction vector of the column at position x . In theory both sides of Eq. (3.1) should be identical for the x and z coordinates of a point. But since the origin and direction of each row and column are fitted independently, they do not match exactly. Hence, the geometrical intersection of the fitted row and column lines in the camera image is used as new image position of the dot instead. All dot positions are recalculated using these intersections, which cancels out many minor detection errors. Further explanations of the target calibration are given in the following reference [107].

A drawback of target calibration are the positioning errors between the two target positions and the sample position. Even with a stiff sample clamp small errors occur e.g. due to the mechanical movement and rotation of the mount. These errors directly affect the calibration and add a noticeable amount of uncertainty.

Light field calibration

Based on the PhD thesis of Diebold [108], tests were done to detect the orientation of the sample by light field calibration. This technique proved to be error-prone in combination with the small opening angle of the used objective and hence was never applied to published measurements. Further details can be found in Appendix A.2.

3 Experimental details

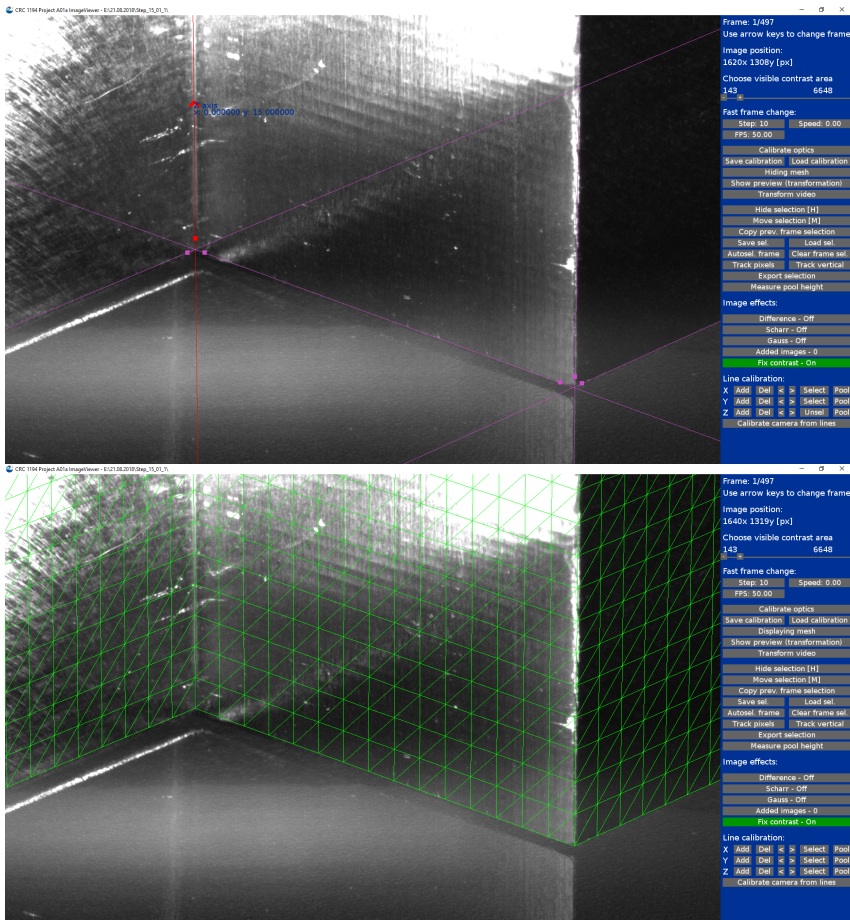


Figure 3.13: Top: A screenshot of the post-processing tool showing an image of a sample and the marked edges for calibration. Bottom: A 3D model of the sample projected onto the image using the calibration from the top.

Line calibration

Following the unsuccessful light field calibration test, a completely new calibration method was developed in order to improve the precision of the measurements. The samples shown in Fig. 3.5 consist of right-angled edges. These geometrical characteristic can be used for a simpler and more accurate calibration method shown in Fig. 3.13. No additional target images or other additional measurements are necessary for this calibration. One corner of the sample is defined as the origin of the local coordinate system orientated along the sample edges. As visible in the top of Fig. 3.13 the edges of the sample are marked in the camera image using two control points per edge. For each edge two coordinates are known from the sample geometry, e.g. for the labeled edge in the top of Fig. 3.13, pointing in the z direction, its x and y position relative to the chosen origin of the coordinate system (the corner at the bottom right) are known. The actual calibration fits a virtual camera with the original sensor size and resolution and seven parameters (3D rotation, 3D position and opening angle) to show each marked edge at the same image position as on the real camera image.

At corners of the sample where different edges meet, the full 3D position of the intersection points is known, e.g. when a x axis with known y and z position intersects a y axis with known x and z position, this intersection happens because of identical z values. The x and y coordinates of the intersection point are given from both edges. When three edges meet at a corner, the marked lines in the post-processing often do not intersect at exactly the same point, but form small triangles with three different intersection points. Instead of averaging these three points into one central point, they are handled as separate points in the post-processing, giving more weight to corners built from three edges instead of corners with only two visible edges for calibration.

To ensure convergence for the calculation of the seven camera parameters, a starting solution has to be generated. The first step is the generation of a starting solution for the rotation of the camera, assuming an

3 Experimental details

orthographic projection. Due to the orthographic assumption the problem complexity is reduced and becomes independent of the unknown camera position and opening angle. The pixel directions of all marked edges in the camera image are measured and unit vectors along the coordinate system are orthographically projected onto an infinite camera sensor plane to calculate their corresponding pixel directions. The rotation of the virtual sensor plane is then fitted, using the least squares error of the averaged edge directions from the camera image compared to the projected axes directions.

The starting solutions for position and opening angle can be calculated independent of each other or in a combined process. A separated calculation starting with the calculation of the position using an assumed (relatively high) camera opening angle proved to be more stable. A ray is sent out from the pixel position of each edge intersection and its length is averaged from the three lengths necessary to reach the x , y and z position of the intersection point. The resulting position difference in all three axes is then taken as an error vector. The same is done for the two control points of every marked edge in the two dimensions known of them. This results in three times the number of intersections plus four times the number of edges error values, which are used for least square fitting of the position and, either additionally or in a subsequent step, the camera opening angle. The starting solution gained by the previous calculations is used for the actual calculation of the camera parameters, which makes use of the same errors used for the fitting of the position and the opening angle but fits all seven parameters at once.

It has to be mentioned that the opening angle of the camera is not equal in both image directions, which would only be the case for a quadratic camera image. Instead it is used to describe the horizontal opening angle while the vertical spreading of the camera rays is scaled by the image size ratio. The following equations are used to model the camera ray in the coordinate system of the camera with y being the normal of the sensor plane:

$$\begin{aligned}
1. \quad ray_x &= \frac{pix_x - img_x/2}{img_x/2} \tan(\alpha_{cam}) \\
2. \quad ray_y &= 1 \\
3. \quad ray_z &= -\frac{pix_y - img_y/2}{img_y/2} \frac{\tan(\alpha_{cam})}{img_x/img_y} \\
4. \quad \vec{ray} &= \frac{\vec{ray}}{|\vec{ray}|}
\end{aligned} \tag{3.2}$$

In Eq. (3.2) \vec{ray} is the camera ray originating at the camera sensor and pointing into the 3D scene, \vec{pix} is the pixel position in the image, \vec{img} the overall image size and α_{cam} is the opening angle of the camera as defined (in 2D) in Fig. 3.14. The z coordinate of the camera sensor is pointing upwards while the pixel position y is pointing downwards, hence the pixel position y has to be inverted for the calculation of the z fraction of \vec{ray} .

This version of the line calibration was specifically designed for the right-angled samples mainly used in this study. Nonetheless it can easily be extended to allow the use of edges (or single points) with arbitrary directions but known real-world positions, which can be treated in the same way as the edges pointing in the directions of the coordinate axes.

Manual calibration

For the static rise height measurements in [63] none of the previous mentioned calibrations could be applied. The custom made PLA sample (Fig. 3.8) has an edge with smooth walls on both sides but no further straight edges due to manual cutting of the sample. Furthermore, the size of the walls on both sides of the edge is different, varying over the height and not known exactly. Hence, neither a precisely defined clamping position as needed for a target calibration nor straight edges as needed for a line calibration are given. This necessitates a manual calibration to measure the rise height in the edge, for which the tilting angle of

3 Experimental details

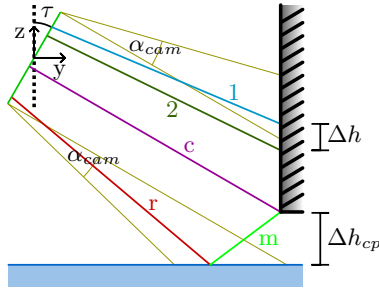


Figure 3.14: The 2D ray system used for manual calibration. The green line in the top left is the camera sensor tilted by τ and the yellow lines illustrate the outer perimeters of the camera frustum and its opening angle α_{cam} . The blue (1) and the darker green (2) lines show the rays to two points with a known height difference Δh . The purple (c) and the red (r) lines show the rays towards the lowest point of the sample corner respectively its reflection on the liquid. The light green line (m) is the mirrored reflection of (r) connecting the corner point and its mirrored image on the liquid.

the camera and its opening angle have to be known a priori. While the tilting angle of the camera can be measured, the opening angle, used for ray calculation, has to be estimated from values obtained by past line calibrations of similar setups.

The calibration is based on a 2D ray tracing system in a vertical plane through the camera and the edge of the sample with its vertical axis called z and its horizontal axis called y . This system is depicted in Fig. 3.14. A given image position \vec{pix} is mapped onto the vertically aligned camera sensor with

$$\vec{s}^* = \begin{pmatrix} 0 \\ -\frac{pix_y - img_y/2}{img_y/2} \frac{h_{sens}}{2} \end{pmatrix}, \quad (3.3)$$

using the image size \vec{img} and the real sensor height h_{sens} . Afterwards, the virtual camera sensor is rotated according to the camera tilting angle to receive the real-world starting position of the ray

$$\vec{s} = \begin{pmatrix} \sin(\tau) \frac{pix_y - img_y/2}{img_y/2} \frac{h_{sens}}{2} \\ -\cos(\tau) \frac{pix_y - img_y/2}{img_y/2} \frac{h_{sens}}{2} \end{pmatrix}, \quad (3.4)$$

using the tilting angle τ . The ray direction is determined similar to Eq. (3.2) to be

$$\vec{ray}^{**} = \begin{pmatrix} 1 \\ -\frac{pix_y - img_y/2}{img_y/2} \frac{\tan(\alpha_{cam})}{img_x/img_y} \end{pmatrix} \quad (3.5)$$

and normalized afterwards to receive \vec{ray}^* . The ray direction has to be tilted by multiplying the rotation matrix \mathbf{R} (Eq. (3.7)) with \vec{ray}^* to receive the final ray direction \vec{ray}

$$\vec{ray} = \mathbf{R} \cdot \frac{\vec{ray}^{**}}{|\vec{ray}^{**}|}, \quad (3.6)$$

3 Experimental details

$$\mathbf{R} = \begin{pmatrix} \cos(\tau) & -\sin(\tau) \\ \sin(\tau) & \cos(\tau) \end{pmatrix}. \quad (3.7)$$

The objective of the experiment in [63] is the measurement of the meniscus height in the observed edge. Due to the irregular shape of the sample bottom, some part of the sample makes contact with the liquid before the observed edge reaches the liquid surface. The capillary forces lead to wetting of the whole sample and the buildup of a meniscus after this first contact. The height of this meniscus has to be measured relative to the flat pool surface, for which the distance between the lowest point of the edge and the undisturbed liquid surface has to be known. The pixel coordinates of the lowest edge point and its reflection on the pool, before the wetting started, can be used to calculate their starting positions \vec{s}_c and \vec{s}_r and ray directions \vec{ray}_c and \vec{ray}_r . Using the ray direction pointing from the camera towards the reflection \vec{ray}_r , the ray direction mirrored by the horizontal liquid, connecting the reflection with the real corner, is known to be

$$\vec{ray}_m = \begin{pmatrix} ray_{r,y} \\ -ray_{r,z} \end{pmatrix}. \quad (3.8)$$

These vectors give an equation system with two equations and three parameters

$$\vec{s}_r + \vec{ray}_r l_r + \vec{ray}_m l_m = \vec{s}_c + \vec{ray}_c l_c, \quad (3.9)$$

with the three unknown ray lengths between the camera sensor and the reflection l_r , between the camera sensor and the corner l_c and between the reflection and the corner l_m as visible in Fig. 3.14.

To solve this equation system, two vertically aligned points on the sample surface (close to the edge) with a known distance Δh in between have

to be found, as sketched in Fig. 3.14. In the experiment, the sample was lowered a defined length (Δh) into the pool after the actual measurement, so that the positions of the same surface feature before and after lowering could be compared. These vertically aligned points have equal real-world y positions since they are on the vertical sample surface. This results in an equation system with two equations and two parameters:

$$\vec{s}_1 + \overrightarrow{ray}_1 l_1 - \vec{s}_2 + \overrightarrow{ray}_2 l_2 = \begin{pmatrix} 0 \\ \Delta h \end{pmatrix}. \quad (3.10)$$

With this equation system the ray lengths l_1 and l_2 can be calculated and since the previously described corner should be at approximately the same y position as the points 1 and 2, they can be used to calculate l_c

$$l_c = \frac{s_{1,y} + ray_{1,y} l_1 - s_{c,y}}{ray_{c,y}}. \quad (3.11)$$

The calculated value of l_c can be inserted into Eq. (3.9) to obtain the missing parameters l_r and l_m . With l_m the distance between the corner and the pool level can be calculated using

$$\Delta h_{cp} = ray_{m,z} l_m. \quad (3.12)$$

By setting the y position of the measured rivulet tip equal to the lowest point of the edge or one of the two points used in Eq. (3.10), its corresponding ray length l_{tip} can be calculated. The rivulet tip height above the pool, therefore, is

$$h_{tip} = s_{tip,z} + ray_{tip,z} l_{tip} - s_{c,z} + ray_{c,z} l_c + \Delta h_{cp}. \quad (3.13)$$

Tests with different values of α_{cam} have shown that the results are very insensitive to its value. With $\alpha_{cam} = 0.1^\circ$ the measured tenside solution rivulet height from [63] is (2.529 ± 0.026) mm (standard deviation) while with $\alpha_{cam} = 10^\circ$ it is (2.570 ± 0.026) mm. The distance and focus of the camera were very similar for different experiments and camera

3 Experimental details

opening angles above 4° were never observed in other measurements. An opening angle of 4° would result in a measured rivulet height of (2.545 ± 0.026) mm, limiting the maximum error made due to the unknown value of α_{cam} between 0.1° and 4° to be approx. 0.016 mm.

3.2.2 Image enhancement

The average camera resolution during the experiments was in the order of approx. $20 \mu\text{m}/\text{px}$. Rivulets, especially in long-term experiments like [90], become very thin and slow when rising much higher than the capillary length l_σ (Eq. (2.8)). The lighting in the experimental rig always had to be arranged in a way that glare points were visible at the rivulet tip. Due to the small size of the rivulet tips, this glare points were only in the order of single pixels on the camera images.

To avoid overexposure of the thin rivulet, the focus of the lighting reflection was set to the wider base of the rivulet, where its distinct refraction created a strong contrast even on mirroring walls. While local overexposure, completely hiding the rivulet tip, was avoided this way, the overall brightness and contrast (or signal-to-noise ratio) at the rivulet tip resulted to be low for very high rise heights. The signal-to-noise ratio was improved by summing up the brightness values of several successive camera images. Even with this signal boost, the rivulet tip glare point usually does not visually differ from the surrounding surface, because it partially follows the unevenness of the sample surface, leading to varying reflection and glare point intensities at different heights in addition to glare points on sample surface elevations themselves.

On darker areas the glare point of the rivulet tip represents an increase in brightness, while on reflecting background elevations the brightness often decreases due to the additional refraction. Since these brightness variations are in the order of the sample surface brightness, the rivulet tip glare point only becomes prominent in comparison with the dry sample surface. This comparison was done by subtracting an image (or a set of summed images) of a previous time in the experiment from the

currently analyzed image to get a dynamically adapting background subtraction. The time difference between these image pairs has to be adjusted manually and adapted during the video run time. When the time difference is too big, the reflections from the liquid on the sample, the position of the sample etc. are different, making an image subtraction impossible. When the time difference is too small, the rivulet tip, which decelerates over time, has not moved far enough to generate a distinct difference in brightness.

3.2.3 Rough surface post-processing

Different measurement techniques for rough sample surfaces were evaluated in the scope of this thesis and also tested during two supervised Bachelor theses [93, 94].

Shadow technique

For flat or rounded rough samples the classical shadow technique can be applied for macroscopic contact angle measurements [99]. This method was used during the course of the supervised Bachelor theses dealing with rough surfaces [93, 94] but not during the main research of this thesis. Since this technique is only applicable for flat or rounded uniform surfaces, it cannot be used on structured samples. More details about how the shadow technique was applied can be found in the Appendix A.3.

Bubble counting

An optical measurement technique for the detection of critical wetting speeds of rough surfaces was examined. This technique was named bubble counting and makes use of the behavior of very rough surfaces to pin air bubbles trapped during wetting. Since this technique was not used in the main thesis, its details are described in Appendix A.4.

Laser refraction

The shadow technique mentioned above is most suitable for rounded sample surfaces, at which the outermost surface point can be focused. However, on flat surfaces the visible shadow is an integral view along the whole sample face, adding blurriness due to the changing surface roughness and small differences in the liquid meniscus shape to the camera image. To measure contact angles at a defined position of a flat surface without receiving an integral value for the whole face, a laser refraction based measurement method was designed and evaluated. This method is described in Appendix A.5.

4 Rivulets and cusps

4.1 Basics of rivulets and cusps

Rivulets

The major part of research within this thesis deals with rivulets and cusps. Fig. 4.1 sketches a rivulet and a cusp. When a vertical edge has an opening angle γ which satisfies the so called Concus-Finn criterion [75] (Eq. (4.1)), the liquid meniscus at the edge experiences a negative capillary pressure pulling it up vertically along the edge.

$$\frac{\gamma}{2} + \theta < \frac{\pi}{2} \quad (4.1)$$

Even when the edge is completely filled with a liquid filament which, therefore, has a vertical surface, a liquid satisfying the Concus-Finn criterion will still be curved towards the edge, exerting a negative capillary pressure. This results in a theoretically unlimited rise of liquid along the edge. The gravitational force at each point of this rising liquid is cancelled out by the negative capillary pressure, increasing to infinity as the liquid surface approaches the edge with further height, decreasing the curvature radius (see Eq. (2.2)) towards zero. This quasi-unlimited vertical rise of liquid in an edge is called rivulet.

Fig. 4.2 shows two common approaches for modeling the shape of rivulets asymptotically reached after an infinite rise time. Modeling the edge as collection of vertical tubes like Ponomarenko et al. [13], as shown on the left of Fig. 4.2, results in the following asymptotic rivulet shape derived from the liquid rise height in vertical tubes:

4 Rivulets and cusps

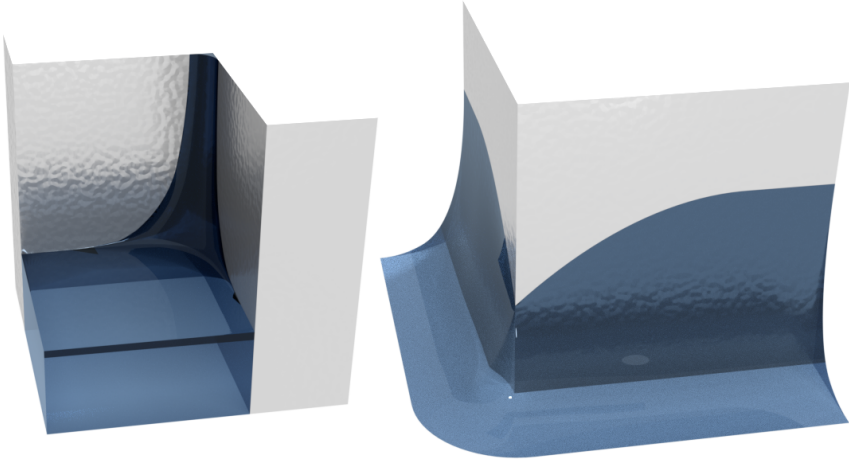


Figure 4.1: Left: An edge with an opening angle γ satisfying the Concus-Finn criterion (Eq. (4.1)) and thus forming a rivulet. Right: An edge with an opening angle above 180° forming a cusp. Images adapted from [64].

$$h = \frac{2\sigma \cos(\theta)}{\rho g r}, \quad (4.2)$$

with r being the radius of the virtual tubes at each position, which is equal to the orthogonal wall distance of the bisector

$$r = \sin\left(\frac{\gamma}{2}\right) m, \quad (4.3)$$

with m being the distance from the edge along the horizontal bisector of the edge. A similar description was gained by O'Brien et al. [11] and Bullard et al. [109] by also using the vertical curvature, but assuming the angle γ to be small enough to approximate the situation as quasi-2D meniscus between two parallel vertical walls with distance w :

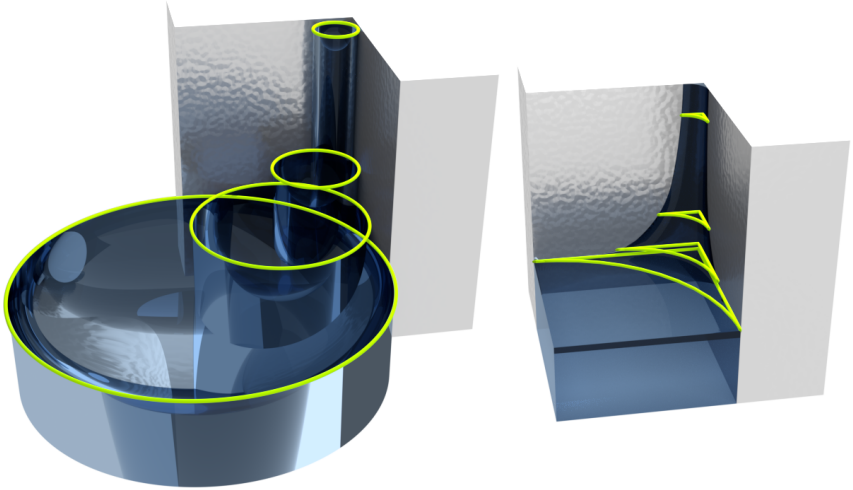


Figure 4.2: Left: The rivulet described as a collection of vertical tubes filling out the space between the adjacent walls. The vertical curvature on the top of tubes is the source of negative capillary pressure. Right: The rivulet described by horizontal slices determining the negative capillary pressure. Images adapted from [64].

$$h = \frac{2\sigma \cos(\theta)}{\rho g w}. \quad (4.4)$$

The distance w of the parallel walls in Eq. (4.4) depends on the distance to the edge and becomes zero directly at the edge. At the limit of γ becoming very small it becomes obvious that

$$w = 2r. \quad (4.5)$$

As for the classical capillary rise in tubes [110, 111], Eqs. (4.2) and (4.4) assume the liquid meniscus to exert a negative capillary pressure on the

4 Rivulets and cusps

liquid column, while at the same time ignoring its effect on the hydrostatic pressure. The shape of the meniscus becomes non-spherical/circular when its width reaches the order of the capillary length l_σ (Eq. (2.8)). The curvature of this non-spherical meniscus cannot be calculated analytically anymore and numerical simulations become necessary for a proper description of menisci in and above the order of the capillary length. Bullard et al. [109] performed such calculations to formulate an empirical correction relating the height values obtained from Eq. (4.4) with the real height at the bottom of the meniscus. Their modified height equation is

$$h = \left(\frac{2 \cos(\theta)}{\sigma_B} - f_B(\theta) g_B(\sigma_B) e^{-4.48 \sigma_B^{1/8}} \right) w, \quad (4.6)$$

$$\sigma_B = \frac{\rho g w^2}{\sigma}, \quad (4.7)$$

$$f_B(\theta) = 9.24 \cos(\theta) + 2.13 \cos(\theta)^3, \quad (4.8)$$

$$g_B(\sigma_B) = 0.834 \sqrt{\sigma_B} - 0.024 \sigma_B. \quad (4.9)$$

The right side of Fig. 4.2 shows a different assumption in which neither virtual tubes nor quasi-parallel walls are assumed. Instead the rivulet is described using horizontal slices with the horizontal curvature specifying the negative capillary pressure. This description results in the rivulet shape being

$$h = \frac{\sigma \cos\left(\theta + \frac{\gamma}{2}\right)}{\sin\left(\frac{\gamma}{2}\right) \rho g x}, \quad (4.10)$$

with x being the distance from the edge along the wall

$$x = \cos\left(\frac{\gamma}{2}\right) m. \quad (4.11)$$

Many studies observed the rising behavior of rivulets, identifying different regimes throughout the spontaneous rise. At the beginning the rivulet rise occurs very fast, but decelerates over a short period of time. Usually the initial rise is assumed to follow the Washburn law [10] with the

only competing forces being the negative capillary pressure and the viscous drag, leading to a $h \sim t^{1/2}$ relation between rise height h and time t [13, 85, 87]. However the Washburn regime cannot be observed experimentally. When plotted in a double logarithmic chart, no straight but a continuously curved line can be observed for the initial phase of rivulet rise. Due to the high acceleration of the previously calm liquid pool into the rivulet and the equally rapid deceleration after the initial rise, inertial forces can be suspected to become relevant in this early regime, regardless of the small size of the rivulet. This is also assumed by Schoelkopf et al. [112] for the imbibition of liquid into the structure of paper, who proposed a modified Washburn law, taking into account inertia, to better describe experimental results.

After this initial rise, usually a distinct power law of $h \sim t^{1/3}$ can be observed, resulting from the interaction of capillary, viscous and gravitational forces [13, 68, 74, 83, 87]. While some authors assume this power law to be the asymptotic limit for long rise times or heights [13], other authors observed a change in the rising behavior beyond the $1/3$ power law [85]. This further change in the rising behavior was also observed in this thesis and subsection 4.3.2 deals with the physical description and mathematical modeling of this additional rising behavior.

The effect of forced wetting on the rising behavior of rivulets was only sparsely researched in the past and hence this thesis analyzed forced rivulet rising. The respective results are presented in subsection 4.3.3.

Cusps

A cusp, as shown on the right of Fig. 4.1, is a depression of the liquid surface formed when a vertical edge in a liquid has an opening angle above 180° . In opposite to rivulets, cusps seem to have a limited depth and in the experiments performed in the course of this thesis, cusps could never be observed depressing the liquid meniscus below the unaffected liquid pool height. In vicinity to a rivulet, the depressing effect of cusps is partly canceled out, which is further described in subsection 4.2.

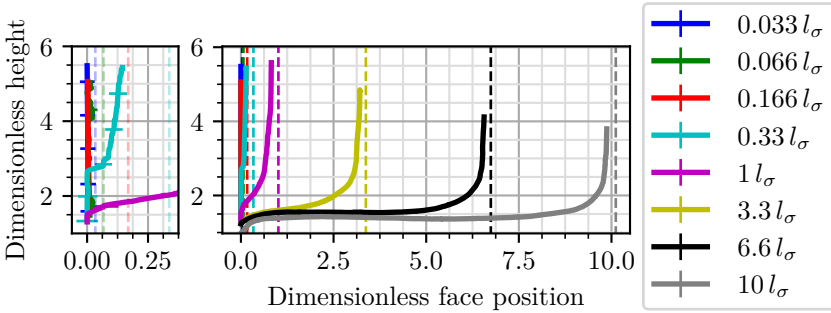


Figure 4.3: The contact line on the center face of samples as shown in Fig. 3.5. The plots are aligned at the outer edge with the cusp and the dashed lines illustrate the corresponding inner edge position for each sample. Height and face position are divided by the capillary length l_σ . The contact line shape was recorded after reaching an asymptotic static position. Data published in [64].

4.2 Static shape of rivulets and cusps

In [64] and [63] the static (or steady-state) shape of rivulets was analyzed. [64] deals with the interaction between rivulets and cusps which results are further described in subsection 4.2.1. The theoretical static rivulet shape models developed in [64] and [63] are presented in subsection 4.2.2.

4.2.1 Interaction of rivulets and cusps

The contact line contour measured on the center face between both edges of samples as sketched in Fig. 3.5 is shown in Fig. 4.3. The samples were made of aluminum and wetted with 20 cSt silicone oil (see

subsection 3.1.1). The samples were used upside down in comparison to Fig. 3.5, which is the same as horizontally mirroring the geometry. All graphs are aligned at the cusp (outer edge), which is defined as zero on the abscissa. The inner edge (rivulet center) of the different samples is indicated with vertical dashed lines. Every measurement was repeated five times and the standard deviation among these repetitions is shown with error bars which are hidden behind the plotted lines, except inside the inset on the left. The height and the position along the face are normalized with the capillary length l_σ . To highlight the phenomena at the cusp, the detail plot at the left with a stretched abscissa shows the contact line contour at the five smallest step sizes in more detail.

Fig. 4.3 shows that the rivulet and the cusp at the largest step size (approx. $10l_\sigma$) seem unaffected from each other, although a slight S-shape appears in the contact line contour in-between. The amplitude of this S-shape is of the order of the standard deviation and hence it can be caused by measurement errors. All smaller step sizes cause clear interaction between rivulet and cusp, resulting in a distinct S-shape in between, instead of a horizontal meniscus section, connecting cusp and rivulet.

Fig. 4.4 shows the cusp depth below the unaffected meniscus height for the different step sizes. It can be seen, that the cusp depth decreases with decreasing step size, becoming zero when the step vanishes. A similar result, with vanishing cusps for small step sizes, was obtained numerically for open grooves by Thammanna Gurumurthy et al. [89]. For comparison, Surface Evolver (SE), a software tool for calculating static interface shapes by minimizing their free energies [113], was employed to calculate the cusp depth for a step size of 50 mm (approx. $33.78l_\sigma$) [64]. The contact angle was varied between 0° and 20° to reflect the uncertainty of the contact angle, which was too small to be measured experimentally. The step size of 50 mm was used to avoid any boundary effects at the cusp. The liquid pool was simulated up to a distance of 30 mm from the walls with a minimal mesh size of $100\mu\text{m}$ directly at the edge. The simulation was stopped when seven consecutive iterations

4 Rivulets and cusps

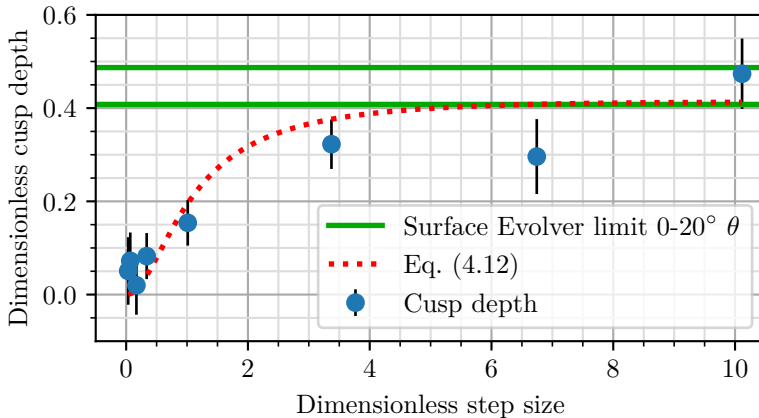


Figure 4.4: The depth of the cusp below the unaffected meniscus height for different step sizes of the samples from Fig. 3.5. The green lines show the cusp depth for an infinite step size calculated with Surface Evolver for contact angles of 0° and 20° . The dotted red line shows the depth of the cusp calculated with Eq. (4.12) using the lower numerical depth as c_{\max} . The cusp depths and step sizes are normalized with the capillary length l_σ . Data published in [64].

had a coefficient of variation below 10×10^{-7} . The results of the Surface Evolver simulations are plotted as horizontal green lines in Fig. 4.4 and verify the existence of an asymptotic maximum cusp depth and the fact that the step size of $10 l_\sigma$ is large enough to yield this maximum depth.

An empirical model was formulated to predict the cusp depth depending on the step size. For this model it is assumed that the cusp is pulled upwards proportional to the contact line slope, which is increased in vicinity to a rivulet. Since the slope of the contact line is also changed by the cusp, the contact line slope at the corresponding cusp position of a single rivulet without a cusp, calculated with Eq. (4.14) introduced later,

is used and inserted into

$$c = \frac{c_{\max}}{1 - \left(\frac{\partial h}{\partial x}\right)} \quad (4.12)$$

in which c_{\max} is the asymptotic maximum cusp depth. Eq. (4.12) is plotted as red dotted line in Fig. 4.4 using the 20° value from Surface Evolver for c_{\max} . This model fits the measured cusp depths qualitatively well. The second step sizes from the right and from the left both show some deviation from this model and the general trend of measured cusp depths. No physical reason exists for these step sizes to show a different behavior than the next similar step sizes; hence, it is assumed that inaccuracies in the target calibration (compare subsection 3.2.1) led to these discrepancies.

When the step size is approximately one capillary length or smaller, a new phenomenon can be observed, which is visible in the detail plot of Fig. 4.3. In contrast to larger step sizes, the contact line contour at such small step geometries does not exhibit a S-shape continuously approaching the deepest point of the cusp. Instead, the curvature from the rivulet continuous to the outer edge, at which the contact line pins and follows this edge vertically down to the bottom of the cusp. For a step size of approximately one capillary length this behavior could not be observed for all measurements, but for step sizes of $0.33 l_\sigma$ and below this, pinning with a vertical contact line becomes clearly evident. As visible in Fig. 4.4 the cusp still generates a small depression for step sizes below one capillary length. This results in a visible cusp at the outer wall of the edge (not plotted) which is connected to the pinned vertical part of the contact line. For step sizes below $0.33 l_\sigma$ the vertical pinning at the outer edge extends over the entire field of view. The contact lines of these small samples show a small amount of scatter (visible in the plots of [64]), which is caused by the limited camera resolution paired with imperfections of the sample edge.

In Fig. 4.5 the same data as in Fig. 4.3, without the data from step sizes below $0.33 l_\sigma$ (with completely pinned vertical contact lines), is shown. In

4 Rivulets and cusps

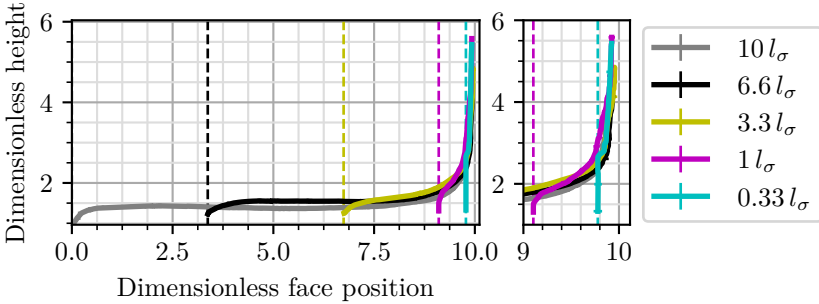


Figure 4.5: The contact line on the center face of samples as shown in Fig. 3.5. The plots are aligned at the inner edge with the rivulet and the dashed lines give the corresponding outer edge position for each sample. Only samples with step sizes above $0.166l_\sigma$ are shown. Height and face position are divided by the capillary length l_σ . Data published in [64].

this plot all graphs are aligned at the inner edge (right side of the graph) with the outer edge of the largest sample (approx. $10l_\sigma$) defining the zero position on the abscissa. As before for the inner edges, vertical dashed lines are used to illustrate the outer edges. In this plot it can be seen that all rivulets share the same contour regardless of the step size. This is especially remarkable for the smallest plotted step size of $0.33l_\sigma$, which shows the previously discussed distinct pinning at the outer edge. It leaves the outer edge at exactly the right height to match the shape of the other rivulets. This indicates that the rivulet shape is completely unaffected by a nearby cusp and very small step sizes only truncate the rivulet at the outer edge without changing its shape. In reverse, this behavior can be used to predict the pinning height at the outer edge of a known step size, when the shape of the rivulet is known.

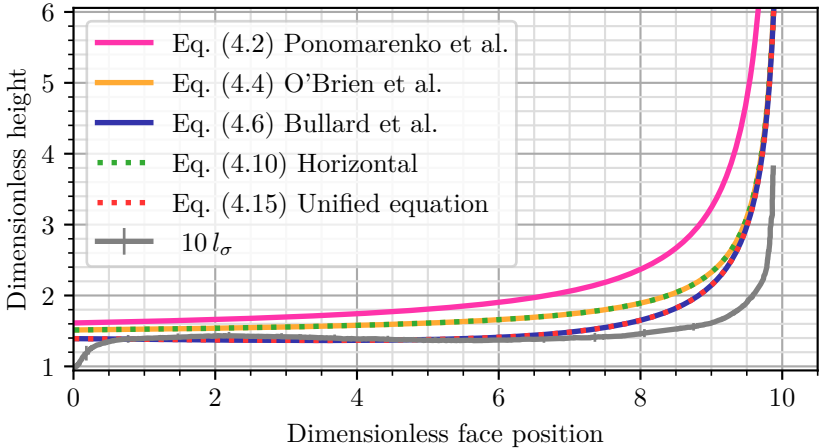


Figure 4.6: A comparison of the rivulet shapes predicted by Eqs. (4.2)-(4.15). For the chosen parameters some of the equations result in equal shapes, which is not the case for all parameter combinations. Data published in [64].

4.2.2 Shape of rivulets

Within the scope of this thesis two different models for the shape of a rivulet were derived. The first model is based on known models from the literature and links those by asymptotically blending from one to the other. The second model is based on the first model, but decoupled from literature models and derived with less restrictive assumptions, resulting in a physically more correct model.

Literature based model

Fig. 4.6 shows a comparison of the literature models Eqs. (4.2)-(4.10) with Eq. (4.15) which will be derived in this section and a measured contact line shape from Fig. 4.3. While the vertical curvature assumption

4 Rivulets and cusps

(Eqs. (4.2)-(4.6)) inevitable leads to an infinite rivulet height directly at the edge (curvature radius becoming zero) for every contact angle lower than 90° , Eq. (4.10), using the horizontal curvature assumption, obeys the Concus-Finn criterion given by Eq. (4.1).

In [64] an analytical description of the rivulet shape, merging Eqs. (4.2)-(4.10) into a single equation, was proposed to respect horizontal as well as vertical curvatures. This approach describes the rivulet shape more universally, though the resulting equation cannot be solved analytically anymore. For an asymptotic fit to Eqs. (4.2)-(4.10) some simplifying assumptions had to be made for the derivation of the unified equation. As for the equations given above, the meniscus is assumed to be circular and its influence on the hydrostatic pressure is neglected. What is more, the main curvature of the rivulet is modeled by assuming the rivulet to consist of 2D slices being orthogonal to its contact line direction with the opening angle of the tilted slices at the edge (blue in Fig. 4.7) being approximated to be equal to the slope angle α_x of the contact line along the wall. The slope angle α_x is defined as

$$\alpha_x = \arctan\left(-\frac{\partial h}{\partial x}\right), \quad (4.13)$$

with x being the distance to the edge along the wall, as shown in Fig. 4.7. To further simplify the description, only the rivulet shape of the samples used in this thesis, with $\gamma = \pi/2$, was derived in [64]. The resulting equation for the shape of the rivulet is

$$h = \frac{\sigma \sin\left(\frac{\pi}{2} - \theta - \frac{\alpha_x}{2}\right)}{\cos\left(\frac{\alpha_x}{2}\right) \rho g x} \quad (4.14)$$

which can be improved by implementing the empirical correction from Eq. (4.6) to get

$$h = \frac{\sigma \sin\left(\frac{\pi}{2} - \theta - \frac{\alpha_x}{2}\right)}{\cos\left(\frac{\alpha_x}{2}\right) \rho g x} - 2x \left(f_B(\theta) g_B(\sigma_B) e^{-4.48 \sigma_B^{1/8}} \right). \quad (4.15)$$

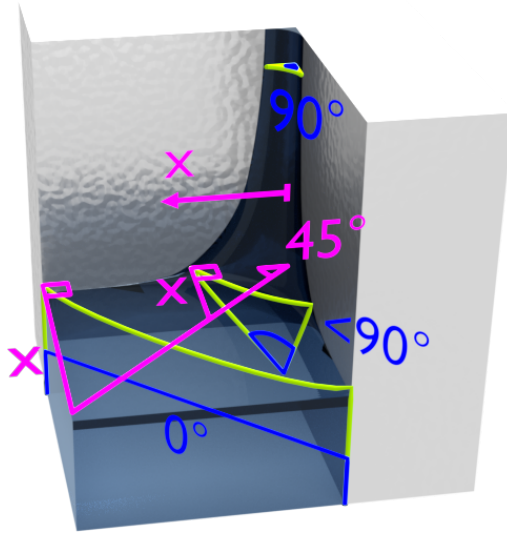


Figure 4.7: A sketch of three of the orthogonal planes used for the derivation of the unified rivulet shape equation Eq. (4.14). Image adapted from [64].

Due to the usage of the slices orthogonal to the contact line, shown in Fig. 4.7, the derivative α_x is incorporated into the equation, making Eqs. (4.14) and (4.15) non-linear differential equations, which have to be solved numerically on a 1D grid. For the numerical solution the Euler method [114] (or similar methods) can be used to plot the function from the initial flat pool level towards the rivulet or a gradient method like the Gauss-Newton algorithm [115] can be applied to solve the whole 1D grid in parallel.

A comparison of Eq. (4.14) with Eqs. (4.2)-(4.10) shows that for $\alpha_x \rightarrow 0$ (far away from the edge, where the vertical curvature is dominant) Eq. (4.14) becomes equal to Eq. (4.4) or Eq. (4.2) times 1/2, as well as the empirically corrected Eq. (4.15) equal to Eq. (4.6). Close to the edge

4 Rivulets and cusps

where $\alpha_x \rightarrow \pi/2$ (90°), the horizontal curvature becomes dominant and Eq. (4.14) becomes equal to Eq. (4.10). Due to this blending between the known literature models, depending on the dominant curvature direction, the rivulet is described more precisely than by applying one of the Eqs. (4.2)-(4.10). In Fig. 4.6, Eq. (4.15) is shown in comparison with the literature models.

Improved model

Based on the system of orthogonal slices used in the derivation of Eq. (4.14), a physically more correct description, not matching to known literature models anymore, was published in [63]. This advanced model is also not limited to right-angled edges but predicts rivulet shapes for arbitrary edge opening angles.

The hydrostatic pressure in Eq. (4.14) assumes the top of the liquid to be at height h . This simplification of assuming a horizontal liquid interface by neglecting the meniscus is common for all rivulet shape models mentioned so far. But since Eq. (4.14) is calculated along the wall position x (see Fig. 4.7), the height h in this equation corresponds to the contact line height at the wall, and with this assumes the complete liquid surface of each slice to be at the highest meniscus position. When the rivulet becomes vertical and the slices, therefore, become horizontal, the gravitational error vanishes due to the equal height of the whole slice. Further away from the edge where the slices are aligned vertically, the error due to h being the top of the meniscus is in the order of the meniscus height. Hence, the improved rivulet description published in [63] uses a coordinate system bisecting the edge (see Fig. 4.8) to improve the physical correctness by describing the height along the bottom of the meniscus, which is closer to the real hydrostatic pressure height than the contact line [109]. This improved model maintains the assumption of neglectable meniscus weights and a circular surface shape in one direction, while it describes the capillary pressure more precisely by calculating the two principal radii of curvature.

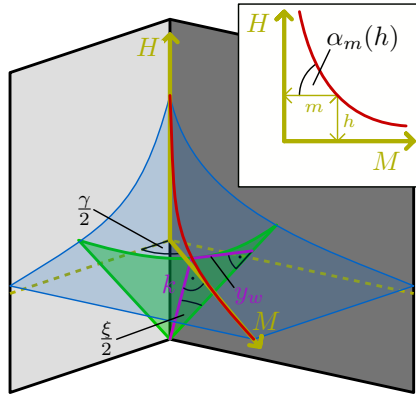


Figure 4.8: A sketch of the orthogonal planes used for the derivation of the improved rivulet shape equation, Eq. (4.25). A rivulet (blue) in an edge of opening angle γ is described by its liquid surface in the bisection plane (red) of the edge. The green slice is orthogonal to the liquid surface in the bisection plane with an orthogonal wall distance of y_w . The opening angle of the green slice is ξ and the in-slice distance between the liquid surface in the bisection plane and the edge is k . The inset on the top right shows the definition of α_m at a given position m along the M axis which bisects the edge horizontally. Image adapted from [63].

The coordinate system in the bisecting plane of the edge (see Fig. 4.8) leads to a new definition of the slope angle

$$\alpha_m(h) = \arctan \left(-\frac{\partial h}{\partial m} \right), \quad (4.16)$$

with m being the horizontal distance from the edge along the bisecting axis. For further calculations the geometry of the green slice in Fig. 4.8, orthogonal to the bisection of the rivulet, has to be determined. A

4 Rivulets and cusps

horizontal triangle between the bisecting axis and one of the two walls can be formed with the opposite leg being orthogonal to the bisecting axis. This triangle has an opening angle of $\gamma/2$ and the opposite leg has a length l of

$$l = \tan\left(\frac{\gamma}{2}\right) m. \quad (4.17)$$

The length k of the purple line in the green slice in Fig. 4.8, connecting the edge with the liquid surface in the bisection plane, can be determined by forming a vertical triangle in the bisection plane. This triangle is formed with one side being the purple line k and one side being the horizontal level (with length m by definition), the edge provides the opposite leg of the triangle. From this triangle and the slope from Eq. (4.16), which stays orthogonal to the direction of k , it follows to be

$$k(h) = \frac{m}{\sin(|\alpha_m(h)|)}. \quad (4.18)$$

From these two values the bisecting angle $\xi/2$ of the green slice can be calculated with an in-slice triangle to

$$\frac{\xi(h)}{2} = \arctan\left(\frac{l}{k(h)}\right) = \arctan\left(\tan\left(\frac{\gamma}{2}\right) \sin(|\alpha_m(h)|)\right). \quad (4.19)$$

With this angle all necessary values are known to calculate the length of the second purple in-slice line y_w . This line orthogonally connects the red surface bisection line to the wall, having a length of

$$y_w(h) = \tan\left(\frac{\gamma}{2}\right) \cos\left(\frac{\xi(h)}{2}\right) m. \quad (4.20)$$

With $\xi/2$ and y_w the two important quantities of the green slice from Fig. 4.8 are known. In contrast to Eq. (4.14), which only considers low contact angle liquids, the improved model also allows the calculation of high contact angle liquids. This leads to three geometrically different wetting setups, which again have to be considered for two inverse

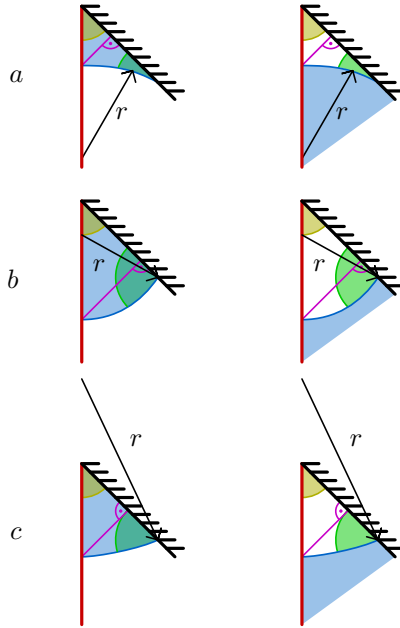


Figure 4.9: Three geometrically different wetting cases of which six wetting configurations with inverted air and liquid phases exist. The yellow angle is $\xi/2$, the green angle is θ^* and the purple line is the length y_w . Image adapted from [63].

liquid/air configurations, resulting in an overall amount of six different wetting cases, shown in Fig. 4.9.

Case *a* from Fig. 4.9 describes the classical case also considered in Eq. (4.14) with the circular arc of the liquid surface originating outside the edge and its radius pointing towards it. This case occurs when the slice contact angle θ^* (Eq. (4.24) given below) is below the slice related Concus-Finn criterion $(\pi/2 - \xi/2)$. For this case the radius r is given as

4 Rivulets and cusps

$$r_a(h) = -\frac{y_w(h)}{\sin\left(\frac{\xi(h)}{2}\right) - \cos(\theta^*(h))}. \quad (4.21)$$

When θ^* is larger than $\pi/2$, case *b* from Fig. 4.9 occurs. In this case the circular arc of the liquid surface is originating outside the edge with its radius pointing further away from the edge. This results in the radius r being

$$r_b(h) = -\frac{y_w(h)}{\cos(\theta^*(h)) \left(1 - \frac{\cos(\xi(h)/2)}{\sin(\theta^*(h))} + \frac{\cos(\xi(h)/2 + \theta^*(h))}{\sin(\theta^*(h)) \cos(\theta^*(h))}\right)}. \quad (4.22)$$

Wetting case *c* from Fig. 4.9 occurs when $\pi/2 - \xi/2 < \theta^* < \pi/2$. In this case r is

$$r_c(h) = \frac{y_w(h)}{\sin\left(\frac{\xi(h)}{2}\right) \left(\frac{1}{\cos(\theta^*(h))} - \frac{1}{\sin(\xi(h)/2)}\right)}. \quad (4.23)$$

Eqs. (4.21)-(4.23) describe the left column of Fig. 4.9 with liquid inside the edge surrounded by air. In the right column of Fig. 4.9 the situation is inverted and air inside the edge is surrounded by liquid. To deal with both situations at once, θ^* is defined to be

$$\theta^*(h) = \begin{cases} \theta & \text{for } \alpha_m(h) \geq 0 \\ \pi - \theta & \text{for } \alpha_m(h) < 0 \end{cases}, \quad (4.24)$$

with θ being the liquid contact angle.

Using these radii, the static pressure equation for the green slice from Fig. 4.8 follows to be

$$\rho gh = \begin{cases} \sigma \left(\frac{1}{r(h)} + \kappa(h)\right) & \text{for } \alpha_m(h) \geq 0 \\ \sigma \left(-\frac{1}{r(h)} + \kappa(h)\right) & \text{for } \alpha_m(h) < 0 \end{cases}, \quad (4.25)$$

4.2 Static shape of rivulets and cusps

with κ depicting the curvature along the bisection of the rivulet (red line in Fig. 4.8) and r being one of r_a , r_b and r_c (depending on $\xi/2$ and θ^*). Thus κ and $1/r$ describe the two principal radii of the surface. The left side of Eq. (4.25) describes the hydrostatic pressure at the height of the bisection point (along the red line in Fig. 4.8), while the right side describes the capillary pressure induced by the curvature inside and perpendicular to the green slice. The curvature along the bisection is defined as

$$\kappa(h) = \frac{\frac{\partial^2 h}{\partial m^2}}{\left(1 + \left(\frac{\partial h}{\partial m}\right)^2\right)^{3/2}}. \quad (4.26)$$

Eq. (4.16) to Eq. (4.26) can be inserted into Eq. (4.25) in order to calculate the height h at every position m . However, this non-linear equation system cannot be solved analytically and hence has to be solved numerically. For this, a fixed number of slices along the bisection axis m is taken into account and the corresponding heights h are calculated using the Gauss-Newton algorithm [115]. For the numerical solution of the rivulet shape, the piece-wise defined functions from Eqs. (4.21)-(4.23), Eq. (4.24) and Eq. (4.25) are disadvantageous. The calculation of numerical gradients close to the switching points between the alternative equations (e.g. $\alpha_m \approx 0$ in Eq. (4.25)) can give different results depending on if both function values for the gradient calculation are evaluated using the same or two different equations. Therefore, all derivatives necessary for the numerical solution are calculated analytically in order to ensure consistent values up to the switching points of the piece-wise defined functions.

The curvature perpendicular to the slices κ can be discretized along the M axis using central differences:

$$\kappa = \frac{h_{i+1} - 2h_i + h_{i-1}}{\left(\frac{m_{i+1} - m_{i-1}}{2}\right)^2 \left(1 + \left(\frac{h_{i+1} - h_{i-1}}{m_{i+1} - m_{i-1}}\right)^2\right)^{3/2}} \quad (4.27)$$

where h_i and m_i depict the height and edge distance of the current slice.

4 Rivulets and cusps

h_{i+1} and m_{i+1} depict the values of the next slice further away from the edge and h_{i-1} and m_{i-1} the values of the next slice towards the edge. The curvature can only be derived for $i > 0$ and $i < L - 1$ and is zero at both borders. Its derivatives are

$$\frac{\partial \kappa}{\partial h_{i+1}} = \frac{4(4h_{i-1}^2 - 2h_{i-1}(3h_i + h_{i+1}) + 6h_i h_{i+1} - 2h_{i+1}^2 + (m_{i+1} - m_{i-1})^2)}{(m_{i+1} - m_{i-1})^4 \left(1 + \left(\frac{h_{i+1} - h_{i-1}}{m_{i+1} - m_{i-1}}\right)^2\right)^{5/2}}, \quad (4.28)$$

$$\frac{\partial \kappa}{\partial h_i} = -\frac{8}{(m_{i+1} - m_{i-1})^2 \left(1 + \left(\frac{h_{i+1} - h_{i-1}}{m_{i+1} - m_{i-1}}\right)^2\right)^{3/2}} \quad (4.29)$$

and

$$\frac{\partial \kappa}{\partial h_{i-1}} = \frac{4((m_{i+1} - m_{i-1})^2 - 2(h_{i-1} - h_{i+1})(h_{i-1} - 3h_i + 2h_{i+1}))}{(m_{i+1} - m_{i-1})^4 \left(1 + \left(\frac{h_{i+1} - h_{i-1}}{m_{i+1} - m_{i-1}}\right)^2\right)^{5/2}}. \quad (4.30)$$

Numerical experiments have shown that for slice distances below $0.1 l_\sigma$ Eq. (4.27) leads to instability in the calculation due to the calculation of κ . While under-relaxation does not solve this problem, it was found that a transformation of the unit system remedies the instability. The transformation converts all lengths into multiples of the smallest distance between two slices, so that by definition all slices have a distance towards their neighbors of at least one. This transformation ensures convergent results for slice distances down to $0.01 l_\sigma$.

Since α_m (Eq. (4.16)) is defined along the discretized bisection axis, it also has to be discretized and becomes

$$\alpha_m = \begin{cases} \arctan\left(\frac{h_{i-1}-h_{i+1}}{m_{i+1}-m_{i-1}}\right) & \text{for } i > 0 \text{ and } i < L - 1 \\ \arctan\left(\frac{h_{i-1}-h_i}{m_i-m_{i-1}}\right) & \text{for } i = L - 1 \\ \arctan\left(\frac{h_i-h_{i+1}}{m_{i+1}-m_i}\right) & \text{for } i = 0 \end{cases} \quad (4.31)$$

with L being the number of slices and the first slice in vicinity to the edge being labeled as zero. The derivatives of α_m for $i > 0$ and $i < L - 1$ are

$$\frac{\partial\alpha_m}{\partial h_{i+1}} = \frac{m_{i-1} - m_{i+1}}{(h_{i-1}^2 - 2h_{i-1}h_{i+1} + m_{i-1}^2 - 2m_{i-1}m_{i+1} + h_{i+1}^2 + m_{i+1}^2)}, \quad (4.32)$$

$$\frac{\partial\alpha_m}{\partial h_{i-1}} = -\frac{\partial\alpha_m}{\partial h_{i+1}} \quad (4.33)$$

and

$$\frac{\partial\alpha_m}{\partial h_i} = 0. \quad (4.34)$$

At the closest slice towards the edge ($i = 0$) $\partial\alpha_m/\partial h_{i+1}$ is given by Eq. (4.32) when substituting h_{i-1} with h_i and m_{i-1} with m_i . With the same substitution Eq. (4.33) gives the equation for $\partial\alpha_m/\partial h_i$. The gradient $\partial\alpha_m/\partial h_{i-1}$ is zero since no slice closer to the edge exists.

For the last slice ($i = L - 1$) $\partial\alpha_m/\partial h_{i+1}$ is zero because no slice further away from the edge exists. $\partial\alpha_m/\partial h_i$ is given by Eq. (4.32) and $\partial\alpha_m/\partial h_{i-1}$ by Eq. (4.33) when for both cases h_{i+1} and m_{i+1} are replaced with h_i and m_i .

4 Rivulets and cusps

The following derivatives depend on the derivatives of α_m but otherwise are not discretized numerically themselves. Hence the derivatives will be denoted $\partial/\partial h$ and the respective derivative of α_m ($\partial\alpha_m/\partial h_{i-1}$, $\partial\alpha_m/\partial h_i$ or $\partial\alpha_m/\partial h_{i+1}$) has to be inserted. The derivative of $\xi/2$ from Eq. (4.19) is

$$\frac{\partial\xi(h)/2}{\partial h} = \frac{\alpha_m(h) \tan\left(\frac{\gamma}{2}\right) \frac{\partial\alpha_m(h)}{\partial h} \cos(\alpha_m(h))}{|\alpha_m(h)| \left(\tan\left(\frac{\gamma}{2}\right)^2 \sin(|\alpha_m(h)|)^2 + 1 \right)} \quad (4.35)$$

and the derivative of the length y_w is

$$\frac{\partial y_w(h)}{\partial h} = -\tan\left(\frac{\gamma}{2}\right) \sin\left(\frac{\xi(h)}{2}\right) \frac{\partial\xi(h)/2}{\partial h} m. \quad (4.36)$$

The derivatives of the three slice radii from Eqs. (4.21)-(4.23) are

$$\frac{\partial r_a(h)}{\partial h} = \frac{y_w(h) \left(\frac{\partial\theta^*(h)}{\partial h} \sin(\theta^*(h)) + \frac{\partial\xi(h)/2}{\partial h} \cos(\xi(h)/2) \right)}{(\sin(\xi(h)/2) - \cos(\theta^*(h)))^2}, \quad (4.37)$$

$$\frac{\partial r_b(h)}{\partial h} = -\frac{y_w(h) \left(\frac{\partial\theta^*(h)}{\partial h} \sin(\theta^*(h)) + \frac{\partial\xi(h)/2}{\partial h} \cos(\xi(h)/2) \right)}{(\cos(\theta^*(h)) - \sin(\xi(h)/2))^2} \quad (4.38)$$

and

$$\frac{\partial r_c(h)}{\partial h} = -\frac{y_w(h) \left(\frac{\partial\theta^*(h)}{\partial h} \tan(\theta^*(h)) + \frac{\partial\xi(h)/2}{\partial h} \frac{1}{\tan(\xi(h)/2)} \right)}{\cos(\theta^*(h)) \sin(\xi(h)/2) \left(\frac{1}{\cos(\theta^*(h))} - \frac{1}{\sin(\xi(h)/2)} \right)^2}. \quad (4.39)$$

Eq. (4.25) is solved using the Gauss-Newton algorithm by minimizing the error

$$e(h)_i = \begin{cases} \rho g h_i - \sigma \left(\frac{1}{r(h)_i} + \kappa(h)_i \right) & \text{for } \alpha_m(h) \geq 0 \\ \rho g h_i - \sigma \left(-\frac{1}{r(h)_i} + \kappa(h)_i \right) & \text{for } \alpha_m(h) < 0 \end{cases} \quad (4.40)$$

for each slice. The derivative of Eq. (4.40) with respect to the same slice is

$$\frac{\partial e(h)_i}{\partial h_i} = \begin{cases} \rho g - \sigma \left(-\frac{\partial r(h)_i}{\partial h_i} \frac{1}{r(h)_i^2} + \frac{\partial \kappa(h)_i}{\partial h_i} \right) & \text{for } \alpha_m(h) \geq 0 \\ \rho g - \sigma \left(\frac{\partial r(h)_i}{\partial h_i} \frac{1}{r(h)_i^2} + \frac{\partial \kappa(h)_i}{\partial h_i} \right) & \text{for } \alpha_m(h) < 0 \end{cases} \quad (4.41)$$

and the derivative with respect to a neighboring slice at position j ($j = i - 1$ or $j = i + 1$) is

$$\frac{\partial e(h)_i}{\partial h_j} = \begin{cases} -\sigma \left(-\frac{\partial r(h)_i}{\partial h_j} \frac{1}{r(h)_i^2} + \frac{\partial \kappa(h)_i}{\partial h_j} \right) & \text{for } \alpha_m(h) \geq 0 \\ -\sigma \left(\frac{\partial r(h)_i}{\partial h_j} \frac{1}{r(h)_i^2} + \frac{\partial \kappa(h)_i}{\partial h_j} \right) & \text{for } \alpha_m(h) < 0 \end{cases}. \quad (4.42)$$

With these analytical derivatives known, the equation system can be solved with the Gauss-Newton algorithm [115] to obtain the result shown in red in Fig. 4.10 for the static rise height of a supersaturated tenside solution. The slice distance for this calculation was $0.01 l_\sigma$. The sample used for the comparison experiment is shown in Fig. 3.8. Due to the rounded edge of the sample the calculated rivulet height, which assumes a sharp edge, is higher than the real-world value. To estimate the rise height in the rounded edge, the rivulet height in a distance towards the sharp edge equal to the distance of the rounded edge from the sharp edge is taken and plotted as dashed green line. It can be seen that the plotted real measurement point has a large uncertainty in the contact angle with measurements reaching below the Concus-Finn criterion marked by a vertical dashed line. Hence, it is possible that the contact angle of the supersaturated tenside solution actually was below the Concus-Finn limit and higher measured contact angles and the observed finite rivulet rise were occurring due to pinning events. Due to this high uncertainty in the real measurement, a second numerical calculation

4 Rivulets and cusps

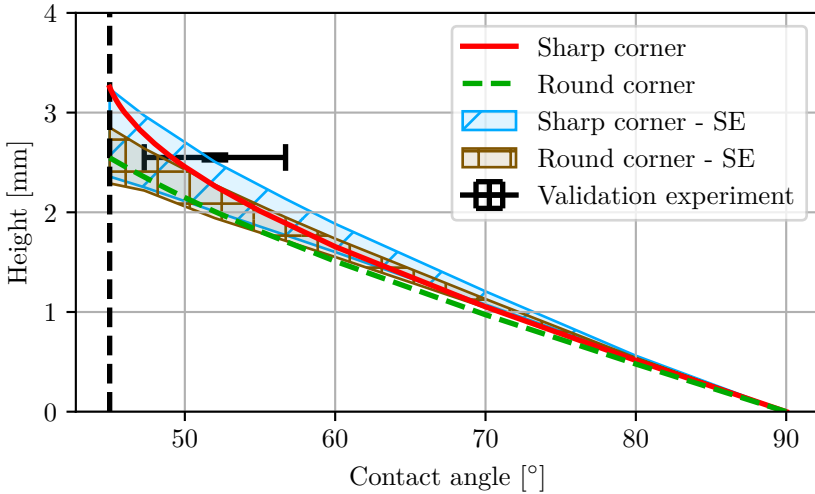


Figure 4.10: Calculated rivulet heights for a supersaturated tenside solution. The Concus-Finn criterion is shown as vertical dashed line. The red line shows the height directly in the edge and the green line shows the approximated height at the rounded sample. The shaded areas show the Surface Evolver results for convergence criteria from 1×10^{-7} to 1×10^{-9} . Data published in [63].

was done for comparison. This calculation was performed in Surface Evolver and proved to be highly dependent on the chosen convergence criteria. Therefore, simulations were performed with convergence criteria of 1×10^{-7} to 1×10^{-9} and the area between these results is marked in Fig. 4.10. It can be seen that the 3D Surface Evolver and the 1D model derived above provide similar results which both intersect the real measurement value. This emphasizes the correctness of the 1D model.

4.3 Rivulet dynamics

This section deals with the dynamics of rivulet motion. In subsection 4.3.1 the rise dynamics of rivulets in vicinity to cusps are analyzed. In subsection 4.3.2 the effect of a finite curvature in the edge on the rivulet rise dynamics is examined and subsection 4.3.3 deals with the forced wetting of edges forming rivulets.

4.3.1 Influence of cusps

In [64], which focused on the interaction of rivulets and cusps as presented in subsection 4.2.1, the rise dynamics of the rivulets were also measured. Fig. 4.11 shows the measured rivulet rise speed of 20 cSt silicone oil for different sample sizes.

The rise speed is expressed as Capillary number (Eq. (2.6)). The time in Fig. 4.11 is expressed in dimensionless time t_{dl} , defined as

$$t_{dl} = t \frac{\sqrt{\rho g \sigma}}{\mu}. \quad (4.43)$$

The rivulet rise was filmed with approx. 250 (249.986) frames per second and several post-processing steps were applied in order to smooth out the calculated speeds. At first the measured height data was interpolated with cubic splines and derivatives of these splines were evenly sampled over time to obtain speed data. A moving average with a window width of half of a second was then applied to the speed data to smooth it out further. Data closer to the beginning or the end of the measurement than half of the averaging window was discarded.

The resulting speed timeline in Fig. 4.11 shows some unexpected behavior. While in subsection 4.2.1 a truncation of the rivulet for step sizes below one capillary length l_σ could be observed, in Fig. 4.11 no change in the rivulet rise behavior around a capillary length of one could be seen. Instead, the rivulets for all step sizes show very similar behavior.

4 Rivulets and cusps

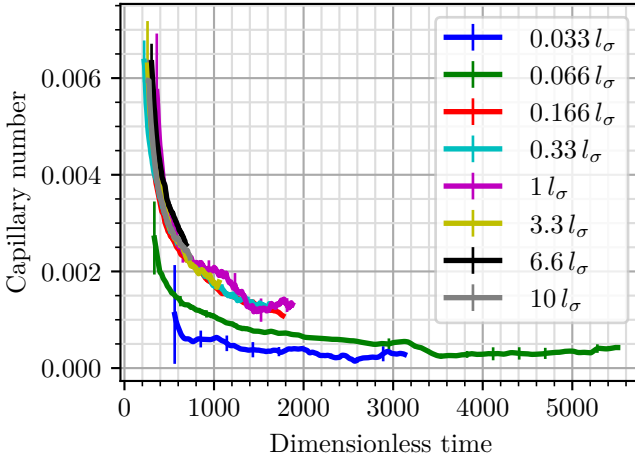


Figure 4.11: The Capillary number of the rivulets for different step sizes (compare to Fig. 3.5) plotted over dimensionless time (Eq. (4.43)). Data published in [64].

Only the rivulet rises with the two smallest step sizes of $0.066 l_\sigma$ and $0.033 l_\sigma$ significantly diverge from the other graphs. Since the capillary force is the only driving force of the rivulet rise, it becomes clear that even with a truncated rivulet shape, this driving force seems not to change. From this fact, it can be deduced that the bottom part of the rivulet, which becomes truncated for small step sizes, is not germane for the rivulet rise dynamics. This leads to the assumption that the region close to the rivulet tip itself provides the necessary driving force for the rivulet rise. One half of this relevant region width can be estimated to be below $0.166 l_\sigma$, since this step size still does not influence the rivulet rise.

The rivulet tip is too small to be observed in detail, so its size and shape are not known exactly. In the following models it is assumed to have a constant width over time and its dominant shape is assumed to be

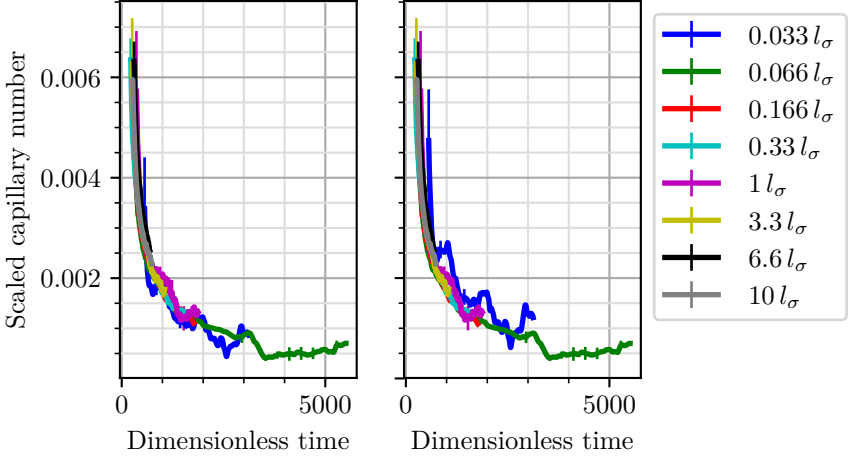


Figure 4.12: The dimensionless rivulet rise speed scaled by the factors given by Eq. (4.45). Left: $d = \text{const.}$ and $d = 0.2 l_\sigma$. Right: $2d = \text{const.}$ and $d = 0.1 l_\sigma$. Data published in [64].

describable by a horizontal arc, as shown on the right of Fig. 4.2. Two different models were built on these assumptions. One model assumes the rivulet tip width on the quasi-infinite wall to be constant (d) and unaffected by the length of the second wall (step size). The second model assumes the overall rivulet tip width ($2d$) to be constant, which leads to a shifting of the rivulet for step sizes below d , increasing rivulet tip width on the quasi-infinite wall. The resulting rivulet tip radii are

$$\begin{aligned}
 d = \text{const:} \quad r &= -\frac{d^2 + s^2}{2(\sin(\theta)d - \cos(\theta)s)} & \text{for } s \leq d \text{ and } \theta < 90^\circ, \\
 2d = \text{const:} \quad r &= -\frac{2d^2 - 2ds + s^2}{\sin(\theta)d - \cos(\theta)s} & \text{for } s \leq d \text{ and } \theta < 90^\circ,
 \end{aligned}
 \tag{4.44}$$

4 Rivulets and cusps

with s depicting the truncated rivulet length, which equals the step size. When the step size is larger than d , the rivulet is symmetric and $s = d$. To use Eq. (4.44) for the description of rivulet rise speeds, the radius has to be inverted to become a curvature κ_{tip} . The curvature ratio between a symmetric and a truncated rivulet can be used as a corrective scaling factor for rivulet speeds at small step sizes. This ratio is defined as

$$\begin{aligned}
 d = \text{const:} \quad & \frac{\kappa_{\text{unaffected}}}{\kappa_{\text{pinned}}} = \frac{(d^2 + s^2)(\sin(\theta) - \cos(\theta))}{2d(\sin(\theta)d - \cos(\theta)s)}, \\
 2d = \text{const:} \quad & \frac{\kappa_{\text{unaffected}}}{\kappa_{\text{pinned}}} = \frac{(2d^2 - 2ds + s^2)(\sin(\theta) - \cos(\theta))}{d(\sin(\theta)d - \cos(\theta)s)}, \quad (4.45) \\
 \text{both for} \quad & s \leq d \quad \text{and} \quad \theta < 90^\circ
 \end{aligned}$$

and leads to the two results shown in Fig. 4.12. While for the assumption of a fixed infinite wall width d the rivulet tip width ($d = 0.2l_\sigma$) would be larger than shown by the experiment ($d < 0.166l_\sigma$) to fit the results, the assumption of a fixed overall rivulet tip width $2d$ fits the measurement data due to $d = 0.1l_\sigma$ being below $0.166l_\sigma$. While this equation is empirical and uses several assumptions, it can scale all measured rivulet rises onto the same curve.

Additional rise speed measurements with silicone oil of 100 cSt viscosity were performed. They could be used to analyze the effect of the viscosity on the rivulet rise, since all other parameters in these measurements were identical. In the frame of [64] and this thesis this data was not post-processed and so the viscosity influence on rivulet rise is still an open topic that can be researched in the next funding period of the project.

4.3.2 Roundness effects

In [90], the effect of real-world edges onto the rivulet rise was analyzed. When an edge is not formed by two bodies (e.g. cylinders) pressed against each other, but is an integral part of an object, it is never perfectly sharp. This limited sharpness is the result of fabrication methods having

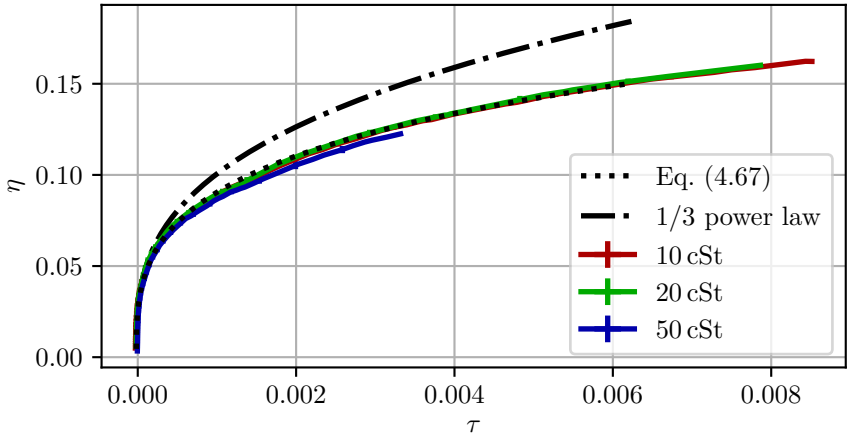


Figure 4.13: The measured rise heights over time in comparison to the $1/3$ power law and the theory from Eq. (4.67). Height and time are expressed in the dimensionless values described in Eq. (4.65) and Eq. (4.66). Data published in [90].

a limited precision and resolution, below which an undefined surface geometry is left. Due to the usually small size of these imperfections, they only become relevant for very thin and, therefore, very high rivulets. The PLA sample from Fig. 3.8 used in [63] is an exception since its edge radius is high enough to even influence rivulets at low heights.

For [90], the spontaneous rivulet rise in right-angled edges was tracked over long periods of time. It was found that the $h \sim t^{1/3}$ power law [13, 68] did not match the experimental results. After a very short initial phase with a power law exceeding $1/3$, the rivulet rise approached the $1/3$ power law, before moving on towards lower power values.

Fig. 4.13 shows the measured rivulet rise heights over time for three

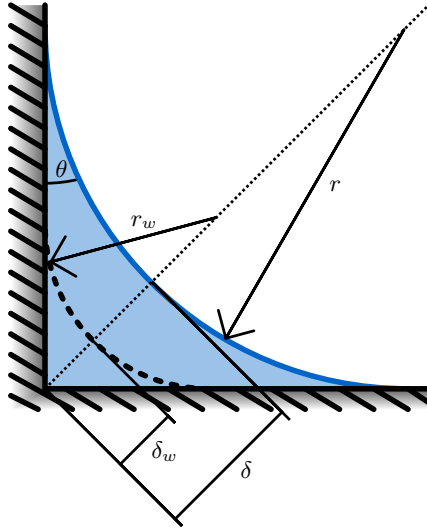


Figure 4.14: The geometry assumed for horizontal rivulet cross sections for the calculation of the rivulet rise in real-world edges.

different silicone oil viscosities on a milled steel sample having the geometry described in Fig. 3.5. In comparison, the corresponding 1/3 power law is plotted as a dash-dotted line. The plotted dimensionless height η and dimensionless time τ will be introduced in Eq. (4.65) and Eq. (4.66). Regardless of the applied dimensionless units, it can be seen, that the 1/3 power law overestimates the rivulet rise for later times.

The rivulet geometry is simplified by assuming the rivulet to be high enough to be describable by horizontal circular arcs, as shown on the right of Fig. 4.2. This allows the derivation of equations describing the effects of a real-world edge. According to Fig. 4.14, the rivulet curvature κ for right-angled edges is approximated as

$$\kappa = \frac{1}{r} \approx -\frac{A}{\delta} \quad (4.46)$$

with δ being the rivulet thickness and A being

$$A = \sqrt{2} \cos(\theta) - 1. \quad (4.47)$$

The resulting static rivulet shape from the force balance between capillary and hydrostatic pressure is

$$\rho gh = \frac{\sigma A}{\delta(h)}. \quad (4.48)$$

Eq. (4.48) respects the Concus-Finn criterion and results in an infinite rivulet rise height for contact angles below the Concus-Finn limit. Fig. 4.14 shows a horizontal cross section of the rivulet with radius r and an assumed edge radius r_w . It is obvious that even for a contact angle θ close to zero, $r \geq r_w$ for $\delta \geq \delta_w$. This geometrically limits the maximum rivulet rise height in a rounded edge to

$$h_{\max} = \frac{\sigma}{\rho g r_w} \quad (4.49)$$

for a contact angle θ of zero, when r becomes equal to r_w and the rivulet thickness on the rounding becomes zero ($\delta = \delta_w$). This description of h_{\max} is consistent with the results published in [69]. For contact angles higher than zero, the rivulet thickness δ becomes equal to δ_w before $r = r_w$, which reduces the maximum rise height to become

$$h_{\max} = \frac{\sigma}{\rho g r_w} \frac{\sqrt{2 \left(1 - \frac{\tan^2(\theta)}{\tan^2(\theta)+1} \right)} - 1}{\sqrt{2} - 1}. \quad (4.50)$$

Eq. (4.50) becomes equal to Eq. (4.49) for $\theta = 0^\circ$ and respects the Concus-Finn criterion by becoming zero for $\theta = 45^\circ$ (the Concus-Finn criterion for right-angled edges). A decrease of 5% in the maximum rivulet rise height h_{\max} (compared to $\theta = 0^\circ$) is obtained for a contact angle of 9.8° .

4 Rivulets and cusps

In [74], the long-wave equation for the evolution of the rivulet thickness $\delta(h, t)$ is obtained from the mass and axial momentum balance equations while accounting for the gravitational, viscous and capillary forces in the rivulet:

$$4g\rho\frac{\partial\delta}{\partial h}\delta^2 - 2B\mu\frac{\partial\delta}{\partial t} + A\sigma\left(\frac{\partial^2\delta}{\partial h^2}\delta + 2\left(\frac{\partial\delta}{\partial h}\right)^2\right) = 0, \quad (4.51)$$

where B is a dimensionless friction coefficient, solely determined by the shape of the rivulet cross section.

For large heights and times, δ approaches a similarity solution far from the liquid pool:

$$\delta(h, t) = LF(\Xi)t^{-\frac{1}{3}}, \quad (4.52)$$

$$\Xi = W - Ght^{-\frac{1}{3}}, \quad (4.53)$$

$$L = \left[\frac{AB\mu\sigma}{24\rho^2g^2}\right]^{\frac{1}{3}}, \quad (4.54)$$

$$G = \left[\frac{8B\rho g\mu}{3A^2\sigma^2}\right]^{\frac{1}{3}}. \quad (4.55)$$

$F(\Xi)$ in Eq. (4.52) is a dimensionless rivulet thickness using the similarity variable Ξ . W in Eq. (4.53) is a constant determined from the boundary conditions and L and G are coefficients used to simplify Eq. (4.52) and Eq. (4.53).

A value of $\Xi = 0$ corresponds to the height of a rivulet in a perfectly sharp edge

$$h = \frac{W}{G}t^{\frac{1}{3}}. \quad (4.56)$$

The function for the dimensionless rivulet thickness $F(\Xi)$ is a solution of the ordinary differential equation

$$-\frac{\partial F}{\partial \Xi} F^2 + \frac{\partial^2 F}{\partial \Xi^2} F + F + 2 \left(\frac{\partial F}{\partial \Xi} \right)^2 - W \frac{\partial F}{\partial \Xi} + \Xi \frac{\partial F}{\partial \Xi} = 0, \quad (4.57)$$

with the boundary conditions

$$F(0) = 0, \quad F(W) = \frac{4}{W - \Xi}, \quad (4.58)$$

because $\Xi = 0$ corresponds to the rivulet tip and $\Xi \rightarrow W$ corresponds to the meniscus, for large times approaching its static solution Eq. (4.48). A numerical solution of Eq. (4.57) obeying the boundary conditions from Eq. (4.58), gives, using the shooting method, a value of $W = 3.1623$.

Close to the rivulet tip $\Xi \ll 1$ and $F(\Xi) \ll 1$ hold true. An approximate solution for this region can be obtained by linearization to be

$$F(\Xi) = \frac{W}{2} \Xi \quad \text{with} \quad \Xi \rightarrow 0. \quad (4.59)$$

By using Eq. (4.52), the Eq. (4.59) can be written in dimensional form, resulting in

$$\delta \approx \frac{GLW o}{2} t^{-\frac{2}{3}} \quad \text{with} \quad o = h_{\text{sharp}} - h. \quad (4.60)$$

The variable o in Eq. (4.60) is the distance between the rivulet height at a rounded and a sharp edge. At the final rise height, δ should be equal to $\delta_w = Ar_w$ as visible in Fig. 4.14. In the vicinity to this final rise height, o becomes equal to o_w , which is

$$o_w = \frac{2Ar_w}{GLW} t^{\frac{2}{3}}. \quad (4.61)$$

In reality, the dimensionless friction coefficient B , which is included in G and L , is not a constant because it is determined, as mentioned above,

4 Rivulets and cusps

from the shape of the rivulet cross section. When the ratio δ_w/δ changes, the cross section and hence also B changes. This change is not accounted for in the current model and for $\delta_w/\delta \ll 1$, it is neglectable either way.

The position of the rivulet tip follows to be

$$h = h_{\text{sharp}} - o_w = \frac{Wt^{\frac{1}{3}}}{G} - \frac{2Ar_w t^{\frac{2}{3}}}{GLW}. \quad (4.62)$$

Eq. (4.62) can be expressed in dimensionless form by using the characteristic height

$$H = \frac{\sigma W^3}{8\rho g r_w} \quad (4.63)$$

and the characteristic time

$$T = \frac{B\mu\sigma W^6}{192A^2\rho^2 g^2 r_w^2}. \quad (4.64)$$

The resulting dimensionless values are

$$\eta = \frac{h}{H} \quad (4.65)$$

and

$$\tau = \frac{t}{T}. \quad (4.66)$$

These definitions allow the dimensionless height η to be written as

$$\eta = \tau^{\frac{1}{3}} - \tau^{\frac{2}{3}}, \quad (4.67)$$

which can be applied universally for any parameters. The effect of edge roundness on the rivulet rise can be described by o_w/h_{sharp} . From Eq. (4.67) this ratio follows to be $o_w/h_{\text{sharp}} = \tau^{1/3}$. When a value of

Oil type	r_w [m]	B
10 cSt	2.129×10^{-5}	74.09
20 cSt	2.199×10^{-5}	70.83
50 cSt	2.392×10^{-5}	80.01
All	2.294×10^{-5}	69.01

Table 4.1: Least square fitted values for r_w and B for the experiments shown in Fig. 4.13. Data published in [90].

$o_w/h_{\text{sharp}} = 0.1$ is defined as notable difference, this difference in rivulet rise becomes apparent at $\tau > 0.001$.

The values of r_w and B for the plots in Fig. 4.13 were obtained by least square fitting onto the experimental data. A clear difference between the 1/3 power law and the measured rivulet rises for three different silicone oil viscosities can be seen. At the same time all three viscosities and Eq. (4.67) fit together excellent.

Table 4.1 summarizes the values for r_w and B obtained by least square fitting of the different silicone oils used for the experiments in [90] which are plotted in Fig. 4.13. The last row shows the values obtained when fitting all experiments at once. In theory all silicone oils should result in the same values of r_w and B since they are geometrical parameters. It is visible that the values of r_w and B differ from liquid to liquid. These deviations can be caused by variations in the edge radius over height. All three liquids, reaching different heights in the given experimental time, thus integrate to different average edge radii. A second explanation can be small differences in the contact angle among the liquids. All three silicone oils exhibit very small contact angles, which could not be measured with the available equipment. Hence it is unknown if the contact angles are completely equal. Different contact angles would lead to slightly different rivulet shapes and hence a change in B .

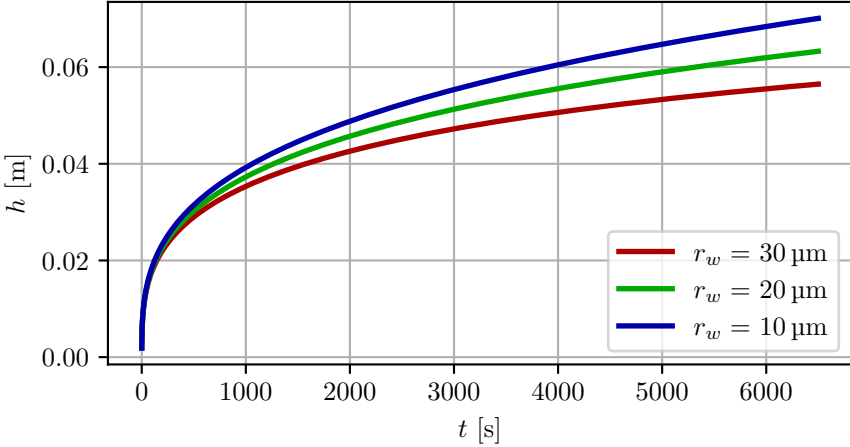


Figure 4.15: The rise height over time from Eq. (4.67). Plotted for different edge radii with otherwise constant parameters. Data published in [90].

The lines showing the rivulet rise of the three silicone oils in Fig. 4.13 are averaged from five repeated measurements each and the standard deviation between these measurements is indicated by vertical bars at selected values (visible at the 50 cSt line). The dotted line showing Eq. (4.67) is plotted using the values obtained when fitting all measurement data at once ($r_w = 2.294 \times 10^{-5}$ m and $B = 69.01$).

For Fig. 4.15, the parameters from the experiments shown in Fig. 4.13 were used and the edge radius was varied from $10 \mu\text{m}$ to $30 \mu\text{m}$. This plot shows the high sensitivity of measured r_w values to errors in the height measurement. After a physical time of 100 min an edge radius difference of $10 \mu\text{m}$ leads to a rivulet rise height change of only approx. 6.46 mm.

In the next step in [90], the sensitivity of the results to the measured contact angle of the liquid/solid combination was examined. It was found that, not directly obvious from the equations, r_w is independent of the assumed/measured contact angle. This means for a measurement of r_w by fitting of Eq. (4.67), the contact angle does not need to be known because r_w is equal for any assumed contact angle. The factor A is contact angle-dependent by its definition in Eq. (4.47) and B is also contact angle-dependent, due to it being dependent on the horizontal rivulet cross section. The scaling in time is determined by A and B in Eq. (4.64). When a physically incorrect contact angle θ is used for the calculation of A , the value of B , the only free parameter left for time scaling (because r_w couples time and height scaling and hence is not freely adjustable), adapts to a value ensuring $B/A^2 = \text{const.}$ This in turn leads to a scaling only depending on r_w anymore (Eqs. (4.63) and (4.64)).

In the study of Deng et al. [85] the rivulet rise of acetone and ethanol in V-grooves, milled into pure copper with a hard tool, are presented. While the V-grooves in this study were smaller than the capillary length, Fig. 4.11 demonstrates that this has no impact on the rivulet rise speed. In the study of Deng et al., a clear separation from the $1/3$ power law for long rise times was observed. The rise speed decreased until becoming zero at a certain time. In [90], Eq. (4.67) was fitted on the published measurement results of Deng et al. in order to explain their measured rise speed decrease with the roundness of the edges of their grooves. Table 4.2 shows the geometrical sizes of the different grooves analyzed by Deng et al. and the fitted values of r_w and B .

Deng et al. used two series of samples. One, labeled H, with a constant groove width and varying heights and one, labeled W, with a constant groove height and varying widths. Both series share a common sample (H5 respectively W2), which has the width from the H and the height from the W series. Fig. 4.16 shows τ - η diagrams of Eq. (4.67) fitted to the data of Deng et al. An excellent agreement of the measurement data with the rounded edge theory can be seen, while the deviation from the

Sample	Width [μm]	Depth [μm]	Edge angle	r_w [m]	B_{acetone}	B_{ethanol}
H1	450	500	42.5°	5.229×10^{-5}	5.937	8.480
H2	450	600	36.3°	4.571×10^{-5}	4.670	5.908
H3	450	650	33.9°	4.033×10^{-5}	3.246	4.215
H4	450	750	30.4°	3.644×10^{-5}	2.975	3.501
H5=W2	450	850	26.7°	3.507×10^{-5}	2.696	3.066
W1	400	850	24.1°	3.722×10^{-5}	2.973	3.814
W2=H5	450	850	26.7°	3.503×10^{-5}	2.647	3.019
W3	500	850	30.1°	3.659×10^{-5}	2.749	3.430
W4	600	850	34.5°	4.006×10^{-5}	3.450	4.761

Table 4.2: The geometrical sizes of the different samples used in [85] and the fitted values for Eq. (4.67) for this samples. H5 and W2 label the same physical sample. Data published in [90].

1/3 power law is very pronounced. Black crosses are used to mark the maximum of Eq. (4.67) at which the rivulet stops at the height h_{\max} given by Eq. (4.50). It can also be seen that this maximum rivulet height is in very good agreement to the experimental results.

The study of Deng et al. was performed using acetone and ethanol as wetting liquids. While the experiments' physical time was only in the range of 30 s, the maximum dimensionless time τ for these experiments is much higher than the dimensionless time reached during the more than 108 min silicone oil experiments from Fig. 4.13. The maximum rise heights of acetone and ethanol in the experiments of Deng et al. are different. This nonphysical offset was not explained in the publication but leads to the little deviation visible at approx. $\tau = 0.04$ in Fig. 4.16.

Due to a contact angle difference of about 5° between acetone and ethanol in the study of Deng et al., the cross section of both liquids' rivulets should be different. Hence, the shape-dependent friction factor B was fitted separately for both liquids. The measurement data of Deng et al. was manually extracted from the published plots. These plots are separated into one showing the H and one showing the W samples, which both show the same data for the common sample H5 or W2. In order to examine the quality of the manual data extraction, the data from H5 and W2 from both plots were taken separately and fitted to Eq. (4.67). As visible in Table 4.2, there are only minor differences in the values of r_w and B fitted for H5 and W2, indicating a good quality of the data extraction from both plots.

Fig. 4.17 shows the data for r_w and B from Table 4.2 plotted over the opening angle of the V-grooves. Except for the smallest opening angle of 24.1° r_w is proportional to the opening angle. When the same machining tool was used for all V-grooves by Deng et al. and milling happened in several passes to fabricate wider grooves, this proportionality is plausible. Deng et al. did not report the exact fabrication process of their V-grooves, so this theory cannot be confirmed. The increase in B with the opening angle can be explained by comparison with the

4 Rivulets and cusps

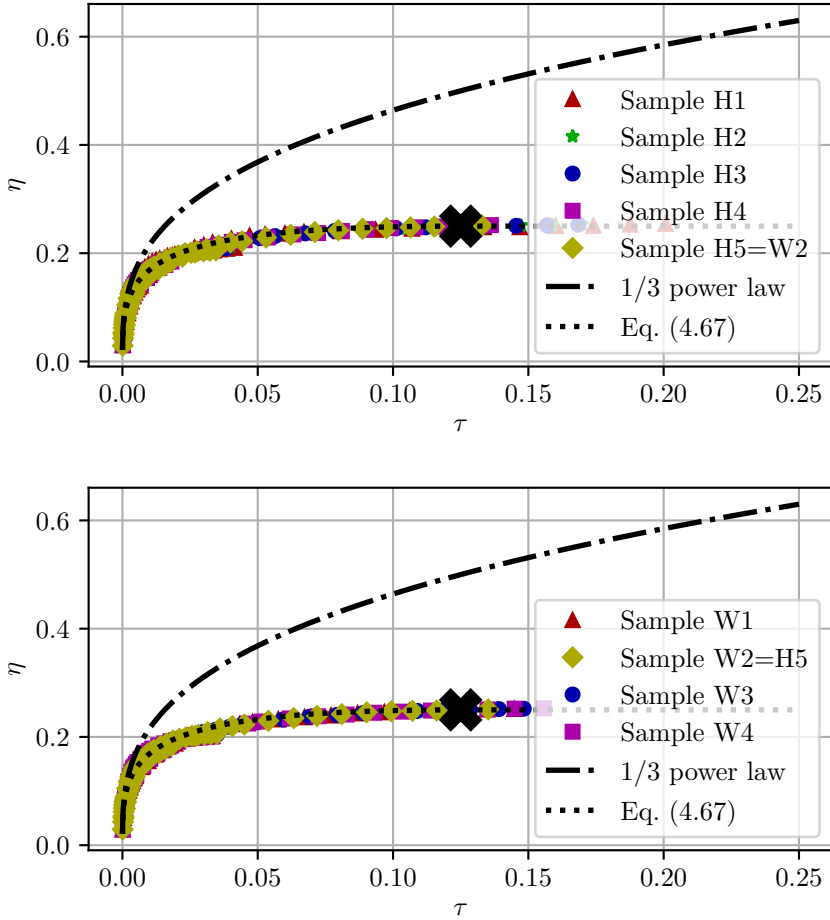


Figure 4.16: Eq. (4.67) fitted on the data of Deng et al. [85]. Top: The H sample series. Bottom: The W sample series. The 1/3 power law is shown in comparison. The black crosses mark the points at which the rivulets reach their final height h_{\max} (Eq. (4.50)). Data published in [90].

numerical work of Ayyaswamy et al. [65]. In this work, the flow profiles in triangular grooves were calculated and the dimensionless friction factors based on these profiles are given. The triangular grooves were aligned horizontally with gravity being perpendicular to them, while the V-grooves from Deng et al. were aligned vertically. Because of this difference, the data cannot be directly compared, but the trends of the dimensionless friction factor can be seen. Ayyaswamy et al. show a decreasing dimensionless friction factor for small contact angle liquids with increasing edge angles. This trend inverts towards increasing dimensionless friction factors with increasing edge angles for liquids with contact angles above approx. $10\text{-}20^\circ$. The values of B obtained for ethanol with $\theta = 19.8\text{-}21.8^\circ$ are higher than the values of B obtained for acetone with $\theta = 24.3\text{-}25.9^\circ$ [85]. This fits the results of Ayyaswamy et al. [65] and to physical expectations. The smaller contact angle of ethanol leads to a thinner rivulet (compare to Fig. 4.14), which has a higher velocity gradient than a thicker rivulet, increasing the viscous friction inside the rivulet. It also agrees to the results of Ayyaswamy et al., predicting that the difference in the dimensionless friction factor between these liquids is more pronounced for larger edge opening angles. The general shape of the rivulet can explain this effect. The rivulet at an edge with a small opening angle forms a thin wedge which overall shape is only slightly affected by the contact angle and hence the curvature of the short free surface between the adjacent walls. The influence of the curvature of the free surface on the overall shape increases with its length, becoming dominant for a thin rivulet film on an edge with a wide opening angle.

Another literature case compared to Eq. (4.67) is the data from Tani et al. [87]. In this study, silicone oil rivulets in micro-milled channels in hard PMMA (Poly(methyl methacrylate)) were tracked over more than 395 min. Fitting of Eq. (4.67) to this rise data failed for two of three samples used by Tani et al. The two samples for which the fitting failed were fitted to rivulet rise rates exceeding the $1/3$ power law, which itself is nonphysical and led to negative values of r_w . For the third sample, which did not exceed the $1/3$ power law, a plausible edge radius of $24.7\mu\text{m}$ was obtained. Two reasons are assumed for the other

4.3.3 Forced rivulet dynamics

In [63], a series of forced wetting experiments with 20 cSt silicone oil on a 100 mm sample with a step size of 15 mm, shown in Fig. 3.6, was performed. The sample was immersed into a silicone oil pool with speeds varying from 0.01 to 50 mm/s. Except for the lowest speed, a limitation in the rivulet rise could be observed, leading to a steady-state maximum rivulet rise height relative to the pool level. For higher speeds, the 100 mm sample proved to be too short for the wetting to become steady-state. This was mainly caused by waves introduced into the pool by the impacting sample, which directly affected the rivulet height in the edge and had no time to decay during the experimental run.

In Fig. 4.18 the steady-state rivulet height in multiples of the capillary length l_σ (Eq. (2.8)) is plotted over the Capillary number (Eq. (2.6)) of the immersion speed. The measurements which did not reach a steady-state rivulet height during the experiments are not shown. Just the slowest measurement, which did not reach a steady-state height inside the field of view, is still plotted. It shows the general trend of the steady-state rivulet height diverging towards infinity when the immersion speed approaches zero. The plotted height for this point represents the last height tracked by the camera before the rivulet left the camera image. The theoretical rise height of this point will be calculated later on.

The Reynolds number (Eq. (2.5)) of the fastest plotted measurement in Fig. 4.18 is only 1.85 when using the capillary length as characteristic length scale, which allows omitting inertial forces and the use of the Stokes equation [116]. In the Stokes equation, all forces, in this case, gravity, capillary and viscous forces, stay in balance at each instance of time. It can be assumed that the forces acting on a rivulet at height h^* , rising up an edge with speed u^* are equal to the forces acting on a rivulet staying at height h^* while the edge drives down with speed u^* . Fig. 4.19 shows this situation in the form of cross sections of two rivulets at the same height h^* . The liquid in a rivulet has a no-slip boundary

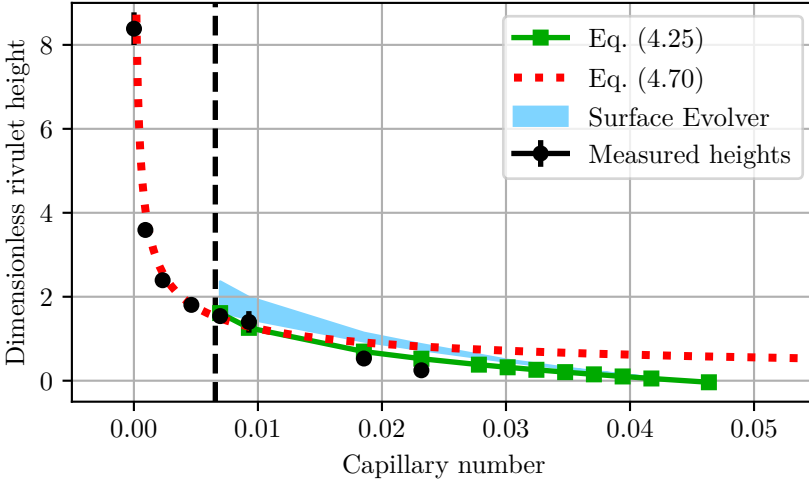


Figure 4.18: The measured steady-state rise heights for forced rivulet wetting in comparison to the 1D model from Eq. (4.25) and results from the Surface Evolver for convergence criteria from 1×10^{-7} to 1×10^{-9} . The dashed vertical line is the Concus-Finn criterion. Data published in [63].

condition at the adjacent walls of the edge and is driven by a pressure gradient equal to the vertical curvature gradient. This pressure gradient is balanced by the hydrostatic pressure, resulting in a 2D flow profile inside the rivulet, which cannot be obtained analytically. A cross section of this flow profile is sketched in the detail image on the left of Fig. 4.19. Assuming the rivulet shape to stay constant, the pressure gradient in the right case, with the moving edge, stays equal. Combined with the equal hydrostatic pressure, this leads to a similar flow profile superposed with a constant speed to meet the no-slip boundary condition (detail image on the right). With this superposition, the gradients in the flow profile and the viscous forces stay equal, leading to the Stokes equation being met.

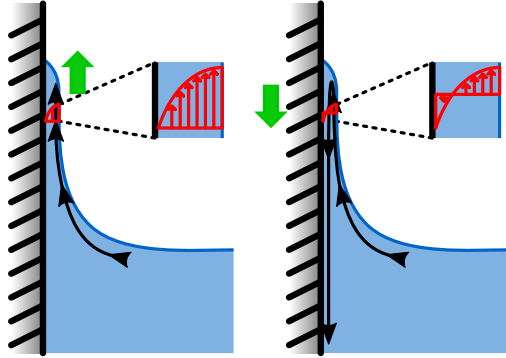


Figure 4.19: A cross section of a rivulet and the flow profile inside when rising up an edge (left) or staying constant at a moving edge (right). Image adapted from [63].

A condition which has to be obeyed in order to calculate a steady state rivulet height is the mass conservation. The liquid flow balance in each horizontal layer has to be zero to meet this condition. This requirement can only be checked by calculating the exact flow profile, which is, as mentioned beforehand, not possible analytically and has to be done numerically [65]. Instead, the possibility to superpose rivulet flow and edge movement can be used to superpose the observable rivulet tip rise with the edge descent. The 1/3 power law [13] can be used to describe the movement of the rivulet tip as

$$h = q \frac{\sigma^2 t^{\frac{1}{3}}}{\mu \rho g}, \quad (4.68)$$

in which q is a dimensionless fitting factor which can be determined with a spontaneously rising rivulet. While an improved and more complex power law was developed in the last section, the differences due to the roundness of the edge only become prominent at higher rivulet rise heights, which are not reached in the observed forced wetting situation. The speed of the rivulet tip at a certain height can be derivated from Eq. (4.68) to be

4 Rivulets and cusps

$$u = \frac{q^3}{3h^2} \frac{\sigma^2}{\mu\rho g}. \quad (4.69)$$

This speed can be superposed with the movement speed of the edge u^* , to receive a constant rivulet height, directly resulting in the steady-state height h^* for a rivulet in an edge moved with this speed.

$$h^* = \sqrt{\frac{q^3}{3u^*} \frac{\sigma^2}{\mu\rho g}}. \quad (4.70)$$

Eq. (4.70) is plotted as red dotted line in Fig. 4.18. A very good agreement of this equation with the measurement data for rising heights above approximately one capillary length can be seen, solidifying the assumption of a constant rivulet shape made for this derivation. What is more, Fig. 4.20 shows two rivulet halves from different experiments, one steady-state rivulet at a moving edge and one spontaneously rising rivulet. Even though the camera perspective and the shown rivulet heights have small variations, it is visible that the shape of the rivulets is very similar.

The deviation of this equation from the measurement data for smaller rivulet rise heights and higher speeds is an expected phenomenon since the $1/3$ power law, the Stokes equation and the purely 2D flow profile become invalid in this region. Eq. (4.70) can be used to calculate the theoretical rise height of the slowest forced movement (0.01 mm/s) in the very left of Fig. 4.18. The theoretical steady-state height of this point is at nearly $41 l_\sigma$, which is far higher than the last tracked position shown in the plot, but plausible due to the steady-state rise height asymptotically approaching infinity at zero movement speed.

While the simple model from Eq. (4.70) fails for steady-state rivulet heights below approximately one capillary length, the slope of such low rivulets could be assumed to be small enough to approximate them with horizontal contact lines moving upwards with a speed of u^* . While no dynamic contact angle model for non-orthogonal moving contact lines is known so far, with this approximation, the model of Kistler [47]

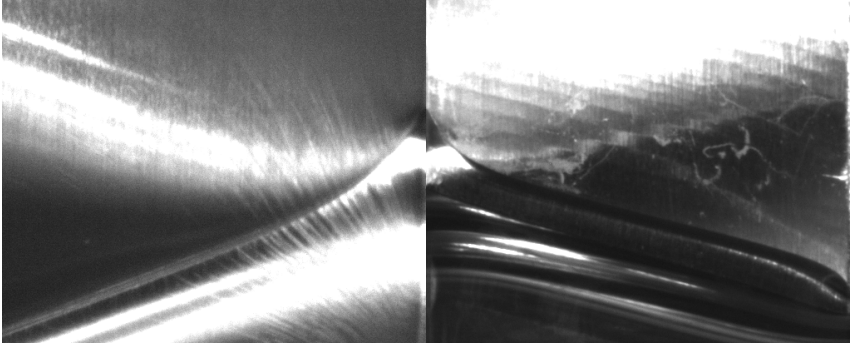


Figure 4.20: A comparison of a constant height rivulet on an edge moving down with 5 mm/s (left) and a spontaneously rising rivulet at approximately the same height (right, with a cusp at the right image border). The camera perspective is not exactly equal in both images.

(Eq. (2.12)) can be applied and inserted into the static rivulet model from Eq. (4.25). This allows the calculation of the approximated steady-state rivulet height for small height values at higher movement speeds. The results of Eq. (4.25) for a 1D mesh resolution of $0.01 l_\sigma$ are plotted in green in Fig. 4.18, using the same speed values as the experiment, also for the experimental points not shown because they did not reach a steady-state during the experimental run. The vertical black dashed line marks the Concus-Finn criterion below which Eq. (4.25) cannot be used because it results in an infinite rivulet height. It can be seen that Eq. (4.25) in combination with Eq. (2.12) approximates the given measurement points well and also nicely connects to Eq. (4.70) at the Concus-Finn limit. Additionally to Eq. (4.25), the Surface Evolver tool [113] was used in combination with the Kistler model (Eq. (2.12)) to verify the results of Eq. (4.25). The results of the Surface Evolver are shown as a blue shaded area for convergence criteria (surface energy coefficient of variation) from 1×10^{-7} to 1×10^{-9} . While the Surface Evolver connects good to Eq. (4.70) and Eq. (4.25) with a coarser convergence criterion, the calculated rivulet heights close to the Concus-Finn criterion

4 Rivulets and cusps

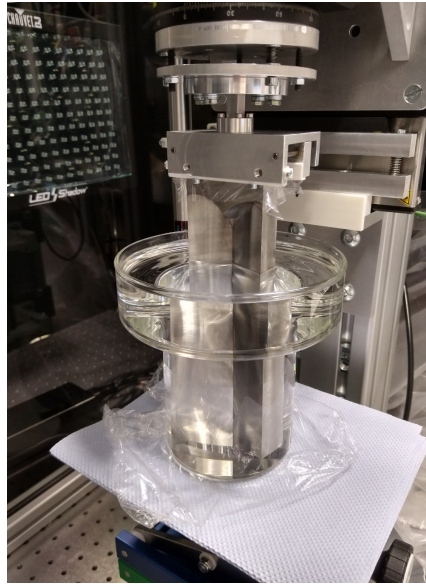


Figure 4.21: A stainless steel sample with an edge opening angle of 135° dipped into a pool of 20 cSt silicone oil. Safety precautions against silicone oil contamination are visible in the form of PE foil at the clamp and below the pool, with additional paper towels.

differ towards higher values for finer convergence criteria. This is the same behavior observed in Fig. 4.10. For the Surface Evolver calculation shown in Fig. 4.18, the walls at both sides of the edge were simulated up to a distance of 50 mm with the mesh in 3.5 mm distance of the edge having a maximum cell length of 0.2 mm. The mesh size was decreased and the domain size increased until the results of the Surface Evolver were independent of these values. The dependency from the convergence criterion could indeed not be removed [63].

Additional measurements on a sample with an edge opening angle of

135° were performed, which can be used to identify the influence of the edge opening angle onto forced rivulet wetting. Fig. 4.21 shows one of these measurements and also illustrates how all other measurements mentioned beforehand were performed. The safety precautions against contamination in form of PE foil between the sample and the clamp and below the liquid pool, which additionally is placed on some paper towels, are visible in Fig. 4.21. These safety precautions prevent the silicone oil from rising up to the clamp, contaminating it and from contaminating the rest of the test rig if some oil is spilled. These precautions are necessary because, as mentioned in subsection 3.1.1, silicone oil basically cannot be cleaned up in place. In the course of this thesis, the data from the measurements with the 135° sample was not post-processed. It is left to the second funding period of the project to analyze this data and compare it with the previously gained data for 90° edges.

4 *Rivulets and cusps*

5 Wetting of rough surfaces

In the real world, surfaces inevitable have some small scale geometrical features called roughness. The effect of such features in edges is already discussed in subsection 4.3.2. The effect of roughness on the wetting of flat walls was neglected in this thesis until now. In this chapter, the insights into wetting of rough walls gained in the course of this thesis are presented. Section 5.1 introduces the basic equations used to describe roughness. In section 5.2, the difficulties of fabricating samples with a specified roughness are highlighted. The chapter concludes with section 5.3, presenting information about the influence of roughness on wetting processes gained during this study.

5.1 Basics of roughness wetting

Wenzel [117] postulated a complete wetting of rough surfaces. Based on the Young equation (Eq. (2.1)) and using the balance of surface tensions/energies to describe the contact angle, his theory assumes the gain and loss in surface energy during wetting to be proportional to the wetted area; hence

$$\cos(\theta_{\text{rough}}) = r \cos(\theta), \quad (5.1)$$

with r being the ratio of the real rough solid surface to the apparent flat surface area,

$$r = \frac{A_{\text{real}}}{A_{\text{app}}}. \quad (5.2)$$

Cassie and Baxter [118] extended Wenzel's theory to be applicable for

5 Wetting of rough surfaces

porous materials by introducing an additional factor f , representing the fraction of apparent solid surface wetted with liquid. The inverse fraction $1 - f$ is the apparent area of porous segments in the solid, filled with air. With this fraction, the contact angle on a rough porous surface is described by

$$\cos(\theta_{\text{rough}}) = rf \cos(\theta) - (1 - f). \quad (5.3)$$

When the surface is not porous ($f = 1$), Eq. (5.3) reduces to Eq. (5.1). The definition of a porous surface used for the derivation of Eq. (5.3) includes any surface with trapped air pockets below the liquid. Hence, also very rough samples trapping air in their surface structures can be considered porous and Eq. (5.3) can be applied. When the roughness features become macroscopic, pinning due to the changing surface angle, as sketched in Fig. 2.4, appears and becomes the dominant factor for increased and unsteady contact angles.

5.2 Roughness fabrication

method	type	roughness	isotropic	reproducibility
polishing	subtractive	very small	yes	high
milling	subtractive	small	no	medium
sandblasting	subtractive	very high	yes	very low
SLS	additive	very high	mainly	very low
FFF	additive	medium to high	no	medium

Table 5.1: A qualitative comparison of the different fabrication methods tested for the production of specified rough samples.

In subsection 3.1.1, the fabrication methods applied for rough samples are

described. They can be divided into subtractive and additive methods. Table 5.1 shows a qualitative comparison of the roughness fabrication methods analyzed in the course of this thesis. In theory, all methods could be used for the production of metal samples to achieve equal, and hence comparable, solid/liquid pairings. However, the use of 3D printing (SLS and FFF) for metals is a new technique under active development [119] and commercially available printing machines are rare, expensive and difficult to handle (danger of metal fire, high power lasers etc.). Hence, for testing the applicability of these techniques, readily available plastic printing machines were used.

As observable in Table 5.1, polishing and milling have a medium to good reproducibility and lead to small or very small roughness values. Polishing leaves microscopic scratches on the surface. The use of a good polishing machine evens them out by constantly changing the polishing direction. In contrast, milling leaves visible, directed milling marks on the surface, which lead to non-isotropic wetting for non-perfectly wetting liquids. Sandblasting is not suitable to produce small roughness values without leaving parts of the surface untreated. Table A.3 shows some measurement results from Weidler [94]. It is visible, that the roughness parameters S_z (largest observed height difference), S_a (average absolute height) and S_q (average quadratic height) change by about one order of magnitude between sandblasting and milling, and between milling and polishing. The additional surface, formed in comparison to a perfectly flat surface, changes by two orders of magnitude from one fabrication method to the next.

While this change in roughness seems to be roughly equal among the different fabrication methods, a completely different wetting behavior was observed for the sandblasted samples compared to both other fabrication methods. Milled and polished samples allowed the immersion into a pool of glycerin-water mixture without air bubbles being trapped on their surface. Sandblasted samples inevitable captured air bubbles on their surface. Water had a contact angle clearly below 90° on milled and polished samples, but showed a hydrophobic contact angle on the

5 *Wetting of rough surfaces*

sandblasted samples. At the same time water droplets pinned strong enough on the sandblasted surfaces to stay in position, even when aligned vertically. It is assumed that this behavior could be attributed to two different factors. First of all, the influence of roughness on wetting is not expected to be linear, so that the roughness level of sandblasted samples could already trigger a very different regime than the roughness of the milled samples. At the same time polished samples could still show a comparable wetting behavior to milled ones. A second reason could be the shape of the roughness features, which should have a significant influence on wetting phenomena (pinning, trapped air pockets, rivulets and cusps), but can be only described in a very generic and averaged/integral manner using common roughness parameters, like the ones defined in EN ISO 25178.

Since no classical metal fabrication method resulting in roughness values between milling and sandblasting was found, the 3D printing methods SLS and FFF mentioned in subsection 3.1.1 were tested in order to fabricate samples with intermediate roughness values. SLS produces a roughness which is not perfectly isotropic but also not far from being isotropic. As Table 5.1 shows, the resulting roughness is very high and an appropriate comparison from everyday life would be a sand castle. Usually the outermost particles connected to the sample are only partially fused to the sample, while still retaining their particle shape. This results in a surface, which haptically feels like fine sand. For FFF the (vertical) surface consists of horizontal layers with approximately cylindrical outer borders (like the crust of a pizza), fused together on top of each other. The surface roughness of these cylindrical shapes is given by the inner surface of the printing nozzle. For a nozzle in good condition, which is not worn out, this roughness can be neglected compared to the cylindrical surface features. It is debatable whether the geometry produced in this process can be termed roughness, since many authors would call these surface features, exhibiting a regular pattern, a structure. The cylindrical layers themselves are taken as roughness elements, with the adjustable printing layer height defining the distance between them. The expected wetting effects due to the cylindrical barriers on the surface are mainly described by Fig. 2.4. For tilted samples rivulets and cusps can appear

on these surfaces.

5.3 Effects of roughness on wetting

Wetting and dewetting of rough surfaces is a topic of great interest for technical applications as well as in literature [2–8, 30, 33, 44, 91, 92, 117, 118, 120–130]. Despite the research on this topic, now going on for more than 70 years and despite the use of classical (Eq. (5.1) and Eq. (5.3)) and new approaches, like function-oriented surface definitions [128], no general relation between wetting behavior and roughness could be found until today. While fitted trends between different roughness parameters and wetting behavior are frequently reported, none of these trends is of a general nature and could be transferred to different solid/liquid systems or differently fabricated roughness without new experimental validation.

In the beginning of this thesis major problems emerged from the natural roughness of sample surfaces. While water is a well understood and easy to handle liquid, every real-world surface with roughness exceeding the level of polished surfaces causes significant amounts of pinning in combination with water. This pinning not only impedes contact angle measurements, but it can completely change the wetting behavior. Rivulets, being the main phenomenon analyzed in this thesis, are especially prone to pinning phenomena. Due to their small scale, inertial forces can be completely neglected. As visible in Fig. 4.11 and Fig. 4.18, the speed of rivulet rise decreases rapidly over height. This implies the driving force of the rivulet becoming increasingly smaller over height. When a rising rivulet is pinned at the edge, it has no inertia allowing it to directly break free and moreover, its driving force is too small to overcome the pinning. At this point the rivulet stays permanently pinned. This usually gives the optical impression of a contact angle above the Concus-Finn limit, leading to an increased meniscus rise in the edge, but not to a fully developed rivulet. When the pinning becomes strong enough, even flat wall menisci become pinned before reaching

5 *Wetting of rough surfaces*

their maximum height, leading to a disturbed shape of the contact line, pinned at arbitrary roughness elements.

Another aspect of roughness is the stochastic influence on wetting. When mono ethylene glycol is used as a liquid, instead of water, the pinning tendency reduces and a rivulet rise on aluminum samples can be observed. Nevertheless, this rivulet constantly pins and de-pins at various roughness features, leading to a jerking rise behavior, which varies from one experimental run to another. For some runs the rivulet becomes completely pinned at some height, while for other runs it continues to rise above this point. This strong stochastic influence prevents a closer inspection of the rivulet behavior and, thus, obscures the rivulet physics. Only liquids without visible pinning behavior can be used for wetting measurements, when it is not the goal to analyze the roughness effects themselves.

The Bachelor theses of Feldner [93] and Weidler [94] tested different force and optical measurement methods (subsection 3.2.3 for the optical post-processing) to analyze the interaction between wetting and roughness of samples as described in Table 5.1 (without FFF samples). They gained the same experience known from literature. While some trends between roughness and wetting behavior could be observed in their studies, no general model for the influence of roughness could be found. In the thesis of Weidler, the main focus was not on dynamic contact angles, but on the more general topic of wetting failure. This is an important topic for coating techniques in industry and hence a common research topic [2, 3, 50, 131–138]. Due to the high roughness of the sandblasted samples and the hydrophobicity of the SLS samples made out of PP, both sample types could not be wetted without air entrainment, reducing their critical wetting speed to zero. This is in contrast to results found in literature for smooth samples, assuming air to be entrained when the dynamic contact angle reaches 180° [50]. In both studies [93] and [94], different, novel measurement methods for dynamic contact angles and critical wetting speeds were tested, but the roughness led to high standard deviations in the data, making

none of these measurement methods look more promising than known measurement methods.

Another roughness study was performed in collaboration with Stephen Garoff from Carnegie Mellon University, using FFF samples (shown in Fig. 3.10) dipped or withdrawn from or into water and sunflower oil. A preliminary study was performed with varying printing layer heights or rather planned roughness levels. After improving the sample fabrication and measurement method, measurements with only one fixed roughness level were performed to reduce the number of parameters. In this study, the speed and the tilting angle of the samples were varied to analyze the wetting perpendicular to the surface features and along the grooves between these features. Water and sunflower oil were used because water shows a contact angle of about 90° on the PLA, while sunflower oil shows a very small contact angle, which could not be measured. This allows to analyze the change in wetting due to rivulets in the grooves. Sunflower oil was used instead of silicone oil, because it can be cleaned off the PLA samples with soap water and ethanol, while silicone oil could not be removed from the PLA samples without damaging them.

One effect that could be observed in preliminary measurements is a jumping motion of the contact line, which appears when immersing FFF samples into sunflower oil or pulling FFF samples out of water. When the printing layers are aligned horizontally, either some excess capillary pressure is built up by suppressing the pinned meniscus during immersion or the hydrostatic pressure difference increases when the pinned meniscus is pulled up with the sample. Both effects increase to a certain level, at which the contact line jumps to the next printing layer in order to reduce these excessive forces. This effect is still under investigation, i.e. whether this jump occurs at a fixed pressure difference limit and how this jumping behavior can be related to factors like sample movement speed.

When the FFF samples are tilted, the wetting and dewetting behavior changes. The contact line does not have to jump along the entire sample length at once, but can jump at the highest or lowest point of the current

5 *Wetting of rough surfaces*

printing layer and from this point slide down or up the sloped printing layer without experiencing large pinning effects in this direction.

6 Summary and outlook

In this thesis the basic wetting phenomena at single and adjacent edges were analyzed. In order for these analyses to be performed, a new experimental test rig was developed and built, which is presented in section 3.1. Furthermore, solid/liquid pairings insensitive to inevitable surface roughness were chosen to eliminate roughness effects during the measurements, as were found in several test series. The advantages and drawbacks of different materials are summarized in subsection 3.1.1. A fully three-dimensional calibration and post-processing of the camera images, allowing the camera to have full freedom in the position, rotation and its focal distance, was developed in order to enable the use of arbitrary sample and liquid pool materials and shapes. The main algorithms developed for this image processing are introduced in subsection 3.2.1.

This thesis focuses on basic phenomena and simple interactions to enable the future description of wetting of more complex systems on the foundation of this basic understanding. For the largest part of this research the sample geometry sketched in Fig. 3.5 was applied, which was especially designed to allow investigation of wetting at single edges and edges in close proximity to one other. Chapter 4 summarizes the physical insights gained from the studies performed with these samples. These insights are subdivided into static (4.2) and dynamic (4.3) wetting results.

For the static case, the interaction between concave and convex edges was investigated and it was found that a cusp undergoes a change in its shape when it is closer than one capillary length to a rivulet. However, the shape of the rivulet seems to be unaffected by a nearby cusp. More details about these results can be found in subsection 4.2.1. Furthermore,

6 Summary and outlook

two models for the shape of a rivulet were developed and presented in subsection 4.2.2. The first model is related to known literature models while the second model is based on the same modeling approach used for the first model, but derived with less assumptions, resulting in a more precise and universal description of rivulet shapes.

The dynamic wetting results are subdivided into three different topics. The first topic presented in subsection 4.3.1 deals with the change in rivulet rise speed due to a nearby cusp and empirically describes the effect of the cusp on the rivulet rise speed. The measurements show no change in rivulet rise speed in vicinity to a cusp, unless the distance between the cusp and the rivulet is less than a tenth of the capillary length. The second topic involves real-world edges with a limited sharpness, leading to a measurable change in rivulet rising behavior and a maximum rivulet rise height. The effects of this limited sharpness are modeled using newly defined dimensionless values describing the rise speed up to the geometrical limit above which the rivulet cannot rise. This behavior and its modeling are summarized in subsection 4.3.2. As a third topic, the influence of forced wetting on the rivulet propagation was reported in this thesis. It was found that the rivulet rise reaches different steady-state heights above the pool level, which depend on the sample immersion speed. An analytic model for the steady-state height of rivulets as well as an approximation for short rivulets, using the improved static rivulet shape model from subsection 4.2.2, are presented in subsection 4.3.3.

In the course of this thesis unintentional roughness complicated many measurements, which demanded a closer look at the interaction of wetting and roughness. Different fabrication methods for intended roughness as well as different measurement techniques for dynamic contact angles and critical wetting speeds on rough surfaces were examined in two supervised Bachelor theses [93] and [94]. None of the tested fabrication and measurement techniques proved to be feasible. Another study using specified rough samples fabricated with FFF was performed. Chapter 5 highlights the findings for the production of rough surfaces and their interaction with wetting phenomena.

While several new insights into the rivulet wetting of edges could be gained in this thesis, there are many pending issues left. Different measurements were performed which were not post-processed within the scope of this thesis and can be used for future analyses. Some of these measurements are similar to the experiments from [64], but use 100 cSt instead of 20 cSt silicone oil. These measurements could possibly provide new insight into the coupling of rivulet rise speed and viscosity in vicinity to cusps. Furthermore, a set of samples with different edge angles, shown in Fig. 3.7, was fabricated and forced wetting experiments were performed with 20 cSt silicone oil and the 135° sample of this set. This measurement data is not yet post-processed and measurements with different samples of this set are still missing, but they yield information on the relation between rivulet rise, cusp depth and the opening angle of the edge, which is a highly interesting research topic. A complete measurement series with FFF samples is, at the time of writing this thesis, still being post-processed. Preliminary measurements have shown interesting behavior, which could yield new insights into the wetting and dewetting of rough surfaces.

Several future measurements were prepared during this thesis. Fig. 3.3 shows a rotating module in the center image, which can be used to rotate cylindrical samples around their vertical axis while performing wetting or dewetting experiments with them. This module was used for preliminary tests during this thesis. After a refinement of the clamping system, this module can be very useful to reveal the dynamic contact angle of liquids wetting samples non-orthogonal to their contact line direction. This type of dynamic contact angle is a completely new topic, but necessary to describe the dynamic and forced wetting of complex surface geometries. With such a dynamic contact angle model, the improved static rivulet shape equation from subsection 4.2.2 could very precisely predict the steady-state rivulet height of forced wetted rivulets at all speeds. Another module for future measurements is shown in the right image of Fig. 3.3. This module for analyzing the gravure printing process was developed by a student group [58] and built after minor

6 *Summary and outlook*

improvements. Some preliminary tests with the force sensors of the module and optical tests with a gravure printing sample and the camera were performed. Future experiments with this gravure printing module could illuminate the process of wetting and dewetting at gravure printing plates on a level of a tenth of the capillary length giving more insight into the phenomena happening during gravure printing.

As mentioned above, this thesis deals with vertical, right-angled edges of different sharpness and the interaction of rivulets in these edges with cusps in vicinity or a forced immersion of the sample. Preparations were made to analyze non-orthogonal wetting and edges of different opening angles. The preliminary results and connections to e.g. forced rivulet wetting, seem to be very promising and so future work can focus on obtaining a more complete picture of rivulet wetting. Non-vertical edges were not analyzed, except for the FFF sample experiments, which do not solely focus on this phenomena. For a better understanding of the wetting of geometrically complex surfaces, the wetting of edges in different orientations towards gravity should be analyzed in future. This also includes tilted edges with an additional rotation around their own edge direction, so that both walls are inclined differently to the direction of gravity. With insight into this tilted rivulet phenomena and refinements of the general rivulet wetting models, it could be possible to abstract more complex surface features, e.g. spherical hills, into combinations of differently tilted, rounded edges with non-linear walls. This could allow to build a general model describing the wetting properties of arbitrary surface features by subdividing them into different edges.

A Appendix

A.1 Force measurement details

To enable the measurement of contact line forces on the samples a 31E-002N5-1m force sensor (from ALTHEN GmbH Meß- und Sensortechnik, Germany) [139] with a maximum force of 2.5 N was built into the test rig. Independent of the AD converting precision, the noise of the sensor exhibits a level of approx. 10 mN, which is higher than e.g. the force pure water ($\sigma = 72 \text{ mN/m}$) exerts on the default Wilhelmy plate used in the DCAT 25, which is only about 2.9 mN. On the other hand a sensor with lower maximum force and therefore higher precision cannot be used, since milled metal samples are relatively large and therefore heavy (see section 3.1.1). For example the samples milled from 1.4404 stainless steel, which were elongated to yield good measurement results, are several times too heavy for the sensor. These samples have weights in the order of 0.6 kg up to the heaviest sample, the 135° edge shown in Fig. 3.7 and 4.21, which has a weight of approx. 1.76 kg. This large difference between the contact line forces and the weight of the samples prevents the exact measurement of these forces.

A.2 Light field calibration details

Light field calibration is a calibration method which should, in theory, enhance the target calibration (see section 3.2.1). It automatically detects the relative positioning of the sample towards the two target positions. Light field calibration makes use of the parallax effect when the sample is moved in relation to a fixed camera position. Due to the perspective,

parts of the sample closer to the camera are seen moving faster than parts further away from the camera. When the real sample speed and the calibrated camera frustum are known, this observed speed difference can be translated into depth information. This depth information can either be filtered and directly used as sample surface in the ray tracing post-processing or a 3D model of the sample can be fitted onto the depth information to obtain its real rotation and position.

While this calibration method in theory should be superior to a pure target calibration, some difficulties prevented the use of it. The main obstacle is the small opening angle of the applied camera objective which leads to negligible perspective effects and hence negligible speed differences visible in the camera images. Moreover, the flat milled metal samples have few characteristic features for the algorithm to track. Due to their high reflectivity and the fixed lighting position, the lighting of the sample and its features constantly changes during sample movement, complicating the automatic tracking even more. These difficulties could not be overcome without other major drawbacks; therefore, light field calibration was never applied to published measurements.

A.3 Shadow technique details

When using the shadow technique, the observed sample surface is aligned parallel to the camera view direction, while the camera itself is orientated horizontally. A diffuse transparent screen is placed on the opposite side of the sample and illuminated from behind. With this setup a black shadow of the sample and the meniscus is visible in front of a white background. Due to the horizontal and perpendicular view at the meniscus and the sample, the macroscopic kink at the contact line can be detected and its visible angle can be measured by fitting and intersecting geometrical primitives (straight lines, circles etc.) or 2D liquid surface models on the visible borders of the sample and the liquid meniscus. Usually the border detection process can be achieved with simple image algorithms.

First the camera image is binarized followed by a border detection by searching pixels with neighbors in a different color. Afterwards separated border pixels (five or more neighboring pixels in a different color) can be dropped and a flood fill algorithm can be applied to detect the connected part of the border.

Within the scope of this thesis the flood fill algorithm was modified to detect only a border line of one pixel width, even if more pixels are previously marked as possible border pixels. The algorithm starts from the top of the image where the usually good contrast allows a clear border detection at the starting pixel \vec{pix}_i . A vertical initial border direction towards the bottom

$$\vec{b}_{\text{dir},i} = \begin{pmatrix} 0 \\ 1 \end{pmatrix} \quad (\text{A.1})$$

is assumed and the distances between all neighboring pixels, which are marked as possible border, and the pixel at $\vec{pix}_i + \vec{b}_{\text{dir},i}$ (in this case the pixel directly below the starting pixel) are compared. The pixel with the shortest distance, which is the pixel at $\vec{pix}_i + \vec{b}_{\text{dir},i}$ if it is marked as possible border pixel, is taken as next border point \vec{pix}_{i+1} . The border direction is updated to be

$$\vec{b}_{\text{dir},i+1} = \frac{\vec{b}_{\text{dir},i} + (\vec{pix}_{i+1} - \vec{pix}_i)}{2}. \quad (\text{A.2})$$

This smoothing of the preferred contact line direction is used to avoid wobble in low contrast areas with multiple possible border directions.

After the border is marked, the kink at the contact line has to be detected. In this thesis this was done by least square fitting two adjacent lines at the border. These lines are fitted on 10px long intersecting border segments to smooth out artificial noise from the binary defined border. This means e.g. the first line is fitted onto the

A Appendix

border pixels 0 to 9 and the second line is fitted onto the border pixels 9 to 18. Afterwards the angle between the lines is calculated and saved (for pixel position 9 in this example) before the lines are moved one pixel further along the border (the first line fitted from 1-10 and the second line from 10-19 in the example) and the intersecting angle is calculated again. This process is repeated for the whole line and the pixel with the highest intersection angle is marked as contact line position.

Usually the visible sample surface is macroscopically flat and hence a straight line is the most suitable fit on the border above the contact line. However, the liquid surface is curved and the choice of the fitted geometry directly influences the resulting contact angle. For fitting a 2D liquid surface model, the whole meniscus down to the flat pool level has to be visible and a static wetting situation, ignoring liquid flow, Marangoni flows etc. has to be assumed. Less modeling and assumptions are involved in geometric models for which ellipsoids, circles and straight lines were examined in this thesis. For ellipsoids the fitting offered different results, depending on the starting solution. Circles can only reproduce parts of a meniscus and due to the limited number of pixels to fit, showed high uncertainties in their fitted radius and hence the calculated contact angle. The simplest geometry is a straight line. Such a line introduces the optimization conflict between a short fitting length, giving more precise contact angles at cost of a higher uncertainty, and a longer fitting length with a less precise contact angle but also less measurement uncertainty.

When the roughness of the sample or the optical resolution becomes high enough to visibly resolve the roughness (in the order of pixels) the shadow technique cannot be applied anymore. At this resolution it becomes unclear which shape to use for fitting the sample surface and which angle to interpret as contact angle since the contact line visibly contacts the tilted surfaces of the single roughness elements instead of the average wall surface.

A.4 Bubble counting details

For the bubble counting technique a transparent liquid tank with flat front wall is needed. The camera is positioned horizontally in front of the liquid tank below the pool surface. The light source is aligned orthogonal to the camera on one side of the pool. In a first step the rough sample is immersed into the pool with the projected measurement speed with its rough surface pointing towards the camera. When the sample stopped moving, a camera picture of the rough surface and possible trapped bubbles (with glare points due to the orthogonal lighting) is taken. Afterwards the sample is pulled out of the pool and immersed again, this time with a very low speed to ensure good wetting. A second camera image of this perfectly wetted surface is taken.

In the post-processing the second image is subtracted from the first image to decrease the visibility of the rough sample background. Afterwards the outer borders of the bubbles are detected by reducing noise using Gaussian blurring with a 3px median, before applying the Sobel filter [140]. After these steps the image brightness should be close to zero on the largest part of the image, while the borders of the bubbles are the only remaining brighter elements. When expressed in a brightness histogram, this histogram is very flat with a steep peak around zero. In this histogram the outer end of the steep slope towards the peak at zero has to be searched in iterative steps to determine the limit between bubble borders and background noise. Afterwards a watershed algorithm using this limit is applied on the image to separate the bubbles and the background. To reduce detection errors, a minimum and a maximum size of estimated bubbles is given and detected bubbles outside this size range are discarded. Furthermore, a minimum roundness factor F_{\min} is used to filter out non circular objects, as exemplary shown in Fig. A.1. This factor is used to compare the perimeter length l_{per} and the inner area A_{inner} (area without the one pixel wide border line) of detected objects with the perimeter length and inner area of perfect circles. At first the equivalent circle radius r for the full object area A is calculated to be

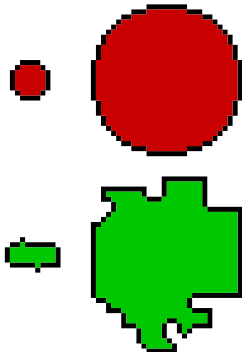


Figure A.1: An example of small (left) and large (right) detected objects with either circular (red) or irregular shape (green). Table A.1 gives the parameters of this objects described by Eqs. (A.3)-(A.5).

$$r = \sqrt{\frac{A}{\pi}}. \quad (\text{A.3})$$

In order to fulfil the roundness requirement the perimeter length has to be

$$l_{\text{per}} \leq F_{\text{min}} 2\pi r, \quad (\text{A.4})$$

while the inner area (without one pixel border) has to be

$$A_{\text{inner}} \geq \frac{(r-1)^2 \pi}{F_{\text{min}}}. \quad (\text{A.5})$$

This system of two requirements is chosen because pixel objects with sizes of $\mathcal{O}(10)$ cannot approximate circles smoothly as demonstrated in Table A.1. The F_{min} values for non circular objects should always be above one, but F_{min} of the small irregular object calculated with l_{per} is only 0.960, predicting a shorter perimeter than for a perfect circle. When

		l_{per} [px]	A_{inner} [px]	A [px]	r [px]
small	circle	20	32	52	4.068
	irregular	25	29	54	4.146
difference		25 %	9 %	4 %	2 %
F_{min}		0.960	1.072		
large	circle	84	640	724	15.18
	irregular	124	640	764	15.59
difference		48 %	0 %	6 %	3 %
F_{min}		1.266	1.045		

Table A.1: Parameters from Eqs. (A.3)-(A.5) for the objects given in Fig. A.1.

calculating this F_{min} value for the small circle, the value is 0.782, lower than the irregular shape but not one which it should be in theory. The larger irregular shape has a l_{per} based F_{min} of 1.266 and with this can be identified as (to a certain degree) non-circular object. But even at this size the circle approximation is poor, leading to a l_{per} based F_{min} of the big red circle of only 0.881. It can be seen that the pixel wise circle approximation becomes better for larger objects but it cannot be guaranteed that the l_{per} based F_{min} of non-circular objects will be above one. Hence Eq. (A.5) is also checked, which is less sensitive to non-circular shapes (as can be seen in Table A.1) but is more likely to result in F_{min} values above one for non-circular objects.

Another filtering checks the minimal distance between objects and combines objects in close vicinity to each other into one object. With this, errors due to multiple glare points and similar optical issues leading to multiple recognition of bubbles are corrected.

A.5 Laser refraction details

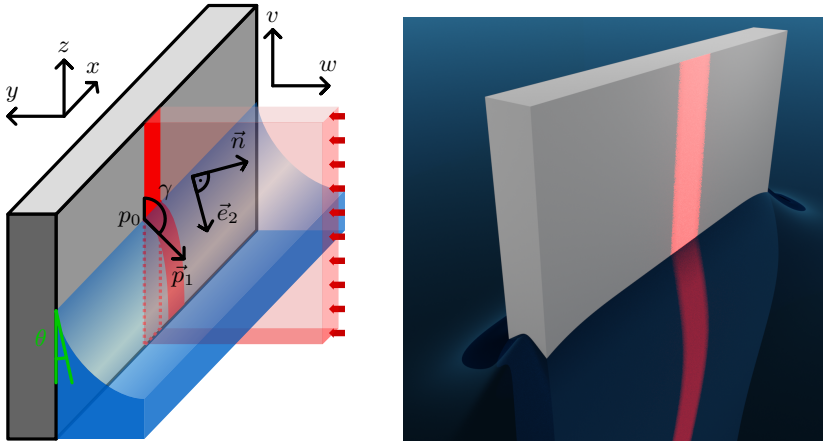


Figure A.2: Left: A sketch of a laser light sheet orthogonally illuminating a sample, resulting in a vertical red line (dotted frame below the liquid surface). Due to liquid refraction a kink and a bending of the red laser line is visible in the camera. Right: The same situation shown in a ray tracing 3D render to give better insight into the real phenomenon.

Fig. A.2 sketches the physical principle of the laser refraction technique on the left and demonstrates the physical effect in a computer simulation on the right. For this method a vertical laser sheet is aligned orthogonal to the sample surface in order to project a straight vertical line onto the sample. The 2D liquid meniscus is only curved inside the laser plane which lets the refraction stay inside this plane, not affecting the shape and position of the laser line on the sample. The camera is positioned tilted to this plane, as depicted in Fig. A.2, which leads to a visible refraction of the laser line below the liquid surface. The value used for contact angle calculation is the kink angle γ directly at the contact line. In the following calculation vectors are rotated around the x and z axes

of the sample shown in the left of Fig. A.2. The rotation matrix around x is defined as

$$\mathbf{R}_x(\alpha) = \begin{pmatrix} 1 & 0 & 0 \\ 0 & \cos(\alpha) & -\sin(\alpha) \\ 0 & \sin(\alpha) & \cos(\alpha) \end{pmatrix} \quad (\text{A.6})$$

and the rotation matrix around z is defined as

$$\mathbf{R}_z(\alpha) = \begin{pmatrix} \cos(\alpha) & -\sin(\alpha) & 0 \\ \sin(\alpha) & \cos(\alpha) & 0 \\ 0 & 0 & 1 \end{pmatrix}. \quad (\text{A.7})$$

The calculation is based on an orthographic camera projection, which can be achieved by a telecentric lens or a negligible influence of the camera opening angle (see Eq. (3.2)) by either having a low value α_{cam} or filming the contact line in the center of the camera image. The rotation of the camera towards the sample has to be measured for this technique. The tilting of the camera towards the horizontal plane is denoted τ and the rotation around the vertical axis, relative to the front face of the sample, is denoted α . The view direction of the camera \vec{s}_1 follows to be

$$\vec{s}_1 = \mathbf{R}_z(-\alpha) \cdot \mathbf{R}_x(-\tau) \cdot \vec{e}_y, \quad (\text{A.8})$$

with \vec{e}_y being the unit vector in the y direction. The normal vector \vec{n} of the liquid close to the contact line depends on the contact angle θ and is formed by rotating $-\vec{e}_y$ in negative x direction

$$\vec{n} = \mathbf{R}_x(-\theta) \cdot (-\vec{e}_y). \quad (\text{A.9})$$

Snells's law gives the view direction of the camera after refraction through the liquid surface \vec{s}_2 to be

$$\vec{s}_2 = \frac{n_g}{n_l} [\vec{n} \times ((-\vec{n}) \times \vec{s}_1)] - \vec{n} \sqrt{1 - \left(\frac{n_g}{n_l}\right)^2 (\vec{n} \times \vec{s}_1) \cdot (\vec{n} \times \vec{s}_1)} \quad (\text{A.10})$$

using the indices of refraction for the gas phase n_g and the liquid phase n_l . In the top right of the left part of Fig. A.2, a 2D coordinate system with the axes v and w is shown. This coordinate system is in the plane of the image and hence in the camera plane. The directions of the unit vectors into v and w in the 3D coordinate system are given by

$$\vec{e}_w = \mathbf{R}_z(-\alpha) \cdot \vec{e}_x \quad (\text{A.11})$$

and

$$\vec{e}_v = \mathbf{R}_z(-\alpha) \cdot \mathbf{R}_x(-\tau) \cdot \vec{e}_z. \quad (\text{A.12})$$

The direction of the refracted laser line at the kink is given by an unit vector \vec{p}_1 . Its visible projection in the v - w camera plane is denoted \vec{p}_1^* . With the visible kink angle being γ and the origin of both coordinate systems defined to be at p_0 , \vec{p}_1^* is

$$\vec{p}_1^* = \sin(\gamma) \cdot \vec{e}_w + \cos(\gamma) \cdot \vec{e}_v. \quad (\text{A.13})$$

In order to project \vec{p}_1^* from the camera plane onto the liquid surface, the surface close to the contact line has to be linearized into a plane. One axis of this plane is equal to \vec{e}_x while the second axis \vec{e}_2 is

$$\vec{e}_2 = \mathbf{R}_x(-\theta) \cdot (-\vec{e}_z). \quad (\text{A.14})$$

\vec{p}_1^* can be projected onto this plane along the camera view axis using the following equation system with three equations and three parameters a_1 to a_3 :

$$\vec{p}_1^* + a_1 \vec{s}_1 = a_2 \vec{e}_x + a_3 \vec{e}_2. \quad (\text{A.15})$$

Both sides of Eq. A.15 are equal to \vec{p}_1 and can be used to calculate it after calculating the parameters a_1 to a_3 .

In the next calculation step the refracted camera view axis \vec{s}_2 is used to calculate the ray length between the unit vector \vec{p}_1 on the liquid surface and the real laser line at the sample surface. It is known a priori that the real laser line is at x and y positions zero (since p_0 was defined as origin of the coordinate systems) which gives the following two conditions for the ray length l_{ray} :

$$l_{\text{ray},1} = \frac{p_{1,x}}{s_{2,x}} \quad (\text{A.16})$$

and

$$l_{\text{ray},2} = -\frac{p_{1,y}}{s_{2,y}}. \quad (\text{A.17})$$

The difference between $l_{\text{ray},1}$ and $l_{\text{ray},2}$ should be zero for a correct equation system. Since θ is unknown but needed for the calculation beginning with Eq. A.9, the calculation can be used to iteratively solve for θ by minimizing the difference between $l_{\text{ray},1}$ and $l_{\text{ray},2}$ starting from a starting solution for θ . For this iterative solution the difference between $l_{\text{ray},1}$ and $l_{\text{ray},2}$ is calculated for two slightly different values of θ to gain a gradient, which can be used in a gradient algorithm like the Gauss-Newton algorithm.

A validation of this measurement method was performed from Weidler in his Bachelor thesis [94] and showed qualitative agreement with the expected dynamic contact angles. Despite the promising results this method was not used further since some technical limitations become obvious. To receive a precise kink angle γ , the sample is not allowed to be too rough to avoid the border of the laser line to become fuzzy. What is more, the laser light sheet has to have a rectangular beam intensity to avoid blurriness of the border. No such laser setup could be found without building a custom laser system. Also most of the rough samples

analyzed in the course of this thesis had significant amounts of roughness, making this method unsuitable for them.

A.6 Liquid data

Liquid	Viscosity		Density	Surface tension
	[mm ² /s]	[mPa s]	[kg/m ³]	[mN/m]
PDMS-10	10	9.45	945	20.2
PDMS-20	20	19.1	955	20.6
PDMS-50	50	48	960	20.8
PDMS-100	100	96.3	963	20.9
Water	0.8940	0.8914	997.1	72.15
Ethanol	1.399	1.0995	785.8	22.07
Ethylene glycol	15.64	17.34	1109	48.91
Acetone*	0.4365	0.3439	787.8	22.996
Glycerine	803.6	1011	1258.02	62.24
Sunflower oil**	5.386	4.955	920	33.10

Table A.2: The most important physical properties of the (pure) liquids used or tested in this thesis (at 25 °C). [141–146]

* For acetone no measurement temperature is given by [144].

** The density of sunflower oil is given at 15 °C by [146], the other values are based on own measurements.

A.7 Surface roughness values

	Sandblasting	Milling	Polishing
S_z [μm]	53-83	2.8	0.5
S_a [μm]	2.5-4.2	2.7×10^{-1}	3.1×10^{-2}
S_q [μm]	4.1-6.3	3.4×10^{-1}	3.8×10^{-2}
Additional surface	19-34 %	2×10^{-1} %	5×10^{-3} %

Table A.3: Roughness parameters resulting from different subtractive fabrication methods used for aluminum samples. S_z is highest measured height difference on the observed surface area. S_a is the average absolute height and S_q the average quadratic height of the roughness. The additional surface is equal to $(A_{real} - A_{app})/A_{app}$ or $r - 1$. Data from the Bachelor thesis of Weidler [94].

Bibliography

- [1] Stephan F. Kistler and Peter M. Schweizer, eds. *Liquid Film Coating: Scientific principles and their technological implications*. London: Chapman & Hall, 1997. ISBN: 0-412-06481-2.
- [2] Hadj Benkreira. “The effect of substrate roughness on air entrainment in dip coating”. In: *Chemical Engineering Science* 59.13 (2004), pp. 2745–2751. DOI: [10.1016/j.ces.2004.03.024](https://doi.org/10.1016/j.ces.2004.03.024).
- [3] Meng-Hua Zhao, Xiao-Peng Chen, and Qing Wang. “Wetting failure of hydrophilic surfaces promoted by surface roughness.” In: *Sci Rep* 4 (June 2014), p. 5376. DOI: [10.1038/srep05376](https://doi.org/10.1038/srep05376). URL: <https://www.ncbi.nlm.nih.gov/pubmed/24948390>.
- [4] Kwang Taek Hong, Harris Imadojemu, and R. L. Webb. “Effects of Oxidation and Surface Roughness on Contact Angle”. In: *Experimental Thermal and Fluid Science* 8 (1994), pp. 279–285.
- [5] R. Krechetnikov and G. M. Homsy. “Experimental study of substrate roughness and surfactant effects on the Landau-Levich law”. In: *Physics of Fluids* 17 (Oct. 2005), pp. 102108–102108–16. DOI: [10.1063/1.2112647](https://doi.org/10.1063/1.2112647). URL: <http://adsabs.harvard.edu/abs/2005PhFl...17j2108K>.
- [6] K.J. Kubiak et al. “Wettability versus roughness of engineering surfaces”. In: *Wear* 271.3-4 (2011), pp. 523–528. DOI: [10.1016/j.wear.2010.03.029](https://doi.org/10.1016/j.wear.2010.03.029).
- [7] Ł. Sadowski, S. Czarnecki, and J. Hoła. “Evaluation of the height 3D roughness parameters of concrete substrate and the adhesion to epoxy resin”. In: *International Journal of Adhesion and Adhesives* 67 (2016), pp. 3–13. DOI: [10.1016/j.ijadhadh.2015.12.019](https://doi.org/10.1016/j.ijadhadh.2015.12.019).

Bibliography

- [8] Alexandr Malijevský. “Does surface roughness amplify wetting?” In: *J Chem Phys* 141.18 (Nov. 2014), p. 184703. DOI: [10.1063/1.4901128](https://doi.org/10.1063/1.4901128). URL: <https://www.ncbi.nlm.nih.gov/pubmed/25399155>.
- [9] Emil Chibowski. “On some relations between advancing, receding and Young’s contact angles”. In: *Adv Colloid Interface Sci* 133.1 (May 2007), pp. 51–9. DOI: [10.1016/j.cis.2007.03.002](https://doi.org/10.1016/j.cis.2007.03.002). URL: <https://www.ncbi.nlm.nih.gov/pubmed/17448435>.
- [10] Edward W. Washburn. “The Dynamics of Capillary Flow”. In: *Physical Review* 17.3 (Mar. 1921), pp. 273–283. DOI: [10.1103/physrev.17.273](https://doi.org/10.1103/physrev.17.273).
- [11] W. J. O’Brien, R. G. Craig, and F. A. Peyton. “Capillary Penetration between Dissimilar Solids”. In: *J Colloid Interface Sci* 26.4 (Apr. 1968), pp. 500–508. DOI: [10.1016/0021-9797\(68\)90298-1](https://doi.org/10.1016/0021-9797(68)90298-1).
- [12] H.M. Princen. “Capillary Phenomena in Assemblies of Parallel Cylinders”. In: *J Colloid Interface Sci* 30.1 (May 1969), pp. 69–75.
- [13] Alexandre Ponomarenko, David Quéré, and Christophe Clanet. “A universal law for capillary rise in corners”. In: *J. Fluid Mech.* 666 (2011), pp. 146–154. DOI: [10.1017/S0022112010005276](https://doi.org/10.1017/S0022112010005276).
- [14] Selin Manukyan. “Fundamental Investigation of Forced Wetting on Structured Surfaces”. PhD thesis. Darmstadt: Technical University of Darmstadt, 2013.
- [15] Daniel Bonn et al. “Wetting and spreading”. In: 81.2 (2009), pp. 739–805. DOI: [10.1103/RevModPhys.81.739](https://doi.org/10.1103/RevModPhys.81.739).
- [16] Thomas Young. “An Essay on the Cohesion of Fluids”. In: *Phil. Trans.* 95 (1805), pp. 65–87. DOI: [10.1098/rstl.1805.0005](https://doi.org/10.1098/rstl.1805.0005).
- [17] Pierre Simon de Laplace. *Mechanique Celeste Supplement au X Livre*. Paris: Courier, 1805.
- [18] Chun Huh and L.E. Scriven. “Hydrodynamic Model of Steady Movement of a Solid/Liquid/Fluid Contact Line”. In: *J Colloid Interface Sci* 35.1 (1971), pp. 85–101. DOI: [10.1016/0021-9797\(71\)90188-3](https://doi.org/10.1016/0021-9797(71)90188-3).

- [19] Peter A. Thompson and Sandra M. Troian. “A general boundary condition for liquid flow at solid surfaces”. In: *Nature* 389 (1997), pp. 360–362.
- [20] H. Hervet and P.-G. de Gennes. “The dynamics of wetting precursor films in the wetting of “dry” solids”. In: *Comptes-rendus des séances de l’Académie des sciences. Série 2, Mécanique-physique, chimie, sciences de l’univers, sciences de la terre* 299.9 (1984), pp. 499–503.
- [21] H Pirouz Kavehpour, Ben Ovryn, and Gareth H McKinley. “Microscopic and macroscopic structure of the precursor layer in spreading viscous drops”. In: *Phys Rev Lett* 91.19 (Nov. 2003), p. 196104. DOI: [10.1103/PhysRevLett.91.196104](https://doi.org/10.1103/PhysRevLett.91.196104). URL: <https://www.ncbi.nlm.nih.gov/pubmed/14611592>.
- [22] M. H. Eres, L. W. Schwartz, and R. V. Roy. “Fingering phenomena for driven coating films”. In: *Physics of Fluids* 12 (June 2000), pp. 1278–1295. DOI: [10.1063/1.870382](https://doi.org/10.1063/1.870382). URL: <http://adsabs.harvard.edu/abs/2000PhFl...12.1278E>.
- [23] L.M. Hocking. “A moving fluid interface on a rough surface”. In: *J. Fluid Mech.* 76.4 (Aug. 1976), pp. 801–817. DOI: [10.1017/S0022112076000906](https://doi.org/10.1017/S0022112076000906).
- [24] D. E. Weidner and L. W. Schwartz. “Contact-line motion of shear-thinning liquids”. In: *Physics of Fluids* 6 (Nov. 1994), pp. 3535–3538. DOI: [10.1063/1.868412](https://doi.org/10.1063/1.868412). URL: <http://adsabs.harvard.edu/abs/1994PhFl...6.3535W>.
- [25] A Boudaoud. “Non-Newtonian thin films with normal stresses: dynamics and spreading.” In: *Eur Phys J E Soft Matter* 22.2 (Feb. 2007), pp. 107–9. DOI: [10.1140/epje/e2007-00026-9](https://doi.org/10.1140/epje/e2007-00026-9). URL: <https://www.ncbi.nlm.nih.gov/pubmed/17377751>.
- [26] Peter C. Wayner. “Spreading of a liquid film with a finite contact angle by the evaporation/condensation process”. In: *Langmuir* 9 (1993), pp. 294–299. DOI: [10.1021/la00025a056](https://doi.org/10.1021/la00025a056).
- [27] Pierre Seppecher. “Moving contact lines in the Cahn-Hilliard theory”. In: *International Journal of Engineering Science* 34.9 (1996), pp. 977–992.

Bibliography

- [28] Peter A. Thompson and Mark O. Robbins. “Simulations of contact-line motion: Slip and the dynamic contact angle”. In: *Physical Review Letters* 63.7 (1989), pp. 766–769. DOI: [10.1103/PhysRevLett.63.766](https://doi.org/10.1103/PhysRevLett.63.766).
- [29] Frank Schellenberger et al. “How Water Advances on Superhydrophobic Surfaces.” In: *Phys Rev Lett* 116.9 (Mar. 2016), p. 096101. DOI: [10.1103/PhysRevLett.116.096101](https://doi.org/10.1103/PhysRevLett.116.096101). URL: <https://www.ncbi.nlm.nih.gov/pubmed/26991185>.
- [30] R. Shuttleworth and G. L. J. Bailey. “The spreading of a liquid over a rough solid”. In: *Discuss. Faraday Soc.* 3 (1948), pp. 16–22. DOI: [10.1039/DF9480300016](https://doi.org/10.1039/DF9480300016).
- [31] Rulon E. Johnson and Robert H. Dettre. “Contact Angle Hysteresis”. In: *Contact Angle, Wettability, and Adhesion* 43 (1964), pp. 112–135. DOI: [10.1021/ba-1964-0043.ch007](https://doi.org/10.1021/ba-1964-0043.ch007).
- [32] Charles W. Extrand and Y. Kumagai. “An Experimental Study of Contact Angle Hysteresis”. In: *J Colloid Interface Sci* 191.2 (July 1997), pp. 378–383. DOI: [10.1006/jcis.1997.4935](https://doi.org/10.1006/jcis.1997.4935).
- [33] H. Kamusewitz, W. Possart, and D. Paul. “The relation between Young’s equilibrium contact angle and the hysteresis on rough paraffin wax surfaces”. In: *Colloids and Surfaces A: Physicochem. Eng. Aspects* 156.1-3 (Oct. 1999), pp. 271–279. DOI: [10.1016/S0927-7757\(99\)00079-5](https://doi.org/10.1016/S0927-7757(99)00079-5).
- [34] Jens Eggers. “Existence of receding and advancing contact lines”. In: *Physics of Fluids* 17 (Aug. 2005), pp. 082106–082106–10. DOI: [10.1063/1.2009007](https://doi.org/10.1063/1.2009007). URL: <http://adsabs.harvard.edu/abs/2005PhFl...17h2106E>.
- [35] D. Y. Kwok et al. “Contact Angle Measurements and Contact Angle Interpretation. 1. Contact Angle Measurements by Axisymmetric Drop Shape Analysis and a Goniometer Sessile Drop Technique”. In: *Langmuir* 13.10 (May 1997), pp. 2880–2894. DOI: [10.1021/la9608021](https://doi.org/10.1021/la9608021). URL: <https://doi.org/10.1021/2Fla9608021>.

- [36] E. B. Dussan V. “On the spreading of liquids on solid surfaces: Static and dynamic contact lines”. In: *Ann. Rev. Fluid Mech.* 11 (1979), pp. 371–400.
- [37] P. G. de Gennes. “Wetting: statics and dynamics”. In: *Rev. Mod. Phys.* 57.3 (1985), pp. 827–863. DOI: [10.1103/RevModPhys.57.827](https://doi.org/10.1103/RevModPhys.57.827).
- [38] Jing-Den Chen and N. Wada. “Wetting dynamics of the edge of a spreading drop”. In: *Physical Review Letters* 62.26 (June 1989), pp. 3050–3053. DOI: [10.1103/PhysRevLett.62.3050](https://doi.org/10.1103/PhysRevLett.62.3050).
- [39] John A. Marsh, Stephen Garoff, and E. B. Dussan V. “Dynamic contact angles and hydrodynamics near a moving contact line”. In: *Physical Review Letters* 70.18 (May 1993), pp. 2778–2781.
- [40] Claire Andrieu, Cécile Sykes, and Francoise Brochard. “Average Spreading Parameter on Heterogenous Surfaces”. In: *Langmuir* 10 (1994), pp. 2077–2080.
- [41] E. L. Decker and Stephen Garoff. “Using Vibrational Noise To Probe Energy Barriers Producing Contact Angle Hysteresis”. In: 12.8 (Apr. 1996), pp. 2100–2110. DOI: [10.1021/la951021n](https://doi.org/10.1021/la951021n).
- [42] E. L. Decker et al. “Physics of contact angle measurement”. In: *Colloids and Surfaces A: Physicochem. Eng. Aspects* 156.1-3 (Oct. 1999), pp. 177–189. DOI: [10.1016/S0927-7757\(99\)00069-2](https://doi.org/10.1016/S0927-7757(99)00069-2).
- [43] C. Della Volpe et al. “The determination of a ‘stable-equilibrium’ contact angle on heterogeneous and rough surfaces”. In: *Colloids and Surfaces A: Physicochem. Eng. Aspects* 206.1-3 (July 2002), pp. 47–67. DOI: [10.1016/S0927-7757\(02\)00072-9](https://doi.org/10.1016/S0927-7757(02)00072-9).
- [44] Tammar S Meiron, Abraham Marmur, and I Sam Saguy. “Contact angle measurement on rough surfaces.” In: *J Colloid Interface Sci* 274.2 (June 2004), pp. 637–44. DOI: [10.1016/j.jcis.2004.02.036](https://doi.org/10.1016/j.jcis.2004.02.036). URL: <https://www.ncbi.nlm.nih.gov/pubmed/15144840>.
- [45] Richard L Hoffman. “A study of the advancing interface. I. Interface shape in liquid-gas systems”. In: 50.2 (1975), pp. 228–241. DOI: [10.1016/0021-9797\(75\)90225-8](https://doi.org/10.1016/0021-9797(75)90225-8).

Bibliography

- [46] O. V. Voinov. “Hydrodynamics of wetting”. In: *Fluid Dyn* 11.5 (1976), pp. 714–721. DOI: [10.1007/BF01012963](https://doi.org/10.1007/BF01012963).
- [47] Stephan F. Kistler. “Hydrodynamics of Wetting”. In: *Wettability*. Ed. by John C. Berg. Vol. 49. Surfactant Science Series. New York: Marcel Dekker Inc., 1993. ISBN: 0-8247-9046-4.
- [48] Tsung-Shann Jiang, Soo-Gun Oh, and John C Slattery. “Correlation for dynamic contact angle”. In: *Journal of Colloid and Interface Science* 69.1 (Mar. 1979), pp. 74–77. DOI: [10.1016/0021-9797\(79\)90081-X](https://doi.org/10.1016/0021-9797(79)90081-X).
- [49] M. Bracke, F. De Voeght, and P. Joos. “The kinetics of wetting: the dynamic contact angle”. In: *Progr Colloid Polym Sci* 79 (1989), pp. 142–149. DOI: [10.1007/BFb0116200](https://doi.org/10.1007/BFb0116200).
- [50] Terence D Blake and Kenneth J Ruschak. “A maximum speed of wetting”. In: *Nature* 282 (Nov. 1979), pp. 489–491.
- [51] *PI LMS-180 data sheet*. Version from Sep. 18. 2020. Physik Instrumente (PI) GmbH & Co. KG. URL: https://web.archive.org/web/20200918125016/https://static.physikinstrumente.com/fileadmin/user_upload/physik_instrumente/files/datasheets/LMS-180_Datasheet.pdf.
- [52] *Airpel Plus Air Cylinders specifications*. Version from Aug. 21. 2018. Airpot Corporation. URL: <https://web.archive.org/web/20180821081526/http://airpot.com/product-category/product-lines/pneumatic-actuation/airpel-plus-air-cylinders/>.
- [53] *Series 3890 CR data sheet*. Version from Apr. 22. 2020. Dr. Fritz Faulhaber GmbH & Co. KG. URL: https://web.archive.org/web/20200422165422/https://www.faulhaber.com/fileadmin/Import/Media/EN_3890_CR_DFF.pdf.
- [54] *Series 38/2 S data sheet*. Version from Apr. 22. 2020. Dr. Fritz Faulhaber GmbH & Co. KG. URL: https://web.archive.org/web/20200422202820/https://www.faulhaber.com/fileadmin/Import/Media/EN_38-2S_FMM.pdf.

- [55] *SC 5008 S data sheet*. Version from Apr. 22. 2020. Dr. Fritz Faulhaber GmbH & Co. KG. URL: https://web.archive.org/web/20200422113329/https://www.faulhaber.com/fileadmin/Import/Media/EN_SC5008S_DFF.pdf.
- [56] *Programming adapter 6501 data sheet*. Version from Apr. 22. 2020. Dr. Fritz Faulhaber GmbH & Co. KG. URL: https://web.archive.org/web/20200422014254/https://www.faulhaber.com/fileadmin/Import/Media/EN_6501_0009X_DFF.pdf.
- [57] *Model 166H/169H data sheet*. Version from Sep. 18. 2020. BCM SENSOR TECHNOLOGIES bvba. URL: https://web.archive.org/web/20200918160225/https://www.bcmsensor.com/wp-content/uploads/2015/03/200605_166H_169H_Single_Point_Load_Cells.pdf.
- [58] Christian Braun et al. “Konstruktion einer Rakelbefestigung und Auswahl geeigneter Sensoren zur Erfassung von Umgebungsbedingungen”. Group project. Darmstadt: Technical University of Darmstadt, 2018.
- [59] D. J. M. Bergink-Martens et al. “Surface dilation and fluid-dynamical behavior of newtonian liquids in an overflowing cylinder: I. Pure liquids”. In: *Journal of Colloid and Interface Science* 138.1 (1990), pp. 1–9. DOI: [10.1016/0021-9797\(90\)90174-M](https://doi.org/10.1016/0021-9797(90)90174-M).
- [60] Colin D. Bain. “The overflowing cylinder sixty years on”. In: *Advances in Colloid and Interface Science* 144.1-2 (2008), pp. 4–12. DOI: [10.1016/j.cis.2008.08.006](https://doi.org/10.1016/j.cis.2008.08.006).
- [61] Hagop V. Panossian. “Structural damping optimization via non-obstructive particle damping technique”. In: *The Third Air Force/NASA Symposium on Recent Advances in Multidisciplinary Analysis and Optimization*. 1990, pp. 7–15.
- [62] Joshua I. Davis, Charles Birdsong, and Harold Cota. “Vibroacoustic study of circular cylindrical tubes in roller coaster rails”. In: *Noise Control Eng. J.* 59.4 (2011), pp. 333–340. DOI: [10.3397/1.3581429](https://doi.org/10.3397/1.3581429).

Bibliography

- [63] Felix Gerlach et al. “Rivulets of finite height”. In: *Colloids and Surfaces A: Physicochemical and Engineering Aspects* (2020). Accepted.
- [64] Felix Gerlach, Maximilian Hartmann, and Cameron Tropea. “The interaction of inner and outer surface corners during spontaneous wetting”. In: *Colloids and Surfaces A: Physicochemical and Engineering Aspects* 583 (2019), p. 123977. DOI: [10.1016/j.colsurfa.2019.123977](https://doi.org/10.1016/j.colsurfa.2019.123977).
- [65] P. S. Ayyaswamy, I. Catton, and D. K. Edwards. “Capillary Flow in Triangular Grooves”. In: *Journal of Applied Mechanics* 41 (1970), p. 332. DOI: [10.1115/1.3423288](https://doi.org/10.1115/1.3423288). URL: <http://adsabs.harvard.edu/abs/1974JAM...41..332A>.
- [66] Geoffrey Mason and Norman R. Morrow. “Meniscus curvatures in capillaries of uniform cross-section”. In: *Journal of the Chemical Society, Faraday Transactions 1: Physical Chemistry in Condensed Phases* 80.9 (1984), p. 2375. DOI: [10.1039/f19848002375](https://doi.org/10.1039/f19848002375).
- [67] Harris Wong, S Morris, and C.J Radke. “Three-dimensional menisci in polygonal capillaries”. In: *Journal of Colloid and Interface Science* 148.2 (Feb. 1992), pp. 317–336. DOI: [10.1016/0021-9797\(92\)90171-h](https://doi.org/10.1016/0021-9797(92)90171-h).
- [68] Lei-Han Tang and Yu Tang. “Capillary Rise in Tubes with Sharp Grooves”. In: *Journal de Physique II* (Jan. 1994). DOI: [10.1051/jp2:1994172](https://doi.org/10.1051/jp2:1994172). URL: <http://arxiv.org/pdf/cond-mat/9401031v1>.
- [69] A. Lopez de Ramos and R. L. Cerro. “Liquid filament rise in comers of square capillaries: a novel method for the measurement of small contact angles”. In: *Chemical Engineering Science* 49.14 (1994), pp. 2395–2398.
- [70] Mark M. Weislogel. “Capillary Flow in an Interior Corner”. PhD thesis. Nov. 1996.
- [71] Mark M. Weislogel. “Compound capillary rise”. In: *Journal of Fluid Mechanics* 709 (Oct. 2012), pp. 622–647. DOI: [10.1017/jfm.2012.357](https://doi.org/10.1017/jfm.2012.357). URL: <http://adsabs.harvard.edu/abs/2012JFM...709..622W>.

- [72] Mohammad Heshmati and Mohammad Piri. “Experimental investigation of dynamic contact angle and capillary rise in tubes with circular and noncircular cross sections.” In: *Langmuir* 30.47 (Dec. 2014), pp. 14151–62. DOI: [10.1021/la501724y](https://doi.org/10.1021/la501724y). URL: <https://www.ncbi.nlm.nih.gov/pubmed/25323811>.
- [73] F. Fouzia Ouali et al. “Wetting considerations in capillary rise and imbibition in closed square tubes and open rectangular cross-section”. In: *Microfluid Nanofluid* 15.3 (2013), pp. 309–326. DOI: [10.1007/s10404-013-1145-5](https://doi.org/10.1007/s10404-013-1145-5).
- [74] Vignesh Thammanna Gurumurthy et al. “Computations of spontaneous rise of a rivulet in a corner of a vertical square capillary”. In: *Colloids and Surfaces A: Physicochem. Eng. Aspects* 544 (May 2018), pp. 118–126. DOI: [10.1016/j.colsurfa.2018.02.003](https://doi.org/10.1016/j.colsurfa.2018.02.003).
- [75] Paul Concus and Robert Finn. “On the behavior of a capillary surface in a wedge”. In: *Proc Natl Acad Sci U S A* 63.2 (June 1969), pp. 292–299. DOI: [10.1073/pnas.63.2.292](https://doi.org/10.1073/pnas.63.2.292).
- [76] R. R. Rye, F. G. Yost, and J. A. Jr. Mann. “Wetting Kinetics in Surface Capillary Grooves”. In: *Langmuir* 12 (1996), pp. 4625–4627. DOI: [10.1021/la9605201](https://doi.org/10.1021/la9605201).
- [77] F. G. Yost, R. R. Rye, and J. A. Jr. Mann. “Solder wetting kinetics in narrow V-grooves”. In: *Acta mater.* 45.12 (1997), pp. 5337–5345. DOI: [10.1016/S1359-6454\(97\)00205-X](https://doi.org/10.1016/S1359-6454(97)00205-X).
- [78] M. M. Weislogel. “Capillary flow in interior corners: The infinite column”. In: *Physics of Fluids* 13 (Nov. 2001), pp. 3101–3107. DOI: [10.1063/1.1408918](https://doi.org/10.1063/1.1408918). URL: <http://adsabs.harvard.edu/abs/2001PhFl...13.3101W>.
- [79] Mark M. Weislogel. “Some analytical tools for fluids management in space: Isothermal capillary flows along interior corners”. In: *ASR* 32.2 (July 2003), pp. 163–170. DOI: [10.1016/S0273-1177\(03\)90247-X](https://doi.org/10.1016/S0273-1177(03)90247-X).
- [80] Ralf Seemann et al. “Wetting morphologies at microstructured surfaces”. In: *PNAS* 102.6 (Feb. 2005), pp. 1848–1852. DOI: [10.1073/pnas.0407721102](https://doi.org/10.1073/pnas.0407721102).

Bibliography

- [81] Yongkang Chen, Mark M. Weislogel, and Cory L. Nardin. “Capillary-driven flows along rounded interior corners”. In: *Journal of Fluid Mechanics* 566 (Nov. 2006), pp. 235–271. DOI: [10.1017/S0022112006001996](https://doi.org/10.1017/S0022112006001996). URL: <http://adsabs.harvard.edu/abs/2006JFM...566..235C>.
- [82] Shao-Wen Chen et al. “Experimental investigation and visualization on capillary and boiling limits of micro-grooves made by different processes”. In: *Sensors and Actuators A: Physical* 139.1-2 (2007), pp. 78–87. DOI: [10.1016/j.sna.2007.03.009](https://doi.org/10.1016/j.sna.2007.03.009).
- [83] F. J. Higuera, A. Medina, and A. Liñán. “Capillary rise of a liquid between two vertical plates making a small angle”. In: *Physics of Fluids* 20 (Oct. 2008), pp. 102102–102102–7. DOI: [10.1063/1.3000425](https://doi.org/10.1063/1.3000425). URL: <http://adsabs.harvard.edu/abs/2008PhFl...20j2102H>.
- [84] Yongkang Chen et al. “Capillary driven flow in micro scale surface structures”. In: *Microelectronic Engineering* 86.4-6 (2009), pp. 1317–1320. DOI: [10.1016/j.mee.2009.02.016](https://doi.org/10.1016/j.mee.2009.02.016).
- [85] Daxiang Deng et al. “Characterization of capillary rise dynamics in parallel micro V-grooves”. In: *International Journal of Heat and Mass Transfer* 77 (2014), pp. 311–320. DOI: [10.1016/j.ijheatmasstransfer.2014.05.003](https://doi.org/10.1016/j.ijheatmasstransfer.2014.05.003).
- [86] Mars M. Alimov and Konstantin G. Kornev. “Singularities of meniscus at the V-shaped edge”. In: *Mechanics Research Communications* 62 (2014), pp. 162–167. DOI: [10.1016/j.mechrescom.2014.10.003](https://doi.org/10.1016/j.mechrescom.2014.10.003).
- [87] Marie Tani et al. “Towards combinatorial mixing devices without any pumps by open-capillary channels: fundamentals and applications.” In: *Sci Rep* 5 (June 2015), p. 10263. DOI: [10.1038/srep10263](https://doi.org/10.1038/srep10263). URL: <https://www.ncbi.nlm.nih.gov/pubmed/26103562>.
- [88] Ophélie Raimbault et al. “The effects of femtosecond laser-textured Ti-6Al-4V on wettability and cell response.” In: *Mater Sci Eng C Mater Biol Appl* 69 (Dec. 2016), pp. 311–20. DOI: [10.1016/j.mbs.2016.10.003](https://doi.org/10.1016/j.mbs.2016.10.003).

- msec.2016.06.072. URL: <https://www.ncbi.nlm.nih.gov/pubmed/27612718>.
- [89] Vignesh Thammanna Gurumurthy et al. “Spontaneous rise in open rectangular channels under gravity.” In: *J Colloid Interface Sci* 527 (Oct. 2018), pp. 151–158. DOI: [10.1016/j.jcis.2018.05.042](https://doi.org/10.1016/j.jcis.2018.05.042). URL: <https://www.ncbi.nlm.nih.gov/pubmed/29793169>.
- [90] Felix Gerlach et al. “Capillary rivulet rise in real-world corners”. In: *Colloids and Surfaces A: Physicochemical and Engineering Aspects* 592 (2020), p. 124530. DOI: [10.1016/j.colsurfa.2020.124530](https://doi.org/10.1016/j.colsurfa.2020.124530).
- [91] Anthony M Schwartz and Silvestre B Tejada. “Studies of dynamic contact angles on solids”. In: *Journal of Colloid and Interface Science* 38.2 (1972), pp. 359–375. DOI: [10.1016/0021-9797\(72\)90252-4](https://doi.org/10.1016/0021-9797(72)90252-4).
- [92] R Ourahmoune et al. “Surface morphology and wettability of sandblasted PEEK and its composites.” In: *Scanning* 36.1 (2014), pp. 64–75. DOI: [10.1002/sca.21089](https://doi.org/10.1002/sca.21089). URL: <https://www.ncbi.nlm.nih.gov/pubmed/23553954>.
- [93] Till Felix Feldner. “Wetting and dewetting of rough and smooth surfaces with variation of kinematic conditions”. B.S. Thesis. Darmstadt: Technical University of Darmstadt, 2018.
- [94] Fabian Weidler. “Investigation of the critical wetting parameters of technical surfaces”. B.S. Thesis. Darmstadt: Technical University of Darmstadt, 2019.
- [95] Ludwig Wilhelmy. “Ueber die Abhängigkeit des Capillaritäts-Coëfficienten der Flüssigkeiten von der chemischen Beschaffenheit und Gestalt der festen Wand”. In: *Ann. Phys.* 198.5 (1864), pp. 1–17. DOI: [10.1002/andp.18641980502](https://doi.org/10.1002/andp.18641980502).
- [96] *pco.edge 5.5 data sheet*. Version from Sep. 10. 2020. PCO AG. URL: https://web.archive.org/web/20200910135247/https://www.pco.de/fileadmin/user_upload/pco-product_sheets/pco.edge_55_data_sheet.pdf.
- [97] *LED Shadow web page*. Version from May 12. 2020. Chauvet DJ. URL: <https://web.archive.org/web/20200512114529/https://www.chauvetdj.com/products/led-shadow/>.

Bibliography

- [98] *Model 120E specification sheet*. Version from Sep. 21. 2020. Veritas, a division of Integrated Design Tools, Inc. (IDT, Inc.) URL: https://web.archive.org/web/20200921072253/https://veritaslight.com/docs/constellation120E_spec_sheet.pdf.
- [99] E. Ramé, S. Garoff, and K. R. Willson. “Characterizing the microscopic physics near moving contact lines using dynamic contact angle data”. In: *Physical Review E* 70.3 (Sept. 2004). DOI: [10.1103/physreve.70.031608](https://doi.org/10.1103/physreve.70.031608).
- [100] Christophe Clanet and David Quéré. “Onset of menisci”. In: *Journal of Fluid Mechanics* 460 (2002). DOI: [10.1017/S002211200200808X](https://doi.org/10.1017/S002211200200808X).
- [101] *SHT7x web page*. Version from Jun. 16. 2020. Sensirion AG. URL: <https://web.archive.org/web/20200616054754/https://www.sensirion.com/en/environmental-sensors/humidity-sensors/pintype-digital-humidity-sensors/>.
- [102] *MPXAZ4115A Data Sheet*. Version from Sep. 21. 2020. NXP Semiconductors. URL: <http://web.archive.org/web/20200921143603/https://eu.mouser.com/datasheet/2/302/MPXAZ4115A-1127122.pdf>.
- [103] *PT 100 data sheet*. Version from Sep. 24. 2020. B+B Thermo-Technik GmbH. URL: <http://web.archive.org/web/20200924132958/https://asset.conrad.com/media10/add/160267/c1/-/gl/000125028DS01/datenblatt-125028-tauchfuehler-b-b-thermo-technik-pt100-40-bis-180-c-pt100.pdf>.
- [104] *W-SZK data sheet*. Version from Sep. 21. 2020. Heraeus Nexensos GmbH. URL: http://web.archive.org/web/20200921145400/https://asset.re-in.de/add/160267/c1/-/de/000189081DS01/DA_Heraeus-Nexensos-W-SZK-0-PT1000-Platin-Temperatursensor-20-bis-100C-1000-3850-ppm-K.pdf.

- [105] *NI 6002 Device Specification*. Version from Jul. 14. 2020. National Instruments Corp. URL: <https://web.archive.org/web/20200714034752/https://www.ni.com/pdf/manuals/374371a.pdf>.
- [106] *NI 9219 Datasheet*. Version from Aug. 20. 2020. National Instruments Corp. URL: https://web.archive.org/web/20200820043919/https://www.ni.com/pdf/manuals/377223a_02.pdf.
- [107] Felix Gerlach, Stephen Garoff, and Cameron Tropea. “Quantitative optical measurement of contact lines on millimeter scale metal structures dipped into a liquid pool”. In: *Proc. 19th Int. Symp. Application of Laser and Imaging Techniques to Fluid Mechanics*. 2018, pp. 862–875. ISBN: 978-989-20-9177-8.
- [108] Maximilian Diebold. “Light-Field Imaging and Heterogeneous Light Fields”. PhD thesis. Heidelberg University, 2016.
- [109] Jeffrey W Bullard and Edward J Garboczi. “Capillary rise between planar surfaces.” In: *Phys Rev E Stat Nonlin Soft Matter Phys* 79.1 Pt 1 (Jan. 2009), p. 011604. DOI: [10.1103/PhysRevE.79.011604](https://doi.org/10.1103/PhysRevE.79.011604). URL: <https://www.ncbi.nlm.nih.gov/pubmed/19257042>.
- [110] James Jurin. “An account of some experiments shown before the Royal Society; with an enquiry into the cause of some of the ascent and suspension of water in capillary tubes”. In: *Philosophical Transactions of the Royal Society of London*: 30 (1718), pp. 739–747. URL: <https://books.google.de/books?id=NUVFAAAACAAJ>.
- [111] James Jurin. “An account of some new experiments, relating to the action of glass tubes upon water and quicksilver”. In: *Philosophical Transactions of the Royal Society of London*: 30 (1719), pp. 1083–1096. URL: <https://books.google.com/books?id=NUVFAAAACAAJ>.
- [112] Joachim Schoelkopf et al. “Influence of inertia on liquid absorption into paper coating structures”. In: *Nordic Pulp and Paper Research Journal* 15.5 (2000), pp. 422–430.

Bibliography

- [113] Kenneth A. Brakke. “The Surface Evolver”. In: *Experimental Mathematics* 1.2 (1992), pp. 141–165. DOI: [1058-6458/92](https://doi.org/10.1058-6458/92).
- [114] Leonhard Euler. *Institutionum calculi integralis*. https://archive.org/details/bub_gb_yRsPAAAAIAAJ, <https://archive.org/details/leonhardieuleri06eulegoog>, <https://archive.org/details/leonhardieuleri05eulegoog>, <https://archive.org/details/leonhardieuleri01eulegoog>. Impensis Academiae Imperialis Scientiarum.
- [115] Carl Friedrich Gauss. *Theoria motus corporum coelestium in sectionibus conicis solem ambientium*. Sumtibus F. Perthes et I.H. Besser, 1809. URL: https://archive.org/details/bub_gb_ORUOAAAAQAAJ.
- [116] George Gabriel Stokes. “On the theories of the internal friction of fluids in motion and of the equilibrium and motion of elastic solids”. In: *Transactions of the Cambridge Philosophical Society* 8 (Apr. 1845), pp. 287–319. URL: <https://babel.hathitrust.org/cgi/pt?id=umn.31951d000213721&view=1up&seq=305>.
- [117] Robert N. Wenzel. “Resistance of solid surfaces to wetting by water”. In: *Industrial and engineering chemistry* 28.8 (Aug. 1936), pp. 988–994.
- [118] A. B. D. Cassie and S. Baxter. “Wettability of porous surfaces”. In: *Transactions of the Faraday Society* 40 (1944), p. 546. DOI: [10.1039/tf9444000546](https://doi.org/10.1039/tf9444000546).
- [119] C. Buchanan and L. Gardner. “Metal 3D printing in construction: A review of methods, research, applications, opportunities and challenges”. In: *Engineering Structures* 180 (Feb. 2019), pp. 332–348. DOI: [10.1016/j.engstruct.2018.11.045](https://doi.org/10.1016/j.engstruct.2018.11.045).
- [120] Leonard W. Schwartz and Stephen Garoff. “Contact angle hysteresis on heterogeneous surfaces”. In: *Langmuir* 1.2 (1985), pp. 219–230. DOI: [10.1021/la00062a007](https://doi.org/10.1021/la00062a007). URL: <http://pubs.acs.org/doi/pdf/10.1021/la00062a007>.
- [121] A. Menchaca-Rocha. “The mobility of mercury drops on rough glass surfaces”. In: *Journal of Colloid and Interface Science* 149.2 (1992), pp. 472–480. DOI: [10.1016/0021-9797\(92\)90434-N](https://doi.org/10.1016/0021-9797(92)90434-N).

- [122] Gershon Wolansky and Abraham Marmur. “Apparent contact angles on rough surfaces: the Wenzel equation revisited”. In: *Colloids and Surfaces A: Physicochemical and Engineering Aspects* 156 (1999), pp. 381–388. DOI: [10.1016/S0927-7757\(99\)00098-9](https://doi.org/10.1016/S0927-7757(99)00098-9).
- [123] G. Palasantzas and J. Th. M. De Hosson. “Wetting on rough surfaces”. In: *Acta mater.* 49 (2001), pp. 3533–3538. DOI: [10.1016/S1359-6454\(01\)00238-5](https://doi.org/10.1016/S1359-6454(01)00238-5).
- [124] José Bico, C Tordeux, and David Quéré. “Rough wetting”. In: *EPL* 55.2 (2001), pp. 214–220.
- [125] José Bico, Uwe Thiele, and David Quéré. “Wetting of textured surfaces”. In: *Colloids and Surfaces A: Physicochem. Eng. Aspects* 206 (2002), pp. 41–46.
- [126] Abraham Marmur. “Wetting on Hydrophobic Rough Surfaces: To Be Heterogeneous or Not To Be?” In: *Langmuir* 19.20 (2003), pp. 8343–8348. DOI: [10.1021/la0344682](https://doi.org/10.1021/la0344682).
- [127] Alfredo Calvimontes, Marc Mauermann, and Cornelia Bellmann. “Topographical Anisotropy and Wetting of Ground Stainless Steel Surfaces”. In: *Materials* 5 (Dec. 2012), pp. 2773–2787. DOI: [10.3390/ma5122773](https://doi.org/10.3390/ma5122773). URL: <http://adsabs.harvard.edu/abs/2012Mate...5.2773C>.
- [128] Albert Weckenmann and Wito Hartmann. “Function-oriented method for the definition and verification of microstructured surfaces”. In: *Precision Engineering* 37.3 (2013), pp. 684–693. DOI: [10.1016/j.precisioneng.2013.01.013](https://doi.org/10.1016/j.precisioneng.2013.01.013).
- [129] Stefan Roland Bommer. “Benetzung nichttrivialer statischer und dynamischer Oberflächen”. PhD thesis. Saarbrücken: Universität des Saarlandes, 2015.
- [130] Juan Manuel Vazquez-Martinez et al. “Effects of Laser Microtexturing on the Wetting Behavior of Ti6Al4V Alloy”. In: *Coatings* 8.4 (2018), p. 145. DOI: [10.3390/coatings8040145](https://doi.org/10.3390/coatings8040145).
- [131] W. L. Wilkinson. “Entrainment of air by a solid surface entering a liquid/air interface”. In: *Chemical Engineering Science* 30.10 (1975), pp. 1227–1230. DOI: [10.1016/0009-2509\(75\)85044-5](https://doi.org/10.1016/0009-2509(75)85044-5).

Bibliography

- [132] R. Burley and B. S. Kennedy. “An experimental study of air entrainment at a solid/liquid/gas interface”. In: *Chemical Engineering Science* 31 (1976), pp. 901–911.
- [133] R. Burley and R. P. S. Jolly. “Entrainment of air into liquids by a high speed continuous solid surface”. In: *Chemical Engineering Science* 39.9 (1984), pp. 1357–1372. DOI: [10.1016/0009-2509\(84\)80069-X](https://doi.org/10.1016/0009-2509(84)80069-X).
- [134] R. A. Buonopane, E. B. Guttoff, and M. M. T. Rimore. “Effect of plunging tape surface properties on air entrainment velocity”. In: *AIChE J.* 32.4 (1986), pp. 682–683. DOI: [10.1002/aic.690320419](https://doi.org/10.1002/aic.690320419).
- [135] P. G. Simpkins and V. J. Kuck. “On air entrainment in coatings”. In: *Journal of Colloid and Interface Science* 263 (July 2003), pp. 562–571. DOI: [10.1016/S0021-9797\(03\)00347-3](https://doi.org/10.1016/S0021-9797(03)00347-3). URL: <http://adsabs.harvard.edu/abs/2003JCIS..263..562S>.
- [136] Terence D Blake, Rosemary A Dobson, and Kenneth J Ruschak. “Wetting at high capillary numbers.” In: *J Colloid Interface Sci* 279.1 (Nov. 2004), pp. 198–205. DOI: [10.1016/j.jcis.2004.06.057](https://doi.org/10.1016/j.jcis.2004.06.057). URL: <https://www.ncbi.nlm.nih.gov/pubmed/15380430>.
- [137] Jacco H Snoeijer et al. “Avoided critical behavior in dynamically forced wetting.” In: *Phys Rev Lett* 96.17 (May 2006), p. 174504. DOI: [10.1103/PhysRevLett.96.174504](https://doi.org/10.1103/PhysRevLett.96.174504). URL: <https://www.ncbi.nlm.nih.gov/pubmed/16712304>.
- [138] T. S. Chan et al. “Hydrodynamics of air entrainment by moving contact lines”. In: *Physics of Fluids* 25 (July 2013), pp. 074105–074105–19. DOI: [10.1063/1.4814466](https://doi.org/10.1063/1.4814466). URL: <http://arxiv.org/abs/1303.1321>.
- [139] *Althen 31E data sheet*. Version from Sep. 21. 2020. Althen GmbH Mess- und Sensortechnik. URL: <http://web.archive.org/web/20200921063926/https://www.althensensors.com/media/23485/model-31e-miniature-tension-and-compression-force-sensor-low-en.pdf>.
- [140] Irwin Sobel. “An Isotropic 3x3 Image Gradient Operator”. In: *Presentation at Stanford A.I. Project 1968* (Feb. 2014).

- [141] *Technical Information ELBESIL-ÖLE* B. L. Böwing GmbH, 2012.
- [142] Ibrahim Sadek Khattab et al. “Density, viscosity, and surface tension of water+ethanol mixtures from 293 to 323K”. In: *Korean Journal of Chemical Engineering* 29.6 (2012), pp. 812–817. DOI: [10.1007/s11814-011-0239-6](https://doi.org/10.1007/s11814-011-0239-6).
- [143] Nikos G. Tsierkezos and Ioanna E. Molinou. “Thermodynamic Properties of Water + Ethylene Glycol at 283.15, 293.15, 303.15, and 313.15 K”. In: *Journal of Chemical & Engineering Data* 43.6 (1998), pp. 989–993. DOI: [10.1021/je9800914](https://doi.org/10.1021/je9800914).
- [144] R. C. Ernst, E. E. Litkenhous, and J. W. Spanyer. “The Physical Properties of the Ternary System Acetone-n-Butyl Alcohol-Water”. In: *The Journal of Physical Chemistry* 36.3 (Mar. 1932), pp. 842–854. DOI: [10.1021/j150333a006](https://doi.org/10.1021/j150333a006).
- [145] *Physical properties of glycerine and its solutions*. Glycerine Producers’ Association, 1963. URL: http://web.archive.org/web/20200916133840/https://www.cleaninginstitute.org/sites/default/files/research-pdfs/Physical_properties_of_glycerine_and_its_solutions.pdf.
- [146] *Biokraftstoffe Basisdaten Deutschland*. Version from Nov. 8. 2019. Fachagentur Nachwachsende Rohstoffe e. V. URL: http://web.archive.org/web/20191108130106/http://www.bioenergie-weserbergland-plus.de/bioenergie/files/literatur/pdf_174_basisdaten_biokraftstoff.pdf.

Bibliography

Nomenclature

Latin letters

Symbol	Units	Description
a		parameter
a		wetting case in Fig. 4.9
A	m^2 or px^2	area
A		geometrical factor
b		wetting case in Fig. 4.9
\vec{b}		vector
B		friction factor
c	m	cuspl depth
c		wetting case in Fig. 4.9
\vec{c}		ray calibration column vector
d	m	width
e		Euler's number
e		pressure error
\vec{e}		unit vector
f	$(kg\ m)/s^2$	viscous friction force

Continued on next page

Latin letters continued from previous page

Symbol	Units	Description
f		fraction of wetted solid area
f		function
F		roundness factor
F		dimensionless rivulet thickness
g	m/s^2	gravity constant
g		function
G		coefficient
h	m	height
H	m	characteristic height
H		sample set with varying height
k	m	slice length
l	m or px	length
L		coefficient
m	m	distance from edge along the bisection axis
n		index of refraction
\vec{n}		normal vector
o	m	rivulet tip distance sharp/round edge
p	$\text{kg}/(\text{m s}^2)$	pressure
p		laser contact line intersection
\vec{p}		visible laser refraction direction
q		fitting factor

Continued on next page

Latin letters continued from previous page

Symbol	Units	Description
r	m or px	radius
r		ratio of real to apparent surface area
\vec{r}		ray calibration row vector
\mathbf{R}		rotation matrix
s	m	step size
\vec{s}	m	ray starting position vector
\vec{s}		camera view direction
S	m	Roughness parameter
t	s	time
T	s	characteristic time
u	m/s	speed
v	(m)	(distance along) coordinate axis
w	(m)	(distance along) coordinate axis
w	m	distance between two parallel walls
W		constant
W		sample set with varying width
x	(m)	(distance along) coordinate axis
x	m	distance from edge along a wall
y	(m)	(distance along) coordinate axis
y	m	length
z	(m)	(distance along) coordinate axis

Continued on next page

Latin letters continued from previous page

Symbol	Units	Description
\vec{img}		image size vector
\vec{pix}		image position vector
\vec{ray}		ray vector
Concluded		

Greek letters

Symbol	Units	Description
α	deg	angle
δ	m	rivulet thickness
η		dimensionless height
γ	deg	angle
γ	deg	opening angle
κ	1/m	curvature
μ	kg/(m s)	dynamic viscosity
π		Archimedes' constant
ρ	kg/m ³	density
σ	kg/s ²	surface tension
τ	deg	tilting angle
Continued on next page		

Greek letters continued from previous page

Symbol	Units	Description
τ		dimensionless time
θ	deg	contact angle
ξ	deg	slice angle
Ξ		similarity variable
Concluded		

Dimensionless groups

The given dimensionless groups are valid for general cases; hence, appropriate values for the characteristic speed u and the characteristic length l can be inserted for different cases.

Symbol	Name	Definition	&	Meaning
Ca	Capillary number	$Ca = \frac{\mu u}{\sigma}$	$\hat{=}$	$\frac{\text{viscous forces}}{\text{surface tension forces}}$
Re	Reynolds number	$Re = \frac{\rho u l}{\mu}$	$\hat{=}$	$\frac{\text{inertial forces}}{\text{viscous forces}}$
We	Weber number	$We = \frac{\rho u^2 l}{\sigma}$	$\hat{=}$	$\frac{\text{inertial forces}}{\text{surface tension forces}}$
Concluded				

Subscripts

Subscripts	Description
0	origin
1	point 1
1	direction 1
2	point 2
2	direction 2
<i>a</i>	advancing
<i>a</i>	average absolute height
<i>a</i>	first case
<i>b</i>	second case
<i>B</i>	Bullard et al.
<i>c</i>	corner
<i>c</i>	third case
<i>d</i>	dynamic
<i>d</i>	direction
<i>g</i>	gas phase
<i>i</i>	variable for different values
<i>l</i>	liquid phase
<i>m</i>	microscopic
<i>m</i>	mirrored
<i>m</i>	coordinate axis subscript

Continued on next page

Subscripts continued from previous page

Subscripts	Description
q	average quadratic height
r	receding
r	reflection
s	starting position
v	coordinate axis subscript
w	wall
w	coordinate axis subscript
x	coordinate axis subscript
y	coordinate axis subscript
z	highest height difference
z	coordinate axis subscript
cp	corner to pool
dl	dimensionless
lg	liquid-gas interface
ls	liquid-solid interface
sg	solid-gas interface
app	apparent
cam	camera opening
dir	direction
inner	inner
max	maximal

Continued on next page

Subscripts continued from previous page

Subscripts	Description
min	minimal
per	perimeter
ray	ray
real	real
rough	rough surface
sens	sensor
sharp	sharp
tip	rivulet tip
σ	capillary
∞	far field
Concluded	

Abbreviations

Abbreviation	Description
1D	one-dimensional
2D	two-dimensional
3D	three-dimensional
DMLM	direct metal laser melting
Continued on next page	

Abbreviations continued from previous page

Abbreviation	Description
FFF	fused filament fabrication
HDR	high dynamic range
MD	molecular dynamics
NI	National Instruments Corp.
PDMS	polydimethylsiloxane
PE	polyethylene
PI	Physik Instrumente (PI) GmbH & Co. KG
PLA	polylactic acid
PP	polypropylene
SE	Surface Evolver
SLS	selective laser sintering
SNR	signal-to-noise ratio
UV	ultraviolet
VOF	volume-of-fluid
Concluded	

Nomenclature

List of Figures

2.1	Contact line and contact angle θ shown for a drop on a flat surface.	8
2.2	The linearized contact line region of liquid on a wall moving to the right.	13
2.3	A qualitative sketch schematically showing the relationship between dimensionless contact line speed and contact angle.	16
2.4	Pinning at a sharp kink until the advancing contact angle increased by $\Delta\theta_a = \gamma$. For receding contact lines the same pinning happens until the contact angle is decreased by $\Delta\theta_r = \gamma$	17
3.1	A simplified 3D rendering of the experimental rig, basic CAD model courtesy of Frank Plückebaum.	22
3.2	A simplified 3D rendering of the experimental rig observed from a second perspective, basic CAD model courtesy of Frank Plückebaum.	23
3.3	Left: The latest version of the sample clamp in use. Center: The first version of a vertical rotation unit. Right: A gravure printing test module.	26
3.4	Left: The wide surface/small volume pool. Right: The overflowing cylinder pool.	28
3.5	The sample geometry used for the majority of experiments in this thesis. Image adapted from [64].	33
3.6	A stainless steel sample with the geometry shown in Fig. 3.5, a step size of 15 mm and a height of 100 mm.	34
3.7	Stainless steel samples with only one analyzed edge, but different edge opening angles.	35

List of Figures

3.8 Left: The PLA sample used for validation in [63]. Right: The aluminum profile used to cast the sample with visible PLA remains where its meniscus broke off. 36

3.9 Three aluminum samples used for roughness measurements. From left to right: Sandblasted, milled, polished. 38

3.10 A PLA sample printed with fused filament fabrication. The horizontal layers as well as a diagonal wavy pattern due to mechanical restrictions (timing belt) of the 3D printer are visible. 39

3.11 The measurement principle of a Wilhelmy tensiometer shown in cross section. The sample plate stays at the pool level height (dashed yellow line) while the liquid forms a meniscus with a nearly straight contact line (red). The liquid surface tension exerts a force along the contact line (small green arrows) in a direction given by the contact angle. The large green arrow above the sample symbolizes the force needed to balance the contact line forces. 40

3.12 The principle of the target calibration. A target (a) is filmed at two different positions in a known distance and rotation to the sample (c). With the target images the frustum (blue) of the camera (b) can be calculated and used to transform the camera images into perspective free mappings as visible in (d). Image adapted from [107]. 45

3.13 Top: A screenshot of the post-processing tool showing an image of a sample and the marked edges for calibration. Bottom: A 3D model of the sample projected onto the image using the calibration from the top. 48

3.14 The 2D ray system used for manual calibration. The green line in the top left is the camera sensor tilted by τ and the yellow lines illustrate the outer perimeters of the camera frustum and its opening angle α_{cam} . The blue (1) and the darker green (2) lines show the rays to two points with a known height difference Δh . The purple (c) and the red (r) lines show the rays towards the lowest point of the sample corner respectively its reflection on the liquid. The light green line (m) is the mirrored reflection of (r) connecting the corner point and its mirrored image on the liquid. 52

4.1 Left: An edge with an opening angle γ satisfying the Concus-Finn criterion (Eq. (4.1)) and thus forming a rivulet. Right: An edge with an opening angle above 180° forming a cusp. Images adapted from [64]. 60

4.2 Left: The rivulet described as a collection of vertical tubes filling out the space between the adjacent walls. The vertical curvature on the top of tubes is the source of negative capillary pressure. Right: The rivulet described by horizontal slices determining the negative capillary pressure. Images adapted from [64]. 61

4.3 The contact line on the center face of samples as shown in Fig. 3.5. The plots are aligned at the outer edge with the cusp and the dashed lines illustrate the corresponding inner edge position for each sample. Height and face position are divided by the capillary length l_σ . The contact line shape was recorded after reaching an asymptotic static position. Data published in [64]. 64

4.4 The depth of the cusp below the unaffected meniscus height for different step sizes of the samples from Fig. 3.5. The green lines show the cusp depth for an infinite step size calculated with Surface Evolver for contact angles of 0° and 20° . The dotted red line shows the depth of the cusp calculated with Eq. (4.12) using the lower numerical depth as c_{max} . The cusp depths and step sizes are normalized with the capillary length l_σ . Data published in [64]. 66

List of Figures

4.5	The contact line on the center face of samples as shown in Fig. 3.5. The plots are aligned at the inner edge with the rivulet and the dashed lines give the corresponding outer edge position for each sample. Only samples with step sizes above $0.166 l_\sigma$ are shown. Height and face position are divided by the capillary length l_σ . Data published in [64].	68
4.6	A comparison of the rivulet shapes predicted by Eqs. (4.2)-(4.15). For the chosen parameters some of the equations result in equal shapes, which is not the case for all parameter combinations. Data published in [64].	69
4.7	A sketch of three of the orthogonal planes used for the derivation of the unified rivulet shape equation Eq. (4.14). Image adapted from [64].	71
4.8	A sketch of the orthogonal planes used for the derivation of the improved rivulet shape equation, Eq. (4.25). A rivulet (blue) in an edge of opening angle γ is described by its liquid surface in the bisection plane (red) of the edge. The green slice is orthogonal to the liquid surface in the bisection plane with an orthogonal wall distance of y_w . The opening angle of the green slice is ξ and the in-slice distance between the liquid surface in the bisection plane and the edge is k . The inset on the top right shows the definition of α_m at a given position m along the M axis which bisects the edge horizontally. Image adapted from [63].	73
4.9	Three geometrically different wetting cases of which six wetting configurations with inverted air and liquid phases exist. The yellow angle is $\xi/2$, the green angle is θ^* and the purple line is the length y_w . Image adapted from [63].	75
4.10	Calculated rivulet heights for a supersaturated tenside solution. The Concus-Finn criterion is shown as vertical dashed line. The red line shows the height directly in the edge and the green line shows the approximated height at the rounded sample. The shaded areas show the Surface Evolver results for convergence criteria from 1×10^{-7} to 1×10^{-9} . Data published in [63].	82

4.11	The Capillary number of the rivulets for different step sizes (compare to Fig. 3.5) plotted over dimensionless time (Eq. (4.43)). Data published in [64].	84
4.12	The dimensionless rivulet rise speed scaled by the factors given by Eq. (4.45). Left: $d = \text{const.}$ and $d = 0.2l\sigma$. Right: $2d = \text{const.}$ and $d = 0.1l\sigma$. Data published in [64].	85
4.13	The measured rise heights over time in comparison to the 1/3 power law and the theory from Eq. (4.67). Height and time are expressed in the dimensionless values described in Eq. (4.65) and Eq. (4.66). Data published in [90].	87
4.14	The geometry assumed for horizontal rivulet cross sections for the calculation of the rivulet rise in real-world edges. .	88
4.15	The rise height over time from Eq. (4.67). Plotted for different edge radii with otherwise constant parameters. Data published in [90].	94
4.16	Eq. (4.67) fitted on the data of Deng et al. [85]. Top: The H sample series. Bottom: The W sample series. The 1/3 power law is shown in comparison. The black crosses mark the points at which the rivulets reach their final height h_{max} (Eq. (4.50)). Data published in [90].	98
4.17	The values of r_w and B from Table 4.2 plotted over the edge opening angle. B values for acetone ($\theta = 24.3\text{-}25.9^\circ$) are marked by upright triangles and B values for ethanol ($\theta = 19.8\text{-}21.8^\circ$) are marked by downward triangles. [85] Data published in [90].	100
4.18	The measured steady-state rise heights for forced rivulet wetting in comparison to the 1D model from Eq. (4.25) and results from the Surface Evolver for convergence criteria from 1×10^{-7} to 1×10^{-9} . The dashed vertical line is the Concus-Finn criterion. Data published in [63].	102
4.19	A cross section of a rivulet and the flow profile inside when rising up an edge (left) or staying constant at a moving edge (right). Image adapted from [63].	103

List of Figures

4.20	A comparison of a constant height rivulet on an edge moving down with 5 mm/s (left) and a spontaneously rising rivulet at approximately the same height (right, with a cusp at the right image border). The camera perspective is not exactly equal in both images.	105
4.21	A stainless steel sample with an edge opening angle of 135° dipped into a pool of 20 cSt silicone oil. Safety precautions against silicone oil contamination are visible in the form of PE foil at the clamp and below the pool, with additional paper towels.	106
A.1	An example of small (left) and large (right) detected objects with either circular (red) or irregular shape (green). Table A.1 gives the parameters of this objects described by Eqs. (A.3)-(A.5).	126
A.2	Left: A sketch of a laser light sheet orthogonally illuminating a sample, resulting in a vertical red line (dotted frame below the liquid surface). Due to liquid refraction a kink and a bending of the red laser line is visible in the camera. Right: The same situation shown in a ray tracing 3D render to give better insight into the real phenomenon.	128

List of Tables

4.1	Least square fitted values for r_w and B for the experiments shown in Fig. 4.13. Data published in [90].	93
4.2	The geometrical sizes of the different samples used in [85] and the fitted values for Eq. (4.67) for this samples. H5 and W2 label the same physical sample. Data published in [90].	96
5.1	A qualitative comparison of the different fabrication methods tested for the production of specified rough samples.	110
A.1	Parameters from Eqs. (A.3)-(A.5) for the objects given in Fig. A.1.	127
A.2	The most important physical properties of the (pure) liquids used or tested in this thesis (at 25 °C). [141–146] * For acetone no measurement temperature is given by [144]. ** The density of sunflower oil is given at 15 °C by [146], the other values are based on own measurements.	132
A.3	Roughness parameters resulting from different subtractive fabrication methods used for aluminum samples. S_z is highest measured height difference on the observed surface area. S_a is the average absolute height and S_q the average quadratic height of the roughness. The additional surface is equal to $(A_{real} - A_{app})/A_{app}$ or $r - 1$. Data from the Bachelor thesis of Weidler [94].	133